University of North Dakota
UND Scholarly Commons

Theses and Dissertations | Theses, Dissertations, and Senior Projects

2008

Geochemical Analysis of Ironstone Preserved Molluscan Fossils of the Hell Creek Formation (Cretaceous) and Ludlow Member of the Fort Union Formation (Paleogene) of Southwestern North Dakota

Tanya P. Justham
University of North Dakota

Follow this and additional works at: https://commons.und.edu/theses

 Part of the Geology Commons

Recommended Citation

Justham, Tanya P., "Geochemical Analysis of Ironstone Preserved Molluscan Fossils of the Hell Creek Formation (Cretaceous) and Ludlow Member of the Fort Union Formation (Paleogene) of Southwestern North Dakota" (2008). *Theses and Dissertations*. 154.
https://commons.und.edu/theses/154

This Thesis is brought to you for free and open access by the Theses, Dissertations, and Senior Projects at UND Scholarly Commons. It has been accepted for inclusion in Theses and Dissertations by an authorized administrator of UND Scholarly Commons. For more information, please contact zeineb.yousif@library.und.edu.

GEOCHEMICAL ANALYSIS OF IRONSTONE PRESERVED MOLLUSCAN FOSSILS OF THE HELL CREEK FORMATION (CRETACEOUS) AND LUDLOW MEMBER OF THE FORT UNION FORMATION (PALEOGENE) OF SOUTHWESTERN NORTH DAKOTA

by

Tanya P. Justham

Bachelor of Science, St. Lawrence University, 2001

A Thesis

Submitted to the Graduate Faculty

of the

University of North Dakota

in partial fulfillment of the requirements

for the degree of

Master of Science

Grand Forks, North Dakota

May

2008

This thesis, submitted by Tanya P. Justham in partial fulfillment of the requirements for the Degree of Master of Science from the University of North Dakota, has been read by the Faculty Advisory Committee under whom the work has been done and is hereby approved.

_____
Chairperson

_____

_____

This thesis meets the standards for appearance, conforms to the style and format requirements of the Graduate School of the University of North Dakota, and is hereby approved.

_____
Dean of the Graduate School

_____
Date

PERMISSION

Title Geochemical Analysis of Ironstone Preserved Molluscan Fossils of the Hell Creek Formation (Cretaceous) and Ludlow Member of the Fort Union Formation (Paleogene) of Southwestern North Dakota

Department Geology

Degree Master of Science

In presenting this thesis in partial fulfillment of the requirements for a graduate degree from the University of North Dakota, I agree that the library of this University shall make it freely available for inspection. I further agree that permission for extensive copying for scholarly purposes may be granted by the professor who supervised my thesis work or, in his absence, by the chairperson of the department or the dean of the Graduate School. It is understood that any copying or publication or other use of this thesis or part thereof for financial gain shall not be allowed without my written permission. It is also understood that due recognition shall be given to me and to the University of North Dakota in any scholarly use which may be made of any material in my thesis.

Signature _____

Date _____

TABLE OF CONTENTS

LIST OF FIGURES

LIST OF TABLES

ACKNOWLEDGMENTS

The author would like to thank the members of her graduate committee: Dr. Joseph Hartman, chairman, Dr. Richard LeFever, and Dr. Scott Korom for their advice and assistance with this project. For their assistance with collecting specimens, she would like to extend her appreciation to Dr. Arthur Bogan, Marron Bingle, Matthew Burton-Kelly, Kristyn Voegele, Benjamin Huffman, and the Fall 2007 Paleo (Geol 415) class: Nathan Munson, Derek Tuoriniemi, Lucas Buckingham, Anna Crowell, and Chad Turner. Dr. Kanishka Marasinghe, UND physics department, provided use of the physics x-ray diffractometer, and many hours of his expertise to help identify troublesome minerals and correct descriptions of XRD methods. Dr. Ronald Matheney provided much appreciated guidance and assistance with the geochemical analyses. Dr. Annette Summers Engal, Louisiana State University, consulted on the influence of bacteria on the reduction of Fe^{3+} and the formation of siderite. Isotope analyses were performed, on short notice, by Dr. David Dettman at the University of Arizona. The project was supported, in part, by funding provided by Dr. Hartman in the form of a graduate research assistantship and financial support for use of the SEM. Dr. Bogan and Dr. Hartman provided financial assistance for field work in the summer of 2007. The department's purchase of, and Dr. Hartman's part in procuring, Geochemist's Workbench® were immensely beneficial to this project, and deserves much gratitude. Finally, the writer would also like to thank her

husband and true friend, Colin Ferguson, for help with sample preparation, photography, and for supporting her throughout the entire process.

ABSTRACT

The uppermost Cretaceous Hell Creek Formation and Paleocene Ludlow Member of the Fort Union Formation in easternmost Montana and western North Dakota produce ironstone preserved freshwater molluscan fossils. Ironstone preserved mollusks are associated with ironstone nodules, which have been described as composed of iron carbonate, iron oxide, or manganese oxide by various researchers. To date, the exact composition of the ironstone preservation has not been satisfactorily determined to allow agreement between researchers. Freshwater mollusk fossils, preserved as ironstone external casts, molds, and steinkerns, tend to be highly weathered. The poor preservation of the fossils has resulted in little professional interest, with a limited understanding of the geochemical conditions that produced this preservational phenomenon. The intent of this project was to determine the composition of the ironstone, and attempt to constrain the geochemical conditions necessary to produce the ironstone preservation.

Ironstone preserved fossils and nodules were collected from five localities in Bowman and Slope Counties in southwestern North Dakota. In order to determine the mineralogical composition, samples of mollusks and nodules were analyzed using x-ray diffraction (XRD). Four fossil and four nodule samples were sent to the University of Arizona for ^{18}O and ^{13}C isotope analyses. The elemental composition of three mollusks and two nodules were analyzed using a scanning electron microscope (SEM) equipped with an energy dispersive spectroscope (EDS). Composition information collected from

the XRD analyses were entered into the computer program Geochemist's Workbench®, in which Eh-pH stability diagrams were created to constrain the geochemical conditions necessary to produce ironstone preservation.

XRD analyses have identified the current mineralogical composition of the ironstone nodules and fossils as siderite (FeCO3), quartz (SiO2), and goethite (FeOOH). The original nodule-forming iron mineral was identified as siderite. Analysis of thermodynamic relationships and stability diagrams indicates that siderite formation occurs within a fairly restricted range of ion activities and Eh-pH conditions. Because sulfate will preferentially combine with ferrous iron to form pyrite, the system must have little to no sulfate activity. Similarly, the fugacity of carbon dioxide must be relatively high in order to encourage the precipitation of siderite. The activity of iron must be above 10^{-6} mol/kg for siderite precipitation; however, increased iron activity beyond 10^{-6} mol/kg does not appear to increase the overall stability of siderite. From Eh-pH diagrams, it can be determined that siderite is only stable in a neutral to basic and a moderately to severely reducing environment.

Ferrous iron ions may have directly replaced the calcium ions in aragonitic shells without the dissolution of aragonite and precipitation of siderite. A replacement scenario allows for the preservation of shell ornamentation observed on many of the ironstone preserved mollusks. SEM and isotope analyses indicate that the siderite was formed in a completely continental environment. The restrictions for siderite precipitation and stability provide a guide for the geochemical pore water conditions that may have existed during early diagenesis of the Hell Creek Formation and Ludlow Member.

CHAPTER I

INTRODUCTION

Purpose

The southwestern corner of North Dakota, in Slope and Bowman Counties, contains outcrops of Upper Cretaceous and lower Paleogene sediments of the eastern Williston Basin. Specimens of freshwater mussels and gastropods, and occasional vertebrate and plant fossils, are commonly preserved as ironstones on either side of the Cretaceous-Paleogene boundary in the Hell Creek Formation and Ludlow Member of the Fort Union Formation. Previous researchers have suggested (Frye, 1967; Groenwold, 1971; Moore, 1976; Murphy et al., 2002), with little verification, that the ironstones may be composed of an iron carbonate, iron oxide, or manganese oxide mineral, or a mix thereof. The invertebrate fossils are preserved with no original shell material as external casts and molds and occasionally as steinkerns.

Ironstone fossils east of the Miles City Arch in the Williston Basin are generally very weathered, destroying distinguishing features such as ornamentation and growth lines. Due to the poor preservation, ironstone fossils have largely been ignored in favor of the age-equivalent, relatively pristine freshwater mussels to the west of the Miles City Arch. Because of this lack of interest, the groundwater environment and diagenetic processes that resulted in an ironstone preservation are not well understood. There has been some detailed sedimentological work in the Hell Creek Formation, but not viewed

from a shell preservational perspective. Except for Moore (1976), there have been only isolated studies on the Ludlow Member with little discussion of ironstone features. Very little work, even from a sedimentological viewpoint, has occurred in the Ludlow.

Ironstone-type deposits, however, are common throughout the Western Interior of North America, and other areas in the world. Developing a research model of the preservation of North Dakota fossils may provide a general understanding of this mode of preservation. Project tasks included the determination of the mineral composition of the ironstone fossils, and the construction of a hypothesis that constrains what geochemical and organic conditions could have resulted in the ironstone phenomenon at the localities under study.

Location

Ironstone preserved fossils and nodules are found in the Hell Creek Formation and the Ludlow Member throughout the eastern portion of the Williston Basin in western North Dakota and eastern Montana. In North Dakota, these rocks crop out along the Missouri River drainage south of Bismarck, and in the drainage of the Little Missouri River southwest of Bismarck. The badlands topography and limited vegetation in the southwestern corner of the state, as well as the easily viewed contacts between the Cretaceous and Paleogene sediments, make the Little Missouri River Valley ideal for the study of ironstone nodule zones containing freshwater molluscan fossils. Fossil and nodule localities analyzed in the study include Bowman and Slope Counties (Figure 1). The study area covers from T129N to T134N, and R105W to R106W. Exact latitude and longitude locations for field localities are included in the Field Methods section.

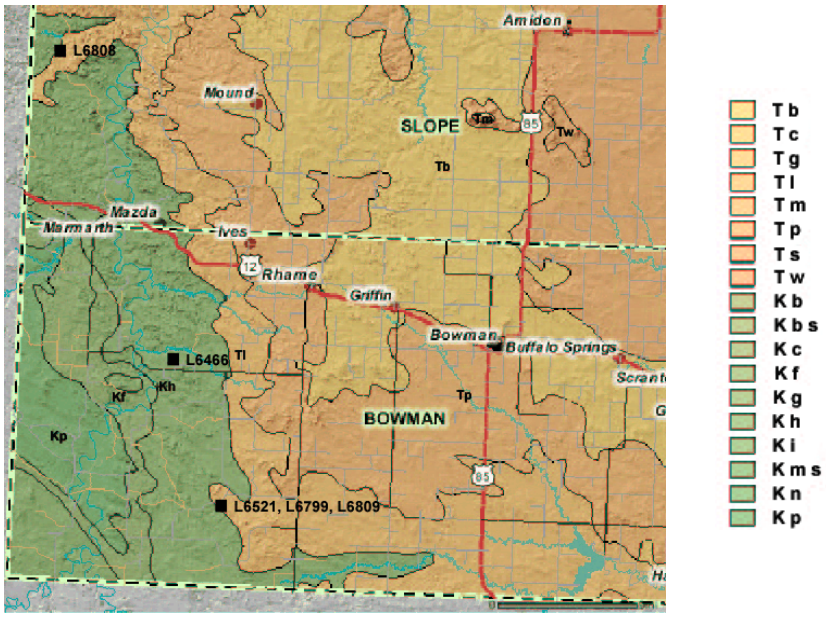

Figure 1. Study area location and bedrock geology map (Kh = Hell Creek, Tl = Ludlow). Map created using the North Dakota Hub Explorer (http://web.apps.state.nd.us/hubexplorer/generalinfo/viewer.html).

Stratigraphic Nomenclature

The Maastrichtian-age Hell Creek Formation in the study area occurs in the outcrop area of the Williston Basin. The Hell Creek overlies the Fox Hills Formation (Figure 2), which can be discerned from the former by the cleaner sandstone (Murphy et al., 2002). The Hell Creek is overlain by the Paleocene Ludlow, which has been referred to as both a formation within the Fort Union Group (Fastovsky, 1987), or as a member of the Fort Union Formation (Murphy et al., 2002). The older usage, Ludlow Member, is that of the U.S. Geological Survey (USGS), while the North Dakota Geological Survey has moved the Fort Union up to group status and recognizes the Ludlow Formation (Moore, 1967). For this study, the older USGS usage will be observed.

The Ludlow Member is the basal unit of the Fort Union Formation. The upper contact of the Ludlow Member in southwestern North Dakota is with the Tongue River

Member, interfingering to the east with the Cannonball Member (Hartman, 2002). Murphy et al. (2002) summarized the criteria that can be used to visually identify the Hell Creek-Ludlow contact, which approximates the Cretaceous/Paleogene (K-Pg) boundary in southwestern North Dakota. The criteria include observing the base of the lowest persistent lignite, the top of the highest claystone with a “popcorn” weathering, and the change from grayish to light brownish or yellow tones.

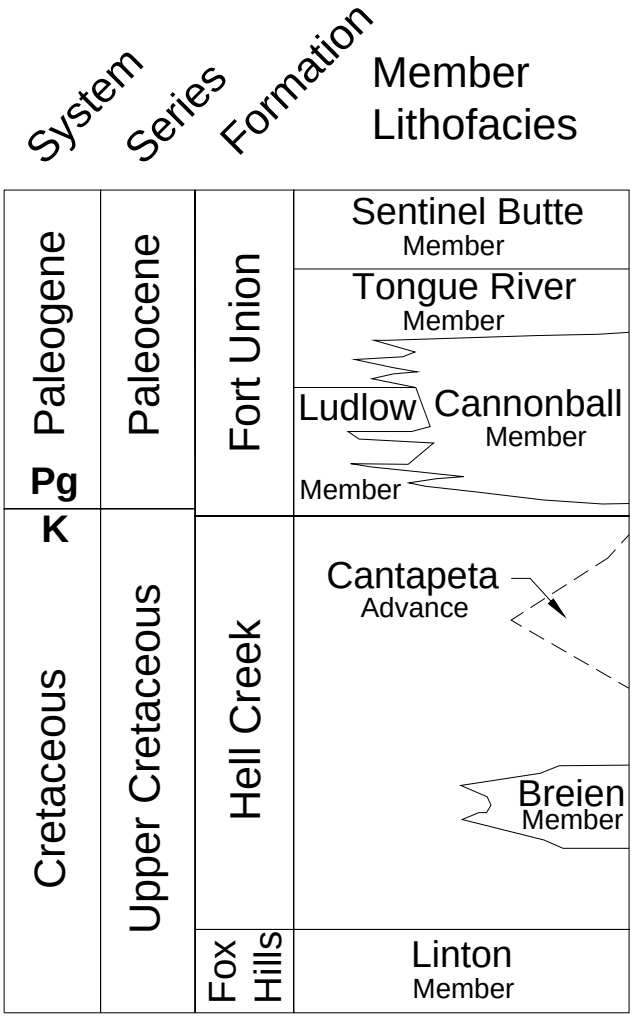

Figure 2. North Dakota stratigraphic column showing generalized stratigraphic nomenclature and relationships in the North Dakota portion of the Williston Basin (after Hartman, 2002).

Sedimentology and Paleogeography

The uppermost Hell Creek and lowermost Ludlow strata in southwestern North Dakota are completely continental in origin. Hell Creek Formation strata consist of somber-colored, poorly cemented, fine-grained sandstone and siltstone, as well as carbonaceous rich shale, mudstone, and claystone (Murphy et al., 2002). Ludlow Member strata are similar to that of the Hell Creek Formation, but slightly less somber in color and containing widespread lignite beds (Moore, 1976). The paleogeography for both the Hell Creek and Ludlow was a broad meandering fluvial environment with poorly drained floodplains caused by a relatively high water table (Fastovsky, 1987). Sediment for the alluvial plain was supplied by the volcanic-rich clastic sediments from an uncertain western source. Meandering streams traveling across the plain emptied into the Late Cretaceous Western Interior Seaway, trending north-south across what is now North America. The formational contact between the Hell Creek and Fort Union approximates an increase in water table elevation from the transgression of the interior seaway, causing a change to large ponds and peat swamps, from which the extensive but discontinuous coals of the Ludlow Member formed (Fastovsky, 1987; Johnson, 2002).

Cretaceous/Paleogene Boundary in the Study Area

As noted, the contact between the Hell Creek and the Fort Union Formations in North Dakota approximates the boundary between Cretaceous and Paleogene (K-Pg) rocks. The K-Pg boundary is well known for the mass extinction event that eradicated the dinosaurs. Research on the patterns of extinction across this boundary, as well as the intriguing hypothesis of a contemporary bolide impact contributing to the extinction

event, has continued to interest and plague researchers. According to Nichols and Johnson (2002), palynology has been used to effectively bracket the boundary in southwestern North Dakota, and is the most reliable method of identifying the boundary.

Previous Work

North Dakota Hell Creek and Ludlow Ironstone Fossils and Nodules

Few workers concerned with the rock units in southwestern North Dakota have spent much time on the nodules or freshwater mollusk fossils in the Hell Creek Formation. Paleontological research in the area has tended to focus on the more dramatic dinosaur and microvertebrate sites. Frye (1967) described many of the concretions and nodules in the Hell Creek Formation in North Dakota, providing discussions of structure, composition, and texture based on thin section analyses. He also provided a brief comparison to similar nodules within the Ludlow Member. Frye (1967) noted that plant, vertebrate bone, and invertebrate fossils were often imbedded in siderite ($FeCO_3$) nodules, whereas they were rarely preserved in other lithologies.

Groenewold (1971) provided a more detailed discussion of concretions and nodules in the Hell Creek Formation. Concretions were defined as mineralogically similar to the surrounding sediments, but more resistive. Nodules were more resistive and mineralogically different from enclosing sedimentary material (Groenewold, 1971). The several forms of limonitic nodules described by Frye (1967) were included by Groenewold within the descriptive groups of siderite masses or siderite lenses, which encompassed all of the “ironstone” nodules. Despite a methods section discussing his use of XRD, Groenewold never actually stated that he ran samples of the “siderite” nodules.

He did describe the results of thin section analyses that indicate nodules are composed of siderite, but not whether the siderite itself is original or a replacement of an earlier concreting mineral. Groenewold (1971) did not refer to any fossils associated with the ironstone nodules.

Moore (1976) described the various types of concretions and nodules of the Ludlow Member and classified them as either carbonate concretions or ironstone nodules. Although earlier workers suggested that the nodules had been formed during Ludlow time, Moore argued that some of the rounded ironstone nodules are actually early clay clasts replaced by iron oxide after channel filling. He did not describe the method of interpretation used to reach this conclusion. Moore (1976) did not mention an association between the nodules and invertebrate fossils, and did not describe ironstone preservation in his discussion of fossils.

Murphy et al. (2002) mentioned the abundant nodules of iron and manganese oxide that occur throughout Hell Creek strata. The composition of the nodules appears to have been decided based on the color exhibited by the exterior of the nodules, rather than by a definitive test. Murphy et al. (2002) mentioned in passing that plant molds, steinkerns of freshwater mussels, and occasional dinosaur bones are often preserved in lenticular, iron oxide beds.

Siderite Nodules and Fossils

Research on the formation of siderite in ancient sediments has largely been neglected. There is, however, some literature that describes the geochemical environment of recently formed siderite formations (Postma, 1977; 1981; 1982; Burton et al., 2006),

and a few articles that consider the preservation of modern iron carbonate fossil concretions (Allison and Pye, 1994; Pye et al., 1990). Postma (1977; 1981) described the formation of siderite in a Denmark bog and within brackish and freshwater swamp sediments (Postma, 1982) by analyzing the composition of the siderite and measuring the Eh and pH of the pore water at sample locations. The siderite analyzed from a bog in Jutland, Denmark, was found to have considerable manganese and calcium contents (Postma, 1977; 1981). Sulfur was present only in minor amounts within the bog (less than 1 % of total content), preventing the formation of iron sulfides. Pore water in the bog was supersaturated with respect to siderite, indicating a very slow precipitation rate. Similar supersaturation and slow precipitation was observed in coastal lowland acidic sulfate soils (CLASS) of Australia, although the iron carbonate in the CLASS environment appears to have been affected by the slightly higher sulfate concentrations within the system. Postma (1981) argued that pH is the major controlling factor of siderite stability within the Denmark bog. The mixing within the bog of acidic, iron rich groundwater from the outwash plain with the basic, carbonate rich water from a till area creates the optimum environment for the precipitation of iron-rich mixed carbonates.

Both siderite and pyrite were found in Skjernå delta swamp sediments in Denmark; however, the siderite was associated with a freshwater environment, while the pyrite was associated with a brackish environment (Postma, 1982). The Skjernå delta swamp freshwater sediments have a relatively low concentration of dissolved sulfur indicating little to no sulfate reduction within the system to provide sulfur for pyrite formation. Two processes for siderite formation were suggested: by the direct

replacement of $CaCO_3$, or by the reduction of ferric oxyhydroxides by organic matter providing both ferrous iron and carbon dioxide for the formation of siderite (Postma, 1982).

Both of the studies of modern siderite formation within Denmark agree with the thermodynamic equilibrium calculations developed by Garrels and Christ (1965). The presence of siderite is associated with moderate to strong reducing conditions. Garrels and Christ argue (1965) that, in order to have a significant stability field for siderite, the activity of dissolved carbonate must be very high, and reduced sulfur must be very low. The activity of calcium, or the relationship between the system and calcium carbonate in contact with the system, is not taken into consideration in their discussion.

Mozley (1989) developed the relationship between depositional environment and the percent composition of early diagenetic siderite in modern sediments. Marine waters produce siderite with a higher Mg^{2+}/Ca^{2+} ratio than meteoric waters. Siderite precipitated from meteoric waters contains more Fe^{2+} and Mn^{2+}, and less Mg^{2+}, than siderite precipitated from marine waters, and often approaches end-member composition (Mozley, 1989). The Ca^{2+} content appears to vary in both meteoric and marine waters. Mozley and Wersin (1992) developed the relationship between depositional environment and the isotopic composition of early diagenetic siderite. Marine siderites tend to have $\delta^{13}C$ values less than -8 ‰ and variable $\delta^{18}O$ values. Siderites with $\delta^{18}O$ values less than -13 ‰ and positive $\delta^{13}C$ values are usually continental in origin, although the $\delta^{18}O$ values in continental siderites can also be variable (Mozley and Wersin, 1992). Baker et al. (1995) used the relationship developed by Mozley (1989) between the geochemistry of

early diagenetic siderite and depositional environment, along with Mozley and Wersin's (1992) relationship between isotopes and the depositional environment of siderite, to determine the depositional environment of the Triassic Rewan Group in eastern Australia. Baker et al. (1995) determined that the early diagenetic concretionary and nonconcretionary siderite from the Rewan Group represented a completely continental depositional environment, as well as a meteoric porewater composition during early diagenesis.

Modern examples of siderite preservation of fossiliferous concretions from the North Norfolk coast of England indicate that the concretions can form within tens of years, and visible mineralization can occur within months (Allison and Pye, 1994; Pye et al., 1990). Aragonitic molluscan shells were found to be more highly sideritized than those of calcite (Allison and Pye, 1994). The siderite was observed to be directly replacing the shell aragonite, allowing for the preservation of shell morphology. Stable isotope analysis of carbon and oxygen isotopes suggested that the shell aragonite was the source of carbonate for siderite formation (Allison and Pye, 1994).

CHAPTER II

METHODS

Field Methods

Field work was performed during August and September of 2007 at various localities in the Hell Creek Formation and Ludlow Member of the Fort Union Formation in Slope and Bowman Counties. Localities, both those previously known and new sites, were chosen for collection based on the presence and association of ironstone nodules and ironstone-preserved fossils of freshwater mollusks. An association was defined as ironstone nodules and fossils existing together on a bedding or weathering plane, or, preferably, fossils imbedded in, or otherwise attached to, a nodule or nodules. The necessity of sampling associated nodules was realized after three ironstone fossils were chosen from the Paleontological Collections at the University of North Dakota and analyzed by x-ray diffraction (XRD) as a preliminary test of composition. The fossils were found to be too highly weathered to provide definitive results. A hypothesis was developed that nodules associated with the fossils may not have been as heavily weathered, and may provide information on original composition.

Freshwater molluscan fossils were collected for analysis based solely on presence and abundance, rather than taxa type or quality of preservation. Associated plant fossils were collected, if observed at a locality, but were not included in analyses. Vertebrate fossils were noted, but not collected. The ironstone nodules were selected based on the

criteria of a visible association with invertebrate fossils, a visible reaction to hydrochloric acid, and the size of the nodule, preferably greater than 10 cm in diameter.

Locality L6799

Locality L6799 is a new Hell Creek locality identified at Mud Buttes, Bowman County (Figure 3). Ironstone preserved gastropods and ironstone nodules were collected from the lower meter of a butte and surrounding surface located at latitude 46° 1’ 18.3” N, longitude 103° 45’ 57.5” W. The originating bed was not identified at this locality, and fossils were not attached to the nodules. Popcorn weathered clay covered the bottom part of the butte and the flat area around it, indicating that the sediment in the area consisted of mostly claystone. Gastropods were generally preserved as steinkerns of single whorls or deformed steinkerns of the entire organism. Nodules were dark yellowish brown (10 YR 6/6) to moderate brown (5 YR 4/4) in color with layers of the exterior breaking off in geometric patterns.

Locality L6521

An old site known for producing species of the genus *Sphaerium* (Scopoli, 1777, fingernail clams), Locality L6521, was recollected during the current field work (Figure 4). Located at latitude 46° 1’ 24.3” N, longitude 103° 45’ 54.2” W at Mud Buttes in Bowman County, Locality L6521 occurs within the Hell Creek Formation, approximately 1 m below the K-Pg boundary. The fossils associated with the ironstone nodules at this locality include freshwater mollusks consisting of gastropod whorls and *Sphaerium* species, fish scales, and vertebrate teeth and bones. The strata enclosing the ironstone layer are siltstone and mudstone beds. Sphaerid specimens collected from the locality

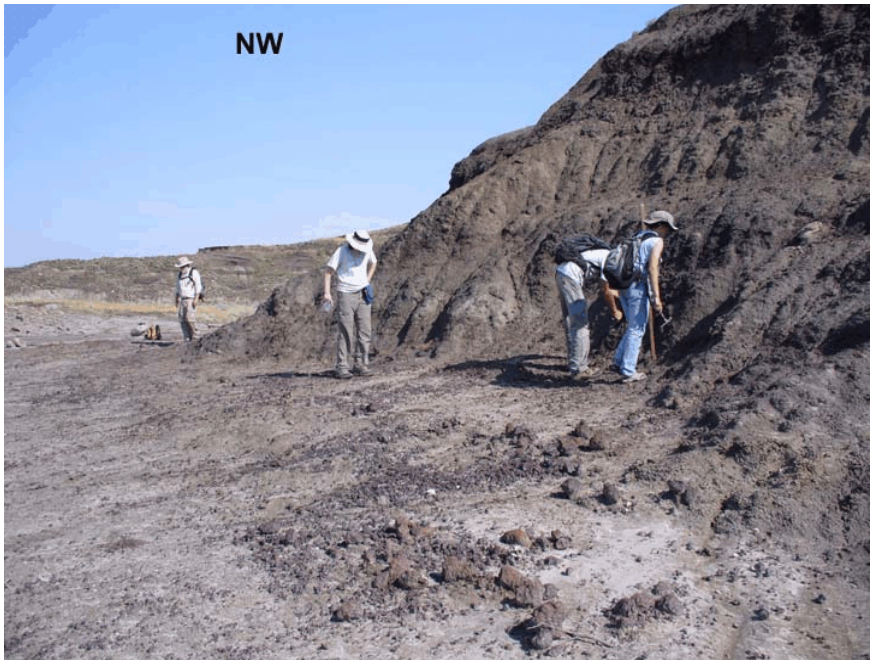

Figure 3. Northwest view of Locality L6799 at Mud Buttes, Bowman County (T.P. Justham, 2007, photo).

Figure 4. View east of Locality L6521, with relationship to K-Pg boundary (J.H. Hartman, 2007, photo).

retained visible growth lines and hinge features (Figure 5). Many gastropod specimens are preserved well enough to show growth lines, and belong to *Campeloma* and *Lioplacodes*. Nodules contained a significant amount of plant matter, but no recognizable invertebrate fossils. The nodules were irregular in shape and very dusky red purple (5 RP 2/2) and brownish black (5 YR 2/1) in color.

Figure 5. Specimen S4712, *Sphaerium* sp. (Locality L6521). Notice the clean edges and visible growth lines. Bar scale is in millimeters (T.P. Justham, 2008, photo).

Locality L6466

Known as the Larkin Locality, Locality L6466 (Figure 6) is located on private ranch property in Bowman County at latitude 46º 9’ 27.0” N, longitude 103º 50’ 8.0” W, stratigraphically located 10.0 m below the top of the Hell Creek Formation. Since the Hell Creek-Fort Union formational contact in Bowman County approximates the Cretaceous/Paleogene boundary, L6466 is located 10.0 m below the K-Pg boundary. The site is at the top of a small, isolated butte, approximately 1.5 m high, in the base of a ravine. An ironstone lenticular bed, 10 to 20 cm thick, caps the butte, and appears to extend into the neighboring hills, although fossils associated with the ironstone nodules have not been observed in the correlated beds. Sediment beneath the ironstone bed consists of poorly cemented, yellowish gray, medium- to fine-grained sandstone. Freshwater unionoid fossils, including *Proparreysia* species (Figure 7), were collected

from where they weathered out on top of the butte, or as detritus around the base of the butte. Unionoid external casts, molds, and steinkerns were collected both as individual entities and attached to nodules (Figure 8), and often retained growth lines and shell ornamentation. Nodules were moderate brown (5 YR 4/4) to moderate yellowish brown (10 YR 5/4) in color and unfractured. Nodules collected from the same ironstone horizon outside the limits of the locality were a dusky blue (5 PB 3/2) color, with a moderate brown (5 YR 4/4) ironstone rind that peeled off in concentric fractures.

Figure 6. View east, outline encompasses Larkin Locality L6466 in Bowman County (J.H. Hartman, 2007, photo).

Figure 7. Specimen S4704, *Proparreysia percorrugata (*Larkin Locality L6466). V-shaped ornamentation distinctive to *Proparreysia* is visible on the umbo, as well as a row of nodes near the aperture. Bar scale is in millimeters (T.P. Justham, 2008, photo).

Figure 8. Ironstone nodule and associated unionoid fossil specimen S4727 (Larkin Locality L6466). Bar scale is 2 centimeters (C.E. Ferguson, 2007, photo).

Locality L6808

Locality L6808 (Figure 9) was found in Ludlow Member strata at Das Goods in Slope County (latitude 46º 26’ 9.8” N, longitude 104º 0’ 9.3” W). The locality produced nodules, vertebrate and plant fossils, and a minimal number of invertebrate fossils, and is equivalent to an Ohio State University microvertebrate fossil site (OSU07-02). Invertebrate fossil specimens consisted of external casts of partial gastropod whirls with

observable growth lines, and gastropod steinkerns. All of the specimens were collected from a ledge where erosional wash had collected, making determination of the producing layer difficult. Fossils were not attached to nodules at Locality L6808. The clayey silt and fine sandstone sediments of the area belong to the Paleocene Ludlow member, and are located approximately 10.6 m above the contact with the Hell Creek Formation. Nodules collected at L6808 were grayish black (N2) and brownish black (5 YR 2/1) in color, rectangular in shape, and occasionally had geometric designs on the surface.

Figure 9. North view of Locality L6808, Das Goods area, Slope County (B.W. Huffman, 2007, photo).

Locality L6809

Locality L6809 (Figure 10) was discovered at Mud Buttes, Bowman County, during fieldwork at latitude 46° 1’ 19.6” N, longitude 103° 45’ 54” W. Ironstone chunks eroding from the 15–cm thick producing layer contained freshwater gastropod and

unionoid fossils, as well as imprints of plant stems. Nodules were mottled light brown (5 YR 5/6), dark yellowish orange (10 YR 6/6), and very dusky purple (5 P 2/2). The light brown and yellowish orange areas were crumbly, and often appeared to contain a significant sand component, while the very dusky purple areas were more coherent. Gastropod and mussel specimens were preserved as external casts, molds, and steinkerns. Growth lines were observed on both external casts and molds. Gastropod specimens generally appeared to belong to *Campeloma*. The relatively few unionoids were not identified. The fine-grained channel sandstone beds bounding the producing layer were located in the Ludlow Member of the Fort Union Formation an undetermined height above the basal contact.

Figure 10. South view of Locality L6809 at Mud Buttes, Bowman County. Producing bed is outlined on the cliff (T.P. Justham, 2007, photo).

Lab Methods

X-ray Diffraction

Three ironstone preserved fossils were originally chosen at random for compositional analysis from Frye's (1967) dissertation specimens collection in the UND Paleontological Collections. Nodules were chosen for proxy analysis for fossils from the same locality based on the size of the nodule and the abundance of fossils associated with the nodule. Preference was given to localities with fossils attached to nodules. More analyses were conducted on nodules from localities preserved in this manner. The samples were labeled T1 through T36 for the test run. Nodules were given a sample number to show how many samples were taken from that particular locality. Ironstone preserved mollusks and non-ironstone, well-preserved, age-equivalent mollusks from Montana were given an institutional specimen number. The Montana fossils, T24–T32 were analyzed for comparison to the ironstone compositions, and to provide information on original shell composition.

Each nodule or fossil chosen for analysis was photographed from various angles, with special attention given to fossils imbedded within the surface of the nodule. Nodules were then cut in half using a Felker Tile Master SC saw to observe the size and composition of the core. Samples T5 and T7–T20 were internal samples taken near the core of the concretion in an attempt to determine the original composition prior to weathering. Using hydrochloric acid to determine the areas near the core with the greatest carbonate content, a small chisel and hammer were used to knock small slivers of ironstone from around the core. The sample slivers were first crushed on an anvil, then

ground using a mortar and pestle and acetone for lubrication into a fine powder of grains < 75 μm in size (less than a #200 sieve size).

Samples T21–T23 were external samples taken from the edge of the nodules to determine the extent of weathering. Specimens T1–T4, T6, and T33–T36 were taken from ironstone preserved fossils, both unionoids and gastropods. Specimens T24–T32 were taken from well-preserved Montana freshwater mussels curated in the UND Paleontological Collections to verify the presence of original aragonite ($CaCO_3$). Fossil specimens were prepared for analysis in a manner similar to the nodules; however, whether an internal sample, whole fossil, or composite of fossils was used depended on the size of the fossils. Choices for ironstone fossil samples were limited by the desire to avoid destroying well preserved samples, which were often also less weathered and would have provided better XRD results.

Copper K_α x-ray diffraction data was measured on a Philips X'Pert Pro® diffractometer with tube settings of 40 kV and 45 mA. A continuous scan speed of 0.21°/s was used, which is equivalent to a step size of 0.008° and a 5-second step time. Approximately two grams of 200 mesh sample powder were prepared for analysis by backfilling stainless steel sample holders having a cylindrical sample chamber of 1 inch diameter and 0.125 inch depth. Samples which did not have enough powder to completely fill the holder were packed on a space filler such as an aluminum disk or a zero-background silicon disk. In order to reduce fluorescence contribution to background, data for all iron containing samples were collected with a proportional counter. Each measurement with the proportional counter lasted 1.5 – 2 hours. Data for the calcite

samples, however, were collected with a multielement X'celerator® solid-state detector, and each measurement took about 6 – 7 minutes. A silicon standard was run with each sample set for calibration of the diffractometer.

XRD results were analyzed using X'pert Highscore and Jade™ Version 3.1 computer programs to search the International Center for Diffraction Data (ICDD) PDF-2 database of representative mineral reflections to try to find close matches. Quartz (SiO_2) and goethite (FeOOH) were the only minerals identified using this method. Other minerals were identified by hand matching sample curves to representative mineral peak reflections printed from the ICDD databases.

Isotopes

Eight ironstone samples, four fossils and four nodules, were sent to Dr. David Dettman at the University of Arizona for $\delta^{18}O$ and $\delta^{13}C$ isotope analyses. Nodule samples for isotope analysis were chosen from four of the five localities based on the strength of the fossil association and the intensity of the siderite peaks in the XRD analysis, indicating unweathered siderite. Fossil samples were chosen for isotope analysis based on the strength of nodule association, the presence of shell ornamentation, and an observable reaction to a 10 % solution of hydrochloric acid. The samples were first powdered and analyzed by the XRD to verify that they were composed of siderite. Two mussels with external shell features were chosen from Locality L6466 as separate samples, two gastropod casts were removed from nodule T15 (L6809) and ground together for a composite sample, and two gastropod whorls were selected from Locality L6799 and

ground together for a composite sample. Values for $\delta^{18}O$ and $\delta^{13}C$ were calculated versus the Vienna Peedee Belemnite (VPDB) standard.

Scanning Electron Microscopy

Two nodule samples and three fossil samples from three of the five localities, excluding Locality L6799 and L6808, were mounted on an aluminum stand and analyzed by a Hitachi S-3400N scanning electron microscope (SEM). The SEM was equipped with an energy dispersive spectroscopy (EDS) system to perform semiquantitative compositional analyses on each sample. Nodule samples consisted of freshly broken chunks, while molluscan samples were analyzed whole. A nodule from L6809 was found to contain a *Campeloma* sp. specimen (S4725), which abutted against the chert core of the nodule (Figure 11). EDS analyses were performed on both the nodule core and the *Campeloma* specimen (S4725) to provide a direct comparison of nodule and fossil elemental composition. An average of five EDS runs were performed on each sample. Weight percentages of iron, magnesium, calcium and manganese for individual EDS runs were rebalanced to constitute 100% of the sample for comparison purposes. The results were then averaged for the entire sample.

Geochemist's Workbench® Essentials

Reaction equations and dominance diagrams for siderite were created using the computer program Geochemist's Workbench (GWB) Release 7.0 with the Essentials package. GWB was developed at the Department of Geology of the University of Illinois at Urbana-Champaign, with the sponsorship of a consortium of companies and government laboratories, and is currently distributed by Rockware, Inc. The default

database for GWB is the Lawrence Livermore National Laboratories (LLNL) database, which supplies activity coefficients calculated according to the extended Debye-Hückel equation (the “B-dot” equation); however, diagrams were also created with the less expansive PHREEQC, WATEQ4F, and MINTEQ databases to compare the agreement in outcome. Calculations for siderite replacement of aragonite performed in GWB Rxn were calculated using only the LLNL database because siderite is not included in the other three databases.

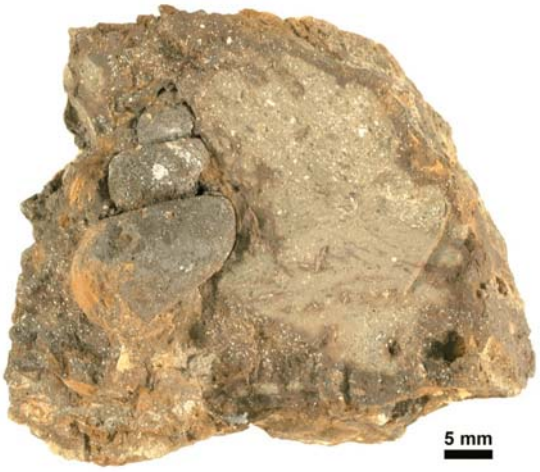

Figure 11. Specimen S4725, *Campeloma* sp. in nodule (Locality L6809). The core of the nodule is shaped around the curves of the gastropod whorls (T.P. Justham, 2008, photo).

CHAPTER III

RESULTS

X-Ray Diffraction

The fossil freshwater mussels sampled from the UND Paleontological Collections, T1 through T4, were found to be very highly weathered and poorly crystalline. Because of the weathering, the XRD intensity counts were very low and the fossils did not provide useful XRD analyses. Quartz and goethite were the only potentially identifiable minerals in these specimens (Table 1), prompting the use of associated ironstone nodules as proxies for the ironstone preserved fossils. Samples T33 through T36 were chosen from newly collected ironstone preserved mollusk fossils that were associated with ironstone nodules. Although the fossils were also quite weathered, the samples were more crystalline than the fossils selected from the UND Paleontological Collections. XRD analyses determined that the fossils were composed of siderite, quartz, goethite, and possibly a small amount of calcite ($CaCO_3$). All XRD intensity curves are included in Appendix A.

As previously mentioned, ironstone nodules were sawed in half prior to XRD sampling in order to exam the core features. Core size and form varied between localities, but all cores were a chert composition (microcrystalline SiO_2), expect for one nodule from Locality L6809, which appeared to have a chert-filled gastropod fossil for the core.

Table 1. Results of XRD analyses for North Dakota ironstone fossils.

Date	Test	Locality	Specimen No.	I/E	Type	Results
07/03/07	1	L0183	S4709	E	Mussel (Unionoid)	Q, G
07/06/07	2	L5657	S4710	I	Mussel (Unionoid)	Q, G
07/09/07	3	L0183	S4709	E	Mussel (Unionoid)	Q, G
07/09/07	4	L6191	S4711	I	Mussel (Unionoid)	Q, G
09/21/07	6	L0183	S4709	E	Mussel (Unionoid)	Q, G
02/25/08	33(15)	L6809	S4705-06	W	2 Gastropods	S, Q, G, C?
02/25/08	34	L6466	S4702	I	Mussel (Unionoid)	S, Q, G, C?
02/25/08	35	L6466	S4703	I	Mussel (Unionoid)	S, Q, G, C?
2/25/08	36	L6808	S4707-08	W	2 Gastropods	S, Q, G, C?

I – Interior W – Whole shell Q – Quartz C – Calcite
E – Exterior S – Siderite G – Goethite

Table 2. Results of XRD analyses for North Dakota ironstone nodules

Date	Test	Locality	Sample No.	I/E	Type	Results
10/23/07	8	L6466	1	I	N	S, Q
10/23/07	9	L6466	2	I	N	S, Q
10/23/07	10	L6466	3	I	N	S, Q, G, C
10/23/07	11	L6466	4NL	I	N	S, Q, G, C
10/23/07	12	L6466	5NL	I	N	S, Q, G, C
10/23/07	13	L6521	1	I	N	S, Q, G, C
– – –	14	L6808	1	I	N	Not Analyzed
11/13/07	18	L6808	2	I	N	S, Q, G
10/23/07	7	L6809	1	I	N	S, Q, C?
10/23/07	15	L6809	2	I	N	S, Q, G, C
10/23/07	16	L6809	3	I	N	S, Q, G, C
11/13/07	19	L6809	4	I	N	S, Q, G
11/13/07	20	L6809	5	I	N	S, Q, G
09/21/07	5	L6799	1	I	N	S?, Q, G
10/23/07	17	L6799	2	I	N	S, Q, G, C
11/13/07	21	L6466	1	E	N	Q, G
11/13/07	22	L6521	1	E	N	S, Q, G, C?
11/13/07	23	L6809	3	E	N	Q, G, C?

I – Interior NL – Non-locality S – Siderite G – Goethite
E – Exterior N – Nodule Q – Quartz C – Calcite

Figure 12. Nodule cores. Clockwise from upper left: a) T11 nodule from ironstone bed correlated with Locality L6466 displaying distinct separation between chert core and ironstone rind. b) T13 nodule from Locality L6521 with intermixed siderite and chert. c) T16 nodule from Locality L6809 showing small, separated core chunks surrounded by a thick rind of ironstone. d) T19 nodule from Locality L6809 exhibiting moderate separation between core and rind. The arrow points to a possible gastropod preserved within the core (T.P. Justham, 2008, photos).

Chert cores were often fractured and infilled with ironstone, or intermixed with the ironstone (Figure 12). At least one fossil was observed within a chert core indicating, along with the intermixing of the core and ironstone, that the chert may have occurred penecontemporaneously to the preservation of the fossils and formation of the ironstone nodules. Speculation on the timing and geochemistry of silica formation, however, is outside the scope of the current research.

Nodule cores were surrounded by two ironstone rinds ranging in thickness from 2 mm to approximately 15 mm. The exterior rind was fairly weathered and consisted of quartz and goethite with occasional small or heavily weathered amounts of siderite. The interior rind was only moderately weathered. All interior rind samples were determined to be composed of siderite, quartz, and goethite, with the possibility of calcite in several samples (Table 2). A significant but unidentifiable peak at 28 $^{o}2\theta$ occurred in several samples, and may indicate a portion of the composition is pyrolusite (MnO_2).

Nine samples (T24 through T32) of well-preserved fossil mollusks (Figure 13) collected from the uppermost Cretaceous Hell Creek Formation in eastern Montana and housed in the Paleontological Collections were analyzed using XRD (Table 3). Five of the samples were found to be original aragonite. *Campeloma* new species A and *Viviparus thompsoni* specimens were composed of original aragonite and an unidentified mineral. Specimens of new Genus A *limneaformis* and *Sphaerium beckmani* were composed of both calcite and aragonite, indicating either partial alteration of the original aragonite to calcite, or a mixed original composition. All of the Montana species sampled are presumed to be represented in the specimens collected from the uppermost

Cretaceous Hell Creek and lowermost Paleocene Ludlow in southwestern North Dakota.

Figure 13. Specimen S2906, *Proparreysia verrucosiformis* (Locality L5233b). Example of a well-preserved mollusk from the Hell Creek Formation of Montana (T.P. Justham, 2008, photo).

Table 3. Results of XRD analyses for well-preserved Montana fossil specimens

Date	Test	Locality	Specimen No.	I/E	Type	Species	Results
01/24/08	24	L5233a	S2905	I	Unionoid	*Proparreysia pyramidatoides* (Whitfield)	A
01/24/08	25	L5233b	S2906	I	Unionoid	*Proparreysia verrucosiformis* (Whitfield)	A
01/24/08	26	L5233b	S2907	I	Unionoid	*Quadrula cylindricoides* (Whitfield)	A
01/24/08	27	L5233b	S2908	I	Unionoid	*Plesielliptio postbiplicatus* (Whitfield)	A
01/24/08	28	L5233b	S2909	I	Unionoid	*Pethobosus aesopiformis* (Whitfield)	A
01/24/08	29	L1151	S2910	W	Gastropod	*Campeloma* n. sp. A	A
01/24/08	30	L5233d	S2911	W	Gastropod	*Viviparus thompsoni* White	A
01/24/08	31	L5233d	S2912	W	Gastropod	New Genus A *limneaformis* (Meek and Hayden)	C, A
01/24/08	32	L6666	S2913 - 18	W	Unionoid	*Sphaerium beckmani* Russell	C, A

I – Interior W – Whole shell C – Calcite
E – Exterior A – Aragonite

$\delta^{13}C$ and $\delta^{18}O$ Isotope Results

Analyses for $\delta^{13}C$ and $\delta^{18}O$ isotopes were relatively consistent between the nodules and fossils and four tested localities (Table 4). Carbon 13 values ranged within the low positive to high negative values from 5.03 ‰ to -1.46 ‰. Oxygen 18 values

ranged from -5.13 ‰ to -9.19 ‰. No patterns were observed to separate the Hell Creek samples from the Ludlow samples. Fossil samples appear to have slightly lower $\delta^{13}C$ values, and slightly higher $\delta^{18}O$ values than the nodule samples.

Table 4. $\delta^{13}C$ and $\delta^{18}O$ isotope results for four fossil and four nodule samples.

Sample	Locality	Stratigraphy	Specimen No.	Type	$\delta^{13}C$ VPDB	$\delta^{18}O$ VPDB
T8	L6466	Hell Creek	– – –	Nodule	3.05	-5.13
T13	L6521	Hell Creek	– – –	Nodule	3.31	-7.14
T15	L6809	Ludlow	– – –	Nodule	3.77	-7.37
T18	L6808	Ludlow	– – –	Nodule	5.03	-7.33
T33 (T15)	L6809	Ludlow	S4705, S4706	Two Gastropods	3.06	-8.33
T34	L6466	Hell Creek	S4702	Unionoid	2.68	-7.63
T35	L6466	Hell Creek	S4703	Unionoid	-1.46	-8.96
T36	L6808	Ludlow	S4707, S4708	Two Gastropods	3.30	-9.19

Scanning Electron Microscopy EDS Results

Electron dispersive spectrometry (EDS) results are semiquantitative and should be viewed as guidelines for compositional content and not as exact values. EDS results and SEM photos of sampled locations are in Appendix B. Silica was identified in all of the samples, ranging from less than 1 % to 47 % weight percent. Aluminum was observed in the *Sphaerium* sp. (S4712, Locality L6521) sample, indicating some clay content; however, the samples were not cleaned prior to analysis so the clay content may relate to the surrounding matrix, and not to the fossil composition. Tiny, silica replaced gastropods (Figure 14) were observed in the core of the Locality L6809 *Campeloma* sp. nodule. The chert cores of the nodules from localities L6521 and L6809 also contained a significant weight percent of siderite. Microscopic rhombic crystals of hematite were

observed on the exterior of the *Campeloma* sp. (S4725, Locality L6809). Hematite can occur from the diagenesis of either siderite or goethite. The hematite crystals on the fossil are presumed to be a late diagenetic alteration of the earlier iron mineral.

Figure 14. Silica replaced, distorted gastropod specimen S4726 (Locality L6809). The specimen was found in the chert core of a nodule containing a *Campeloma* sp. specimen. The image is magnified 400 times.

Calcium provided the major metal constituent in two of the *Campeloma* sp. (S4725, Locality L6809) specimen runs and two of the runs on the sample of nodule T13 (Locality L6521, Table 5). Since both samples had observable attached calcite cement, the calcium content may have been due to calcite preserved in the sample, or as cement unintentionally included in part of the analysis. Overall, magnesium replacement was found to be fairly low. Manganese replacement was slightly higher than magnesium replacement in most runs. One anomalous EDS run on the *Sphaerium* sp. (S4712, Locality L6521) specimen was found to contain 45.5 % manganese. Calcium content varied from unmeasurable to greater than 60 % of the metal content. Siderite was found to be relatively pure in the *P. percorrugata* (S4704, Locality L6466), *Sphaerium* sp.

(S4712, Locality L6521), and in the *Campeloma* sp. nodule (Locality L6809). In contrast, the *Campeloma* specimen (S4725, Locality L6809) and nodule T13 (Locality L6521) were found to be highly oxidized and the iron was extensively replaced by calcite.

Table 5. Standardized SEM weight percentages for metals

Sample	Fe	Mg	Ca	Mn
L6466 S4704 *Proparreysia percorrugata* (Whitfield)	87.8	2.9	3.7	5.7
	91.3	1.8	4.2	2.7
	94.3	0.0	4.2	1.5
	85.7	2.9	2.8	8.6
	89.3	1.3	2.2	7.2
L6521 S4712 *Sphaerium* sp.	83.0	9.7	0.0	7.3
	79.6	6.2	0.0	14.2
	89.1	5.0	0.0	5.8
	88.1	3.2	0.0	8.7
	91.4	1.7	0.0	7.0
	51.8	1.1	1.6	45.5
L6809 S4725 *Campeloma* sp.	88.4	1.4	4.7	5.5
	38.3	2.4	56.1	3.2
	35.6	2.3	60.0	2.1
	86.2	2.6	7.1	4.0
	76.2	5.6	14.0	4.1
L6809 *Campeloma* sp. Nodule	86.1	0.7	8.2	5.0
	92.6	1.0	2.9	3.5
	87.5	1.9	6.8	3.8
L6521 Nodule T13	71.9	4.8	18.0	5.3
	69.8	2.6	17.1	10.6
	29.3	2.2	64.3	4.1
	43.4	2.2	53.0	1.4

CHAPTER IV

DISCUSSION

Composition

All of the nodules analyzed with XRD displayed an inner rind composed of siderite, quartz, and varying amounts of goethite. The outer rind contains a slightly less crystalline content of goethite, quartz, and varying amounts of siderite. The working hypothesis is that because of the inverse nature of the siderite and goethite in the nodules, with siderite content and crystallinity decreasing from the center outward and goethite increasing from the center outward, siderite was the original ironstone mineral. Goethite commonly forms from the oxidation of iron minerals, such as siderite and pyrite, and is presumed to be the weathering remnant of the original siderite that preserved the fossils and formed the associated nodules. This hypothesis is supported by the reaction mechanics. A strongly reducing environment and bacterial mediation is necessary to convert goethite to siderite. Siderite, however, easily oxidizes to goethite when exposed to air. It is unlikely that there was a prior iron mineral that created the nodules and was converted to or replaced by siderite, because such a mineral would presumably leave at least a trace amount of original material to be identified in the XRD curves. Similarly, it is thermodynamically difficult to replace iron oxides or iron sulfates, the other candidates for nodule formation, with siderite (Faure, 1998).

The strong quartz peaks observed in many of the XRD curves are due to the

inevitable inclusion of chert core in many of the internal samples. The inclusion of silt- and fine sand-sized quartz grains in the structure of the nodules and fossils could also account for some of the quartz in the samples. Quartz is much less susceptible to weathering than iron minerals, especially siderite. A more crystalline structure would result in the strong quartz readings, even if the quartz weight percentage was not very high.

Thin and discontinuous calcite deposits were present on the exterior of the nodules and fossils. Calcite was also present along the edges of fractures through the nodules. The XRD curves of many of the nodules and three of the fossils contained a weak peak at 29.5 ^{o}2 Theta, which matches the major peak for calcite. Because calcite has only one strong peak and the samples had very poor crystallinity, minor peaks were not noticeable and identification could not be ascertained. A peak at 28.0 ^{o}2 Theta, tentatively identified as pyrolusite, is a similar situation without minor peaks to verify the identification. Pyrolusite would be a reasonable mineral for the manganese associated with siderite to form upon oxidation.

Fossil Preservation

Two possible scenarios will be discussed for the preservation of the fossils under study. The first scenario considers a situation in which the fossils were composed of aragonite and direct replacement of the calcium in the sediments and shells with dissolved iron from the surrounding groundwater resulted in the siderite external casts. The second scenario considers the possibility that the siderite was precipitated directly from the groundwater, forming casts around the calcite shells, which were subsequently

dissolved. These two scenarios are not mutually exclusive, and it is likely that they were both occurring to preserve the mollusks and create the nodules, as will be discussed later.

Aragonite was chosen as the likely replaced mineral in the first scenario rather than calcite due to the inherently less stable nature of aragonite at surface conditions. XRD results from the Montana specimens indicated that many of the freshwater mollusks in the area were either completely or partially composed of aragonite. Allison and Pye (1994) described a modern situation in which ferrous iron was observed to replace the calcium in aragonite to form siderite. The aragonite shells in the modern fossiliferous siderite concretions were found to be more sideritized than the calcite shells.

Because many of the fossilized mollusks retain much of the original morphology of the shell, most notably those from Locality L6466, it is very likely that a replacement reaction such as

$$CaCO_3(\text{aragonite}) + Fe^{2+}_{(aq)} \rightarrow FeCO_3 + Ca^{2+}_{(aq)} \quad (1)$$

was occurring. In a dissolution and precipitation situation, the fine details of shell morphology are less likely to be preserved. External molds and steinkerns would also compose a greater percentage of the preservation than external casts in a dissolution-precipitation situation. This is not the case at localities L6466, L6521, L6799, and L6808. External casts are difficult to distinguish from steinkerns at Locality L6809 due to the high level of weathering. The free energy of reaction for the replacement of aragonite by siderite is

$$\Delta G^{o}_{rxn} = [-159.3 + (-132.2)] - [-269.7 + (-18.9)] = -2.9 \text{ kcal/mol}, \quad (2)$$

indicating that at standard state conditions, the reaction will move in the forward direction and ferrous iron will replace calcium to form siderite. Gibbs' free energy calculations were performed using the standard free energy of formation values from Woods and Garrels (1987), as compiled in Appendix B of Faure (1998).

The K value for the replacement of calcium in aragonite with ferrous iron is$10^{2.13}$, using Woods and Garrels' (1987) energies of formation; therefore, the equilibrium Law of Mass Action equation for the reaction is:

$$K = 10^{2.13} = 133.6 = \frac{Ca^{2+}}{Fe^{2+}}. \quad (3)$$

At standard state conditions and stated thermodynamic information, the ratio of calcium ion activity to ferrous iron activity must equal 133.6 or less in order for iron to replace calcium within aragonite. This indicates that the calcium and ferrous iron activities cannot be more than two magnitudes of difference apart in order to force the reaction in the forward direction. This is different from a precipitation situation in which ratio of calcium to ferrous iron would need to be greater than the solubility constant in order to supersaturate the water and force precipitation. Standard state conditions for a water sample are T = 25^{o}C, P = 1 atm, and the activity of all ions and molecules in the water is equal to 1 mol/kg. In real water samples, standard state is nearly impossible to achieve; therefore, the results of reactions at standard state only provide a guide as to the more favorable reaction direction.

Thermodynamic values for the energy of formation are currently variable and depend on which data compilation is used. Because of this variability, an exact ratio

value, such as the example provided above, cannot be determined for this equation. Values of K calculated for the equation ranged from $10^{2.09}$, using the LLNL data in GWB, to $10^{2.9}$ using data from Weast et al. (1986), as compiled in Appendix B of Faure (1998). Research in this area, therefore, must focus on whether products are favored at reasonable ratios using several sets of thermodynamic data in order to determine that the information is valid. Research into the effects of variables, such as pH and temperature, on the ratio could also help determine the likelihood of the reaction's occurrence.

The GWB subprogram Rxn was used to input various temperatures, pH values, and activities for calcium and ferrous iron to determine how these variables might affect ferrous iron replacing calcium in aragonite to form siderite in a real-world situation. All program calculations and results are included in Appendix C. At standard state, products were favored and a K value of $10^{2.09}$ was calculated. Varying pH values did not affect whether products or reactants were favored. Variable pH was not expected to affect the outcome since the activity of hydrogen ions is not considered in the equation. The solubility of both aragonite and siderite, as well as calcite, is pH dependent, indicating that the stability of the final mineral, whether aragonite, calcite or siderite, will depend on the pH.

Varying the activities of the two dissolved species only changed the preferred direction of the reaction if the ratio of the activities became greater than the K value of 100 or $10^{2.09}$. Increasing the temperature from 10°C to 30°C increased the Ca^{2+}/Fe^{2+} ratio for replacement from 100 to 125. High temperature pore waters would appear to be

slightly more amenable to the replacement of aragonite by siderite than cooler temperature pore waters.

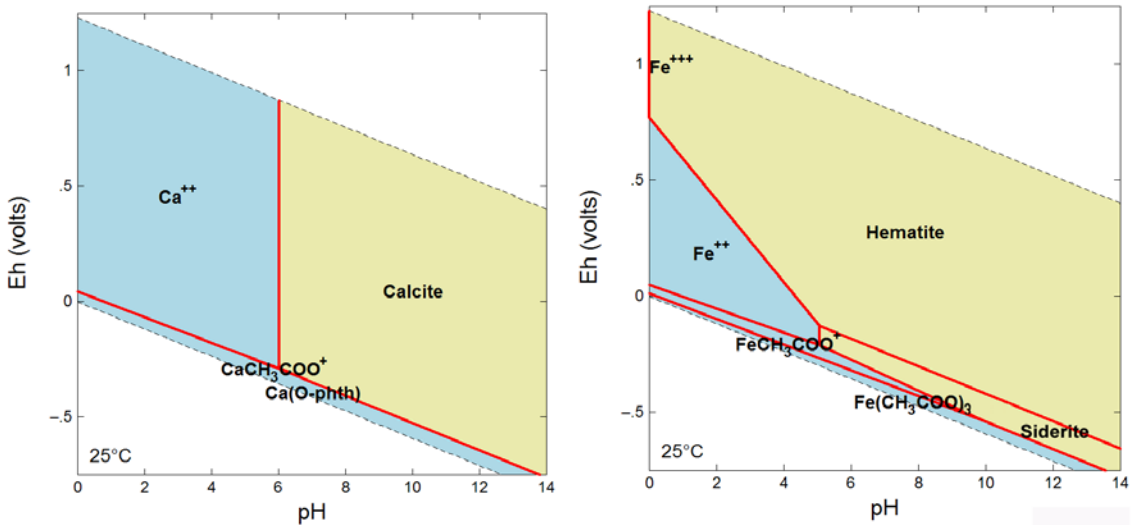

Figure 15. Eh-pH stability diagrams for calcium (left) and iron (right) minerals and dissolved species. Standard state conditions: 1 atm pressure, 25°C, fCO_2 = 0.003, $[Ca^{2+}]$ = 1 mol/kg, $[Fe^{2+}]$ = 1 mol/kg.

An appropriate ratio of dissolved calcium to iron within a natural water is possible, based on thermodynamic calculations, to allow for siderite replacement of aragonite. Why, then, is siderite replacement of aragonite shells not more common? Figure 15 shows Eh-pH stability diagrams for calcium and iron minerals, and dissolved species, at standard state. The calcite and siderite stability fields cover approximately the same span of pH values; however, while calcite exists at all possible Eh values within the stability field of water, siderite is only stable within a thin span of very reducing conditions. At the modeled activities for iron and calcium, iron will be able to replace the calcium ion in aragonite at any pH where calcite is stable, but only when the Eh of the

system is very low. At conditions more oxidizing than siderite tolerance, aragonite will alter into the more stable calcite, or simply dissolve.

Groundwater Geochemistry

The second possibility for the sideritized preservation of freshwater mollusks within the Hell Creek Formation is the direct precipitation of siderite from iron carbonate saturated water. This is presumed to be the mechanism for the formation of the nodules since no evidence of replacement was observed within the nodules. Siderite would have precipitated around the chert cores and shells forming iron carbonate external molds and steinkerns of the aragonite shells, which were subsequently dissolved. This scenario does not depend on the activity of calcium in the water or amount of calcium carbonate in contact with the system, but does depend on the activity of ferrous iron and the fugacity of carbon dioxide acting upon the system. The activity of sulfur must also be considered in this scenario. Pyrite formation is much more common than siderite formation and often occurs with siderite formation in marine waters, which is an indication that a reaction between iron and sulfate is thermodynamically more favorable than a reaction between iron and carbonate. Pyrite was not observed in either the XRD or SEM elemental analyses.

Eh-pH diagrams created for siderite stability have historically been very limited. Thermodynamic data, as discussed earlier, is variable and difficult to find for temperatures other than 25^{o}C. In order to try to effectively understand how siderite stability is affected by a range of variables, such as temperature, pH, CO_2 fugacity, and water composition, several diagrams must be created with multiple variable

combinations. Hand drawing, or even computer drafting, of Eh-pH diagrams requires extensive amounts of time to calculate the appropriate equations. The equations must then be combined in a graph form delineating stability and dominance zones. Limited knowledge on interactive species, and the complexity of considering minor species as well as the major ones, have limited the information included in earlier diagrams. Researchers have thus generally been restricted by these practical considerations to the creation of one or two stability diagrams. The diagrams are usually calculated at 25°C, an unrealistic temperature for most groundwaters.

The computer program Geochemist's Workbench® (GWB) was utilized in an attempt to create a wider range of stability diagrams and try to determine whether the stability range of siderite could be better constrained. Specifics of the program are discussed in the Methods section. The subprogram Act2 was employed to create Eh-pH diagrams (Appendix D). Act2 uses the Lawrence Livermore National Laboratories (LLNL) database as the default database for thermodynamic information. The range of possible species included in the calculations is greatly expanded by the computer's ability to solve equations quickly. The program allows calculations at varying temperatures, pressures, with additional chemical variables, and at varying activities and fugacities of the various constituents.

An initial diagram of ferrous iron species was created with the properties of 1 atmosphere of pressure (atm), a temperature of 10°C, a CO_2 fugacity of 0.003 atm, an iron activity of 10^{-7} mol/kg, and a sulfate activity of 10^{-2} mol/kg. The activities for iron and sulfate were arbitrarily chosen to represent a high-sulfate, low-iron groundwater

environment. The fugacity of carbon dioxide was chosen to represent an open ground water system near the surface-water interface under conditions like those found today. The resultant Act2 diagrams are in Appendix D.

Temperature was kept constant at 10°C while iron and sulfate activities and carbon dioxide fugacity were changed individually, and then in combination, to determine the effect on the stability of siderite of increasing or decreasing each constituent. An initial temperature of 10°C was used because it is the conventional ground water temperature used for modern geochemical calculations. Two diagrams were also created using the full suite of likely groundwater constituents. Temperature was then increased to 30°C to simulate the possible increased groundwater temperature in a subtropical zone, which is hypothesized for this geographic area during the Maastrictian and early Paleocene. The same simulations with small changes were run with the higher temperature. Activities were increased or decreased by a factor of ten. Fugacity was increased by 0.003 atm increments. A constant pressure of 1 atm was maintained through all simulations.

The initial simulation resulted in a wedge-shaped area of dissolved iron carbonate with a basic pH range (> 8) (Figure 16). Increasing CO_2 partial pressure widens the wedge at the expense of the hematite field, but does not cause the siderite to precipitate. Decreasing sulfate activity also vertically increased the iron carbonate wedge, but at the expense of the pyrite field. Siderite did not precipitate even at sulfate activities as low as 10^{-8} mol/kg. The pyrite field, however, does not decrease significantly even at such low sulfate activities. Increasing the activity of iron to 10^{-6} mol/kg immediately causes

siderite to precipitate, although the iron carbonate wedge reduces in area both laterally and vertically. The siderite stability field exists at pH values greater than 11, which would be toxic in a natural system. After the first increase in iron activity, continuing to increase the activity of iron does not appear to change the field shape or size. The hematite field, however, does spread laterally with increased iron activity. Combining increased iron with increased carbon dioxide and decreased sulfate activity expands the siderite field both laterally and vertically at the expense of hematite and pyrite. When the two variables are changed drastically, the stability field of siderite expands to a minimum pH of 7.5, but continues to expand vertically. At this point, increasing the iron activity allows the field to expand into the mildly acidic zone.

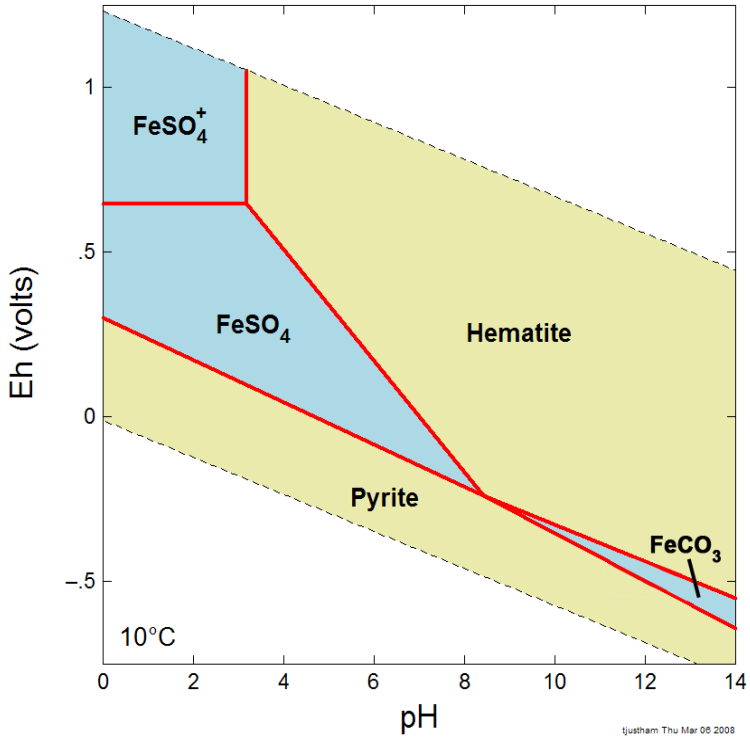

Figure 16. Initial diagram for the 10°C series of simulations. Conditions:1 atm, fCO_2 = 0.003, $[Fe^{2+}] = 10^{-7}$ mol/kg, $[SO_4^{2-}] = 10^{-2}$ mol/kg. Dark gray areas indicate dissolved species. Light gray indicates solid species.

In order to determine the effects of other common porewater constituents on the stability of siderite, two simulations were run with common aqueous ions. Ions of chloride, sodium, manganese, magnesium, and calcium were added to the list of ions interacting with the ferrous iron. The additional ions changed the iron carbonate wedge to a more triangular shape (Figure 17). The right side of the wedge lost space to a field of ferrite-magnesium creating the triangular shape. Increasing the iron activity from 10^{-7} mol/kg to 10^{-6} mol/kg again created a siderite field from the aqueous iron carbonate field. The field area was relatively small due to the space lost to ferrite-magnesium, but increased in size both laterally and vertically with increased fugacity of carbon dioxide and decreased sulfate activity.

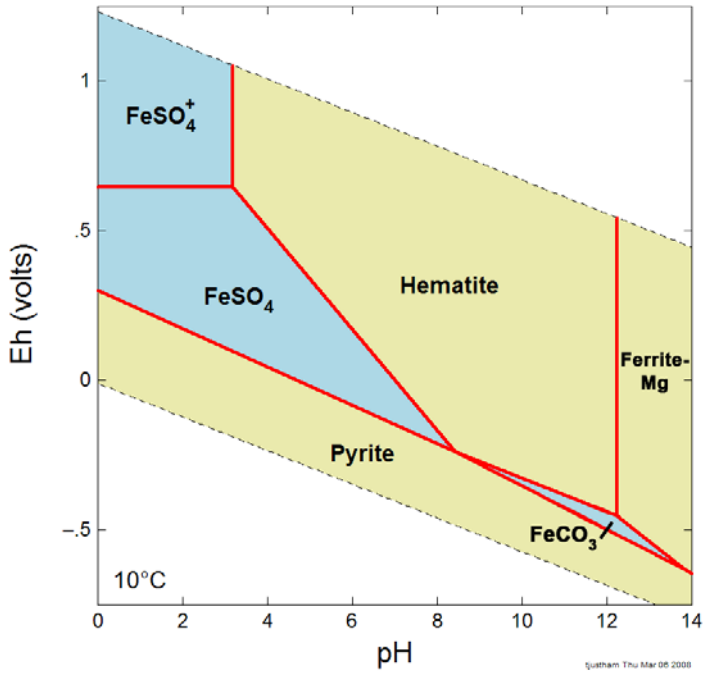

Figure 17. Eh-pH diagram created for iron species with interactions from major ions often found in modern ground waters. Conditions: 10°C, 1 atm, fCO_2 = 0.003, $[Fe^{2+}]$ = 10^{-7} mol/kg, $[SO_4^{2-}]$ = 10^{-2} mol/kg, $[Na^+]$ = 10^{-4} mol/kg, $[Mn^{2+}]$ = 10^{-6} mol/kg, $[Mg^{2+}]$ = 10^{-2} mol/kg, $[Ca^{2+}]$ = 10^{-2} mol/kg, $[Cl^-]$ = 10^{-3} mol/kg. Dark gray areas indicate dissolved species. Light gray indicates solid species.

The latest Cretaceous and early Paleocene climates were much warmer in the Williston Basin than they are today (Johnson, 2002). In order to determine how warmer ground water may have affected the formation and stability of siderite, Eh-pH diagrams were also created with a water temperature of 30°C (Figure 18). With the increased temperature, a siderite stability field exists in the initial simulation. The field is a very small wedge-shaped area at pH values greater than 12, and is shared with magnetite. Increasing the fugacity of carbon dioxide and decreasing the activity of sulfate each produces similar results as at 10°C, except the fields also spread laterally. Increasing iron content does not appear to enlarge the siderite stability field, even at activities of 10^{-1} mol/kg.

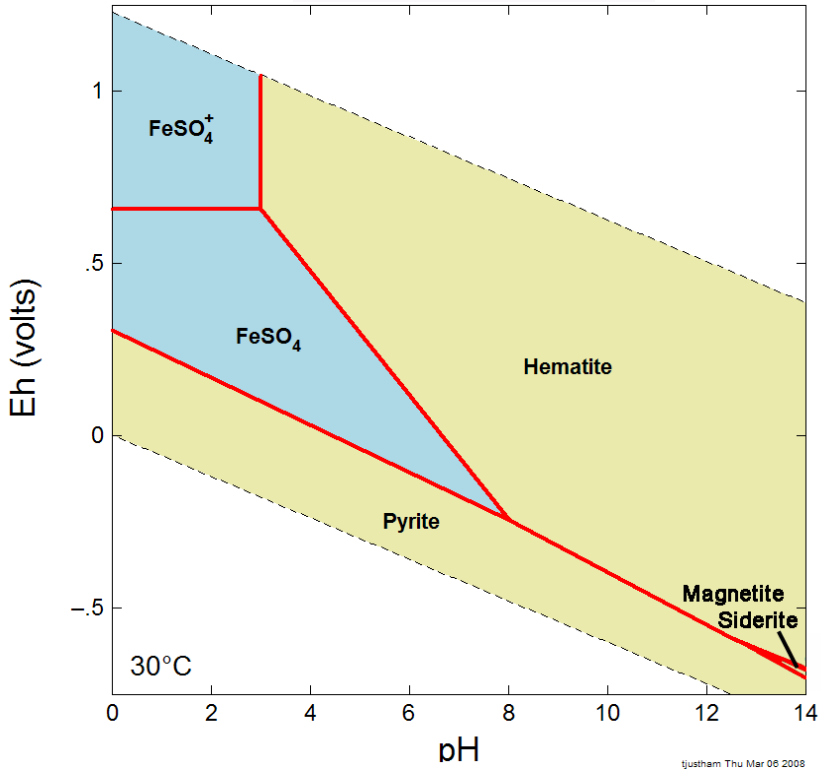

Figure 18. Initial diagram for the 30°C series of simulations. Conditions:1 atm, fCO_2 = 0.003, $[Fe^{2+}] = 10^{-7}$ mol/kg, $[SO_4^{2-}] = 10^{-2}$ mol/kg. Dark gray areas indicate dissolved species. Light gray indicates solid species.

Numerous compilations of thermodynamic information exist. In order to determine if the results of the LLNL dataset are consistent with those from other datasets, comparison diagrams were created using thermodynamic data from MINTEQ, PHREEQC, and WATEQ4F datasets. MINTEQ, PHREEQC, and WATEQ4F all require an extremely low sulfate activity, on the order of 10^{-9} mol/kg or less, and an increased CO_2 partial pressure in order to develop a siderite stability field. Increases in iron activity do not cause a precipitation of siderite using MINTEQ and WATEQ4F databases, and does not affect the size or shape of the field once it forms. PHREEQC requires an increase in iron activity to 1 ppm (10^{-6} mol/kg) in order to precipitate siderite, similar to the LLNL database. The thermodynamic information from all three databases results in small siderite zone wedges similar to the one formed by LLNL data, but situated at much higher pH values. Increases in the fugacity of carbon dioxide and decreases in the sulfate activity expand the size of the siderite field in both the laterally and vertically.

Interestingly, the shape and width of the siderite field within an Eh-pH diagram for iron depends on the carbon species that is used to create the diagram. The partial pressure of carbon dioxide within the system has been kept constant in the analysis for this discussion because it was assumed that carbon dioxide would be the carbon species that remains the most constant within the system. The sediments composing the Hell Creek Formation and Ludlow Member in this area do not appear to have a significant carbonate mineral composition to have contributed to the dissolved carbonate species. Garrels (1960), used a constant carbonate activity to create an Eh-pH diagram relating iron species. Diagrams were created in GWB Act2 using both carbonate and bicarbonate

to compare with the carbon dioxide results. Keeping CO_2 fugacity constant results in a thin wedge-shaped field ranging in pH from neutral to very basic, and roughly parallel to the lower stability line for water. Holding the carbonate or bicarbonate activity constant results in a triangular-shaped field, which ranges in pH from neutral to 10, and extends into more oxidizing environments.

In order for siderite to precipitate from a natural water and remain stable, the sulfur activity must be fairly low. The partial pressure of carbon dioxide can increase the stability field for siderite, but the effect of increased CO_2 fugacity appears to be limited by large concentrations of sulfur. Iron activity must be at least 1 ppm to precipitate siderite, which is not uncommon in modern systems. Continuing to increase iron activity above 1 ppm does not appear to increase the range in which siderite is stable. Deposits similar to the Hell Creek Formation are reported in Holocene marshes and sandflats of the North Norfolk coast of England. Dissolved iron concentrations within the modern system rarely exceed 1 ppm, which matches the conclusions presented by the Eh-pH diagrams. Unlike the replacement reaction where ferrous iron replaces the calcium in aragonite to form siderite, the combination of CO_2 and Fe^{2+} to precipitate siderite directly from water does not appear to depend significantly on the concentration of iron within the water, once the iron activity is above the critical level of 1 ppm. If the sulfate activity is significantly reduced, iron will preferentially combine with carbonate species in place of sulfate at high pH values. The two scenarios for shell preservation and nodule formation are not mutually exclusive assuming that the system has an appropriate ratio of calcium activity to iron activity, and a low sulfate activity. In both situations, the pH must

be basic, and the system must exist in a very reducing environment. Siderite formation probably began with the replacement of calcium by iron in aragonitic molluscan shells, then continued with direct precipitation of siderite around the fossils and chert cores.

Porewater Composition

Using the relationship between authigenic siderite geochemistry and depositional environment developed by Mozley (1989), the three localities from the Hell Creek Formation and Ludlow Member analyzed using EDS appear to have formed in meteoric groundwater. Marine siderite is characterized by an extensive substitution of magnesium for iron, up to 41 mol% $MgCO_3$ (Mozley, 1989). The relatively low magnesium and high manganese content in the samples indicates that the siderite was formed in a freshwater environment with no marine influences. When the samples are plotted on a ternary plot with Fe, Mg and Ca (Figure 19), the *P. percorrugata*, *Sphaerium*, and L6809 nodule cluster together near the Fe corner. The *Campeloma* specimen and L6521 nodule plot closer to Ca, but do not appear to cluster. The ternary plot with Mn, Ca, and Mg indicates that none of the samples cluster based on this analysis. Both ternary plots show, as indicated before, that the magnesium content in all samples is relatively low compared to the other three constituents.

The isotopic composition of the eight analyzed sideritized fossils and nodules supports a model of continental formation. Seven of the eight samples had positive $\delta^{13}C$ values. A unionoid from Locality L6466, Specimen S4703, had a slightly negative value of -1.46 ‰, which is still well above -8 ‰, determined by Mozley and Wersin (1992) to be the high end for marine $\delta^{13}C$ values. The variability of $\delta^{18}O$ values in both marine and

continental siderites makes oxygen isotopes less reliable for determinations of depositional environment. Samples ranged in values from -5.13 ‰ to -9.19 ‰ for $\delta^{18}O$. All values were greater than the suggested -13 ‰ for continental waters; however, the measured $\delta^{18}O$ isotope values are still more negative than what would generally be expected from marine water that has not been depleted by mixing or sediment interactions (Mozley and Wersin, 1992).

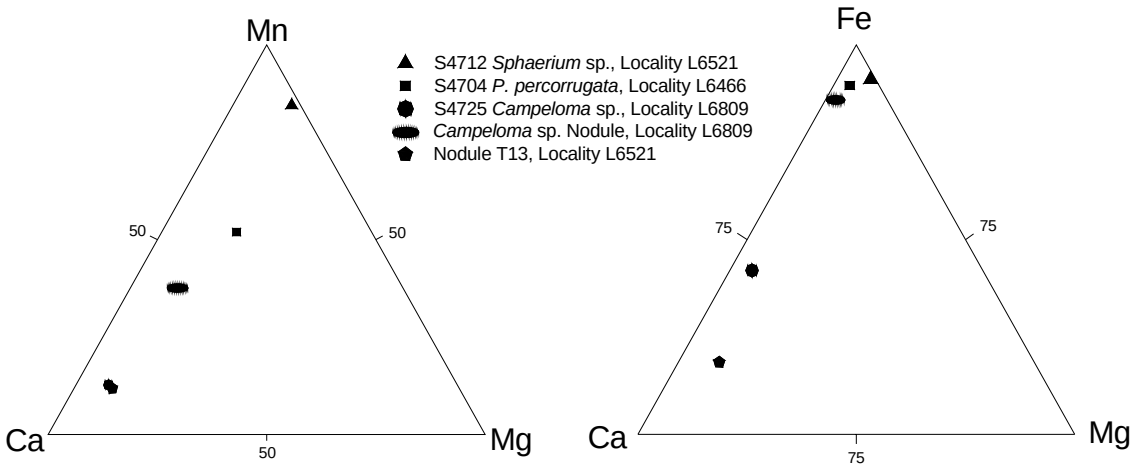

Figure 19. Ternary plots of metal elemental composition of the samples analyzed by the SEM EDS. The plots show clustering of the S4704, S4712, and the *Campeloma* sp. nodule on the right plot and no clustering on the left plot.

Organic Influences

Bacterial reduction of organics to produce the carbon dioxide used to form siderite at the localities should result in more negative $\delta^{13}C$ values in the siderite preserved mollusks than in the original mollusk shells (A.S. Engals, personal communication, February 7, 2008). Unfortunately, the Hell Creek and Ludlow strata in the study area do not produce any shells with original material to compare to the siderite preserved fossils. Comparisons to isotope analyses for well-preserved, age-equivalent

Hell Creek fossils from eastern Montana (Gibson, 1990) and basal Hell Creek fossils from western South Dakota (Cochran et al., 2003) indicates that the sideritized fossils are heavier in both $\delta^{13}C$ and $\delta^{18}O$. The lighter $\delta^{18}O$ values in Montana could be due to the increased altitude and distance from the seaway, but the lighter values for the South Dakota fossils are not as easily explained. Although a bacterial influence is assumed for siderite formation in general, due to the reducing environments within which it forms, without fresh shell material from the localities in question, it is difficult to provide evidence of a bacterial influence. Siderite preserved fossils appear to have slightly more negative $\delta^{13}C$ and $\delta^{18}O$ values than the siderite nodules. The apparent differences may be an artifact of sampling, or could be an indication of siderite replacement of the shells, which would have used the original carbonate in the shell structure.

Time Occurrence

Preliminary study of the possible timing of preservation for the fossils and development of the nodules indicates an early diagenetic time of formation, possibly during the burial process near the sediment-water interface. A late diagenetic formation time would require the replacement of an early formed nodule by siderite, or the growth of siderite nodules at the expense of the surrounding bedding structures. Frye (1967) and Groenewold (1971) both note that bedding surrounding the nodules is not disrupted or compacted. Bedding was even observed to continue through individual nodules. Thin sections of the nodules did not indicate significant grain replacement, other than the weathering of siderite to limonitic material (G.H. Groenewold, personal communication, March 14, 2008). XRD and SEM analyses did not provide evidence of any minerals

(clay, pyrite, etc.) that may represent an earlier form of the concretion that has since been replaced by siderite. An early diagenetic occurrence of sideritization is a preliminary hypothesis based on visual and chemical clues indicating that the nodules formed during early diagensis of the surrounding materials, and that siderite is the probable original mineral composition of the nodules. More research will be required in order to formally accept or reject the hypothesis.

CHAPTER V

CONCLUSIONS

This study of the ironstone preserved fossils and nodules in the rocks of the Hell Creek Formation and Ludlow Member of southwestern North Dakota supports the following conclusions:

1. All samples, both nodules and fossils, have been heavily weathered and oxidized.
2. XRD analyses have identified the current mineralogical composition of the ironstone fossils and nodules as siderite ($FeCO_3$), quartz (SiO_2), and goethite (FeOOH).
3. The increased content of siderite toward the core of the nodules, and the pervasiveness of siderite in the samples, likely indicates that siderite was the original iron mineral forming the fossiliferous nodules.
4. The majority of nodules, and some fossils, have a chert core, which is partly intermixed with the siderite rind.
5. Fossil gastropods, both microscopic and macroscopic, have been observed in the chert core, indicating a penecontemporaneous formation of the chert with shell deposition and burial.
6. Many of the mollusks, especially unionoids, appear to have been preserved by replacement of original aragonite with siderite, preserving shell ornamentation and structures.

7. Reaction calculations indicate that siderite replacement of aragonite is thermodynamically favorable, and therefore likely in appropriately reducing environments.
8. Eh-pH diagrams indicate that siderite precipitation requires a neutral to basic groundwater and a very reducing environment, which would require a significant amount of organic matter.
9. Manipulation of variables considered in the stability diagrams has indicated that siderite precipitation, without associated pyrite, requires low to non-existent sulfate activity, a relatively high fugacity of carbon dioxide, and ferrous iron activity of at least 10^{-6} mol/kg within the pore water.
10. SEM and isotope analyses indicate that the siderite was formed in a meteoric pore water environment.
11. A bacterial influence on the formation of siderite cannot be determined at this time from isotope analyses.
12. Preliminary research suggests an early diagenetic formation for the siderite nodules.

Future Work

This project was a preliminary investigation to constrain the geochemical conditions in the groundwater environment that produced the siderite preservation of freshwater mollusks through the Hell Creek and Ludlow strata of southwestern North Dakota. Various aspects of this project could benefit from continued research, such as further investigation of the chert cores prevalent in the siderite nodules and some of the

fossils. Constraining the chemical environment required for the formation of the cores, and attempting to determine their exact relationship to the fossils and nodules, would add to the overall understanding of this preservation. A paleontological comparison of ironstone-preserved fauna to the well-preserved and well-studied fauna of the Montana Hell Creek could provide information on differential sideritization and changing faunal assemblages across the landscape. Continued isotopic analyses for both siderite preserved mollusks and siderite nodules could provide more information for bacterial influence or the differences in formation between the nodules and fossils.

APPENDICES

Appendix A

X-ray Diffractometer Graphs

Abbreviations:

A – Aragonite ($CaCO_3$)

C – Calcite ($CaCO_3$)

G – Goethite (FeOOH)

P – Pyrolusite (MnO_2)

Q – Quartz (SiO_2)

S – Siderite ($FeCO_3$)

(?) Indicates an uncertain identification

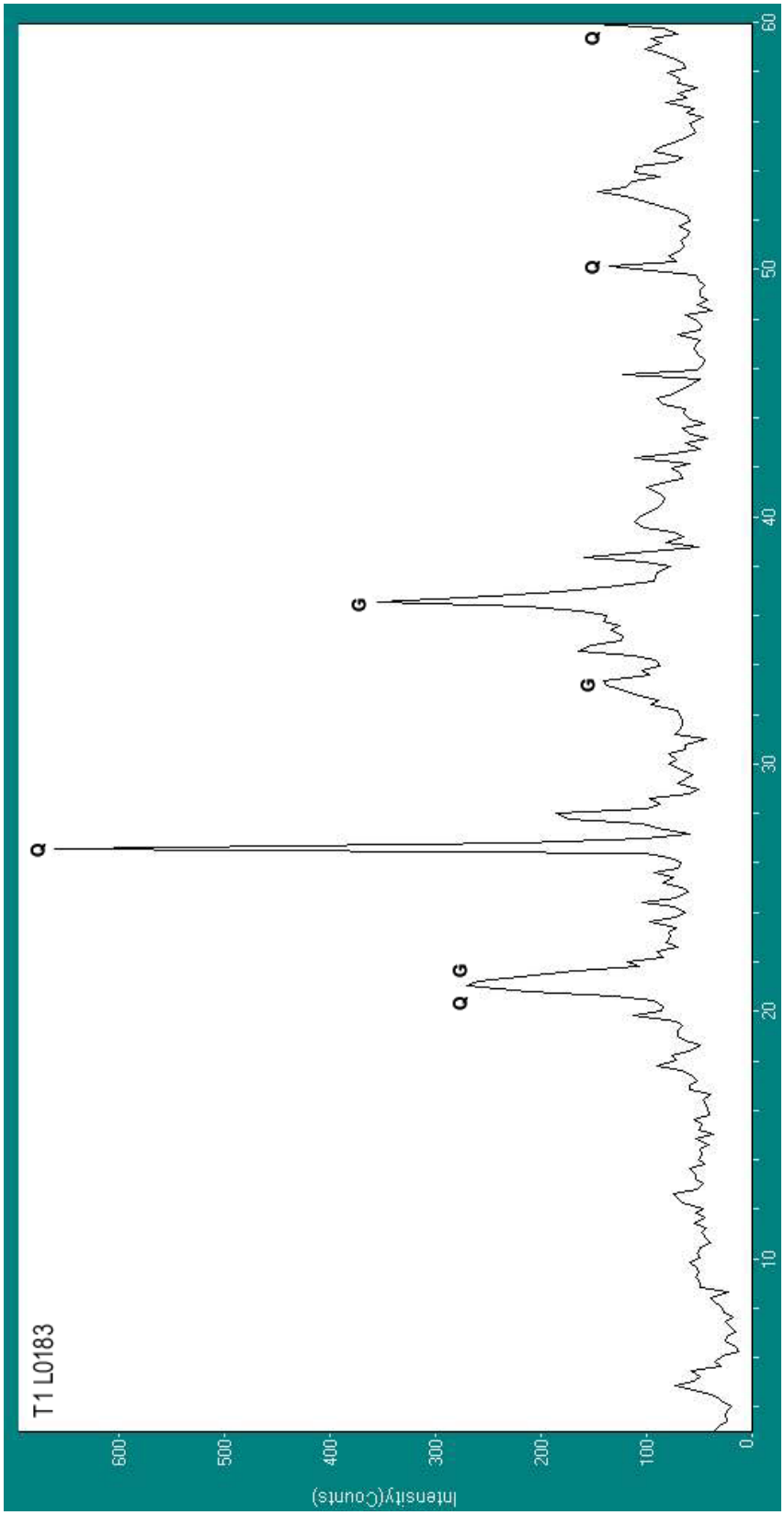
T1 L0183
Intensity(Counts)
Position [°2Theta]
Q
Q G
G
G
Q
Q

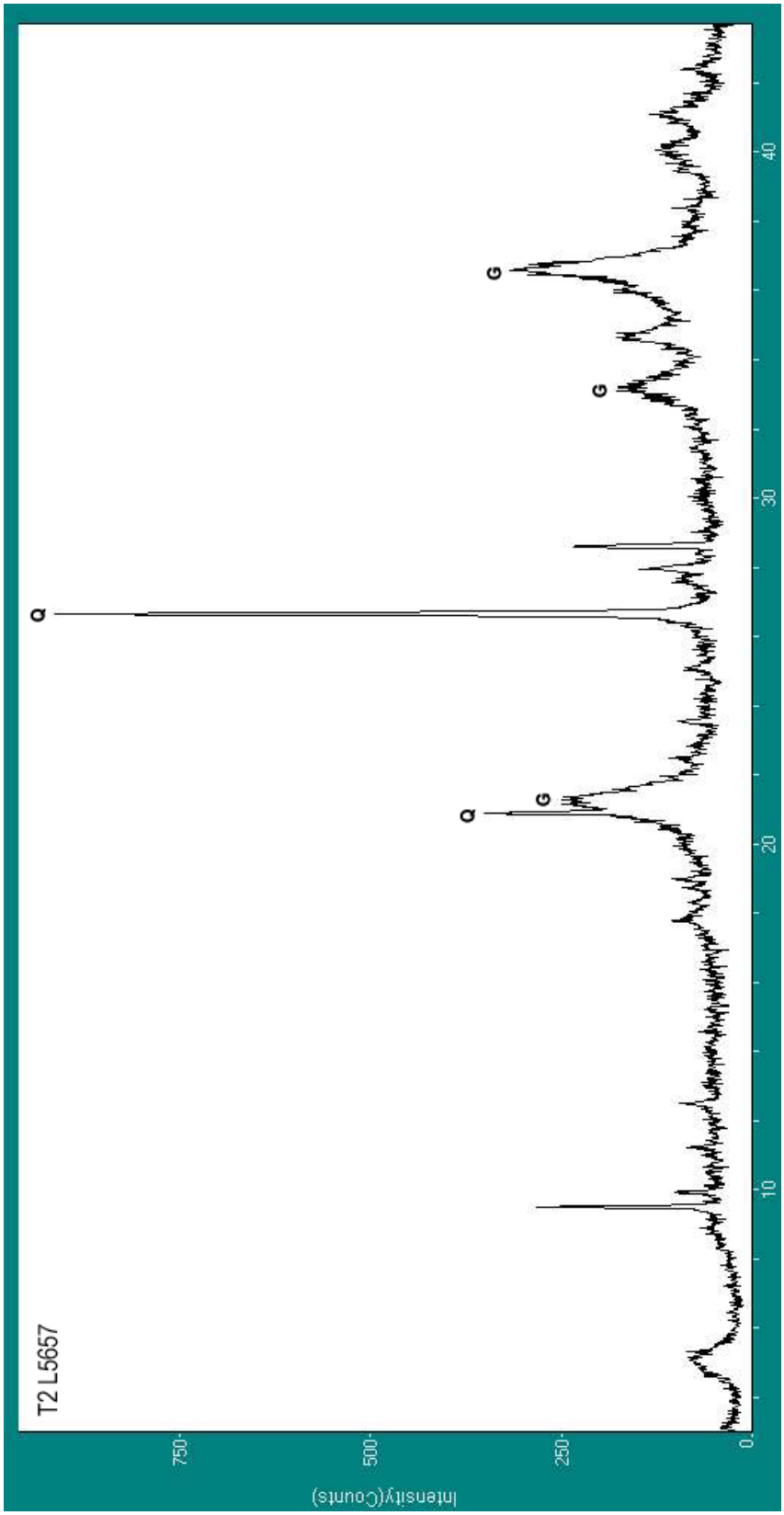
T2 L5657
Intensity(Counts)
0
250
500
750
Q
Q
G
G
G
10
20
30
40
Position [°2Theta]

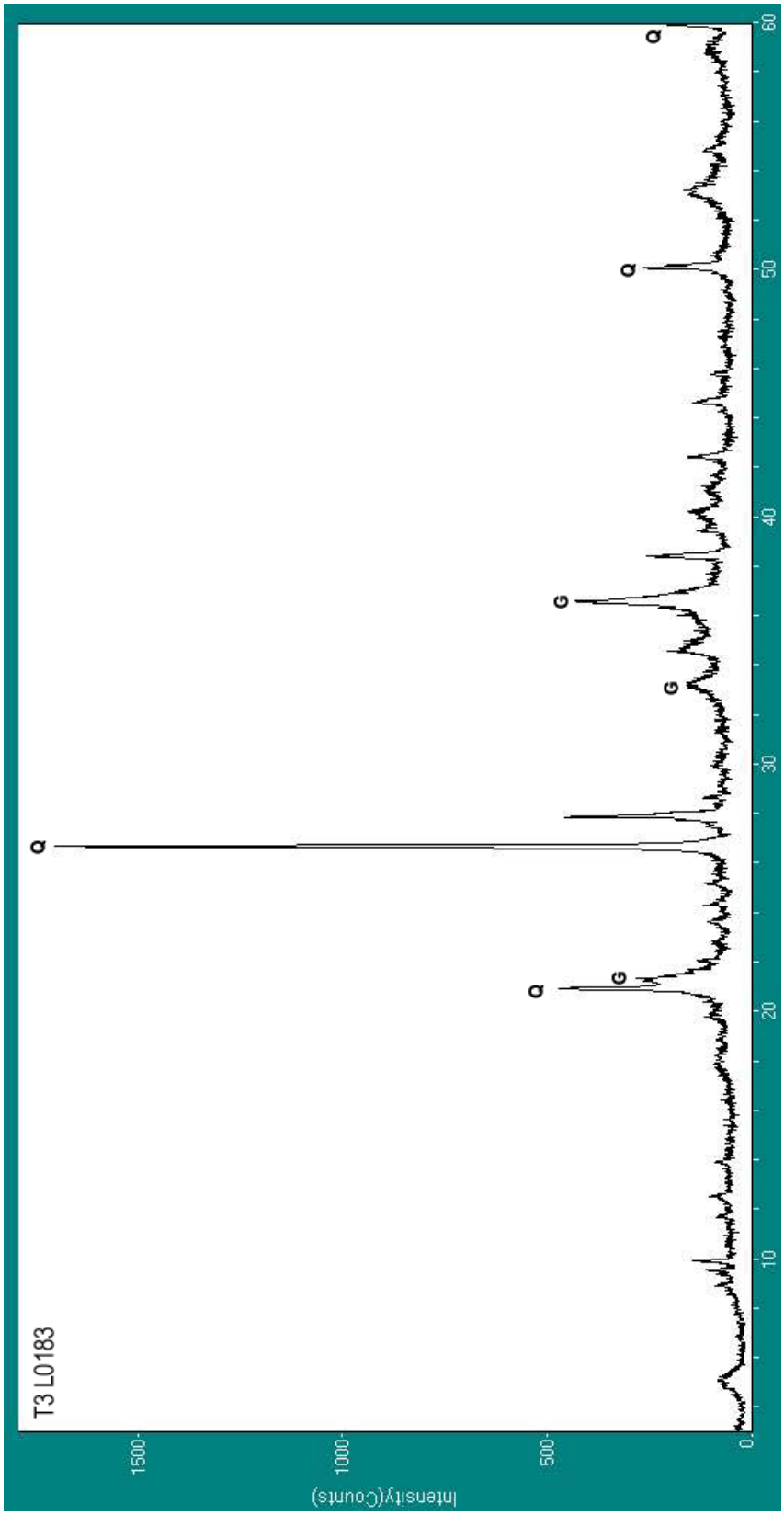
T3 L0183
Intensity(Counts)
1500
1000
500
0
10
20
30
40
50
60
Q
G
Position [°2Theta]

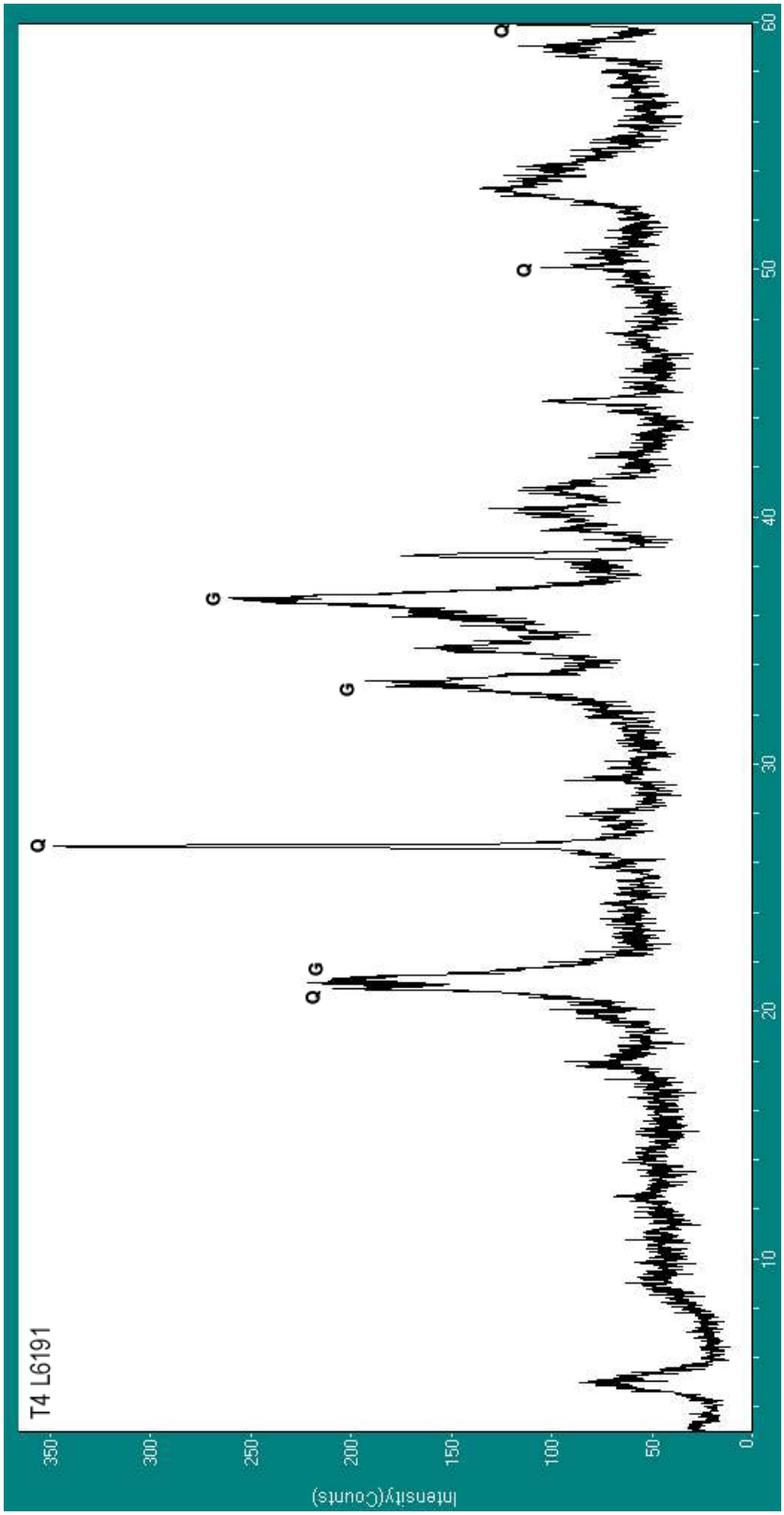
T4 L6191
Intensity(Counts)
Position [°2Theta]
Q
Q I G
G
G
Q
Q

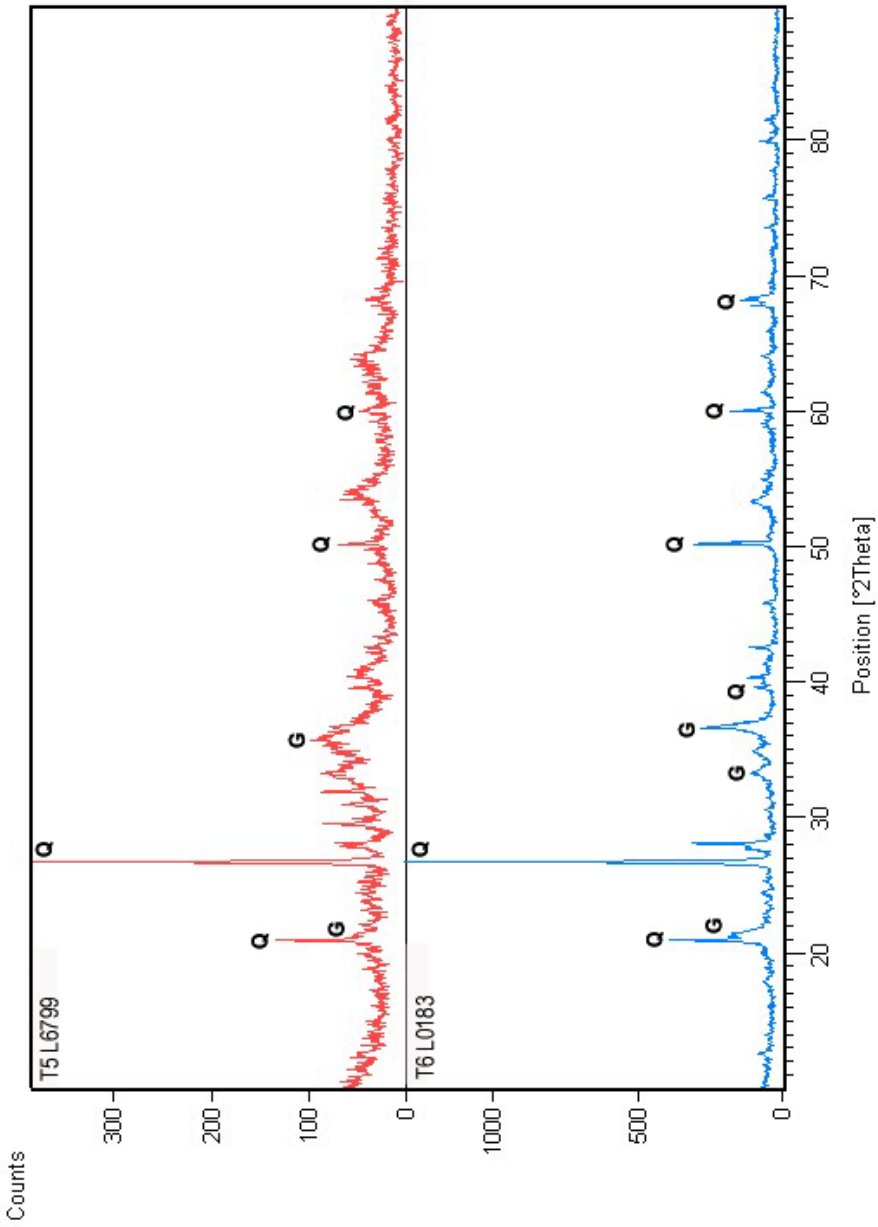
T5 L6799
T6 L0183
Counts
Position [°2Theta]
Q
G

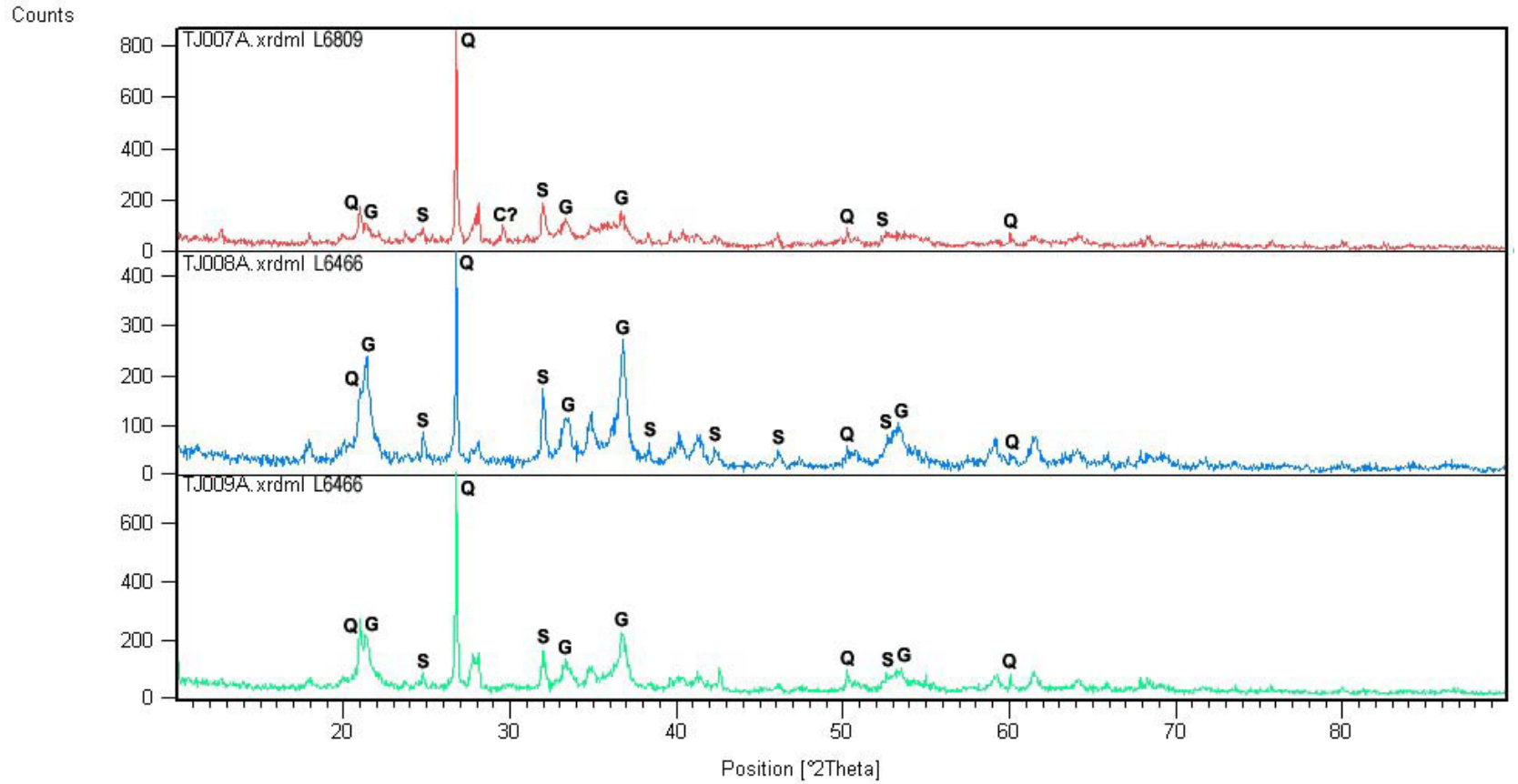
Counts
TJ007A.xrdml L6809
TJ008A.xrdml L6466
TJ009A.xrdml L6466
Q
G
S
C?
Position [°2Theta]

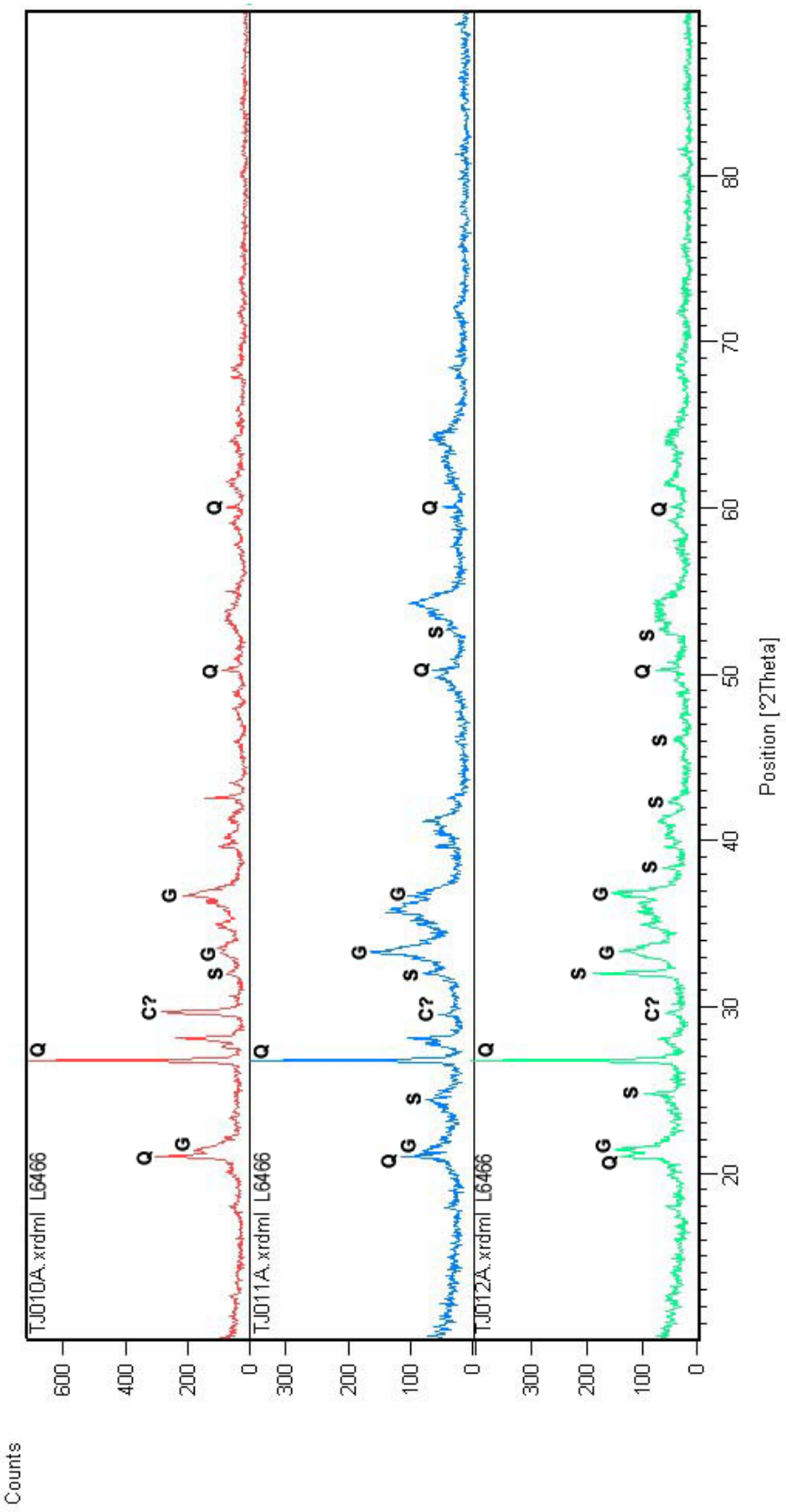
TJ010A.xrdml L6466
TJ011A.xrdml L6466
TJ012A.xrdml L6466
Counts
Position [°2Theta]
Q
G
S
C?

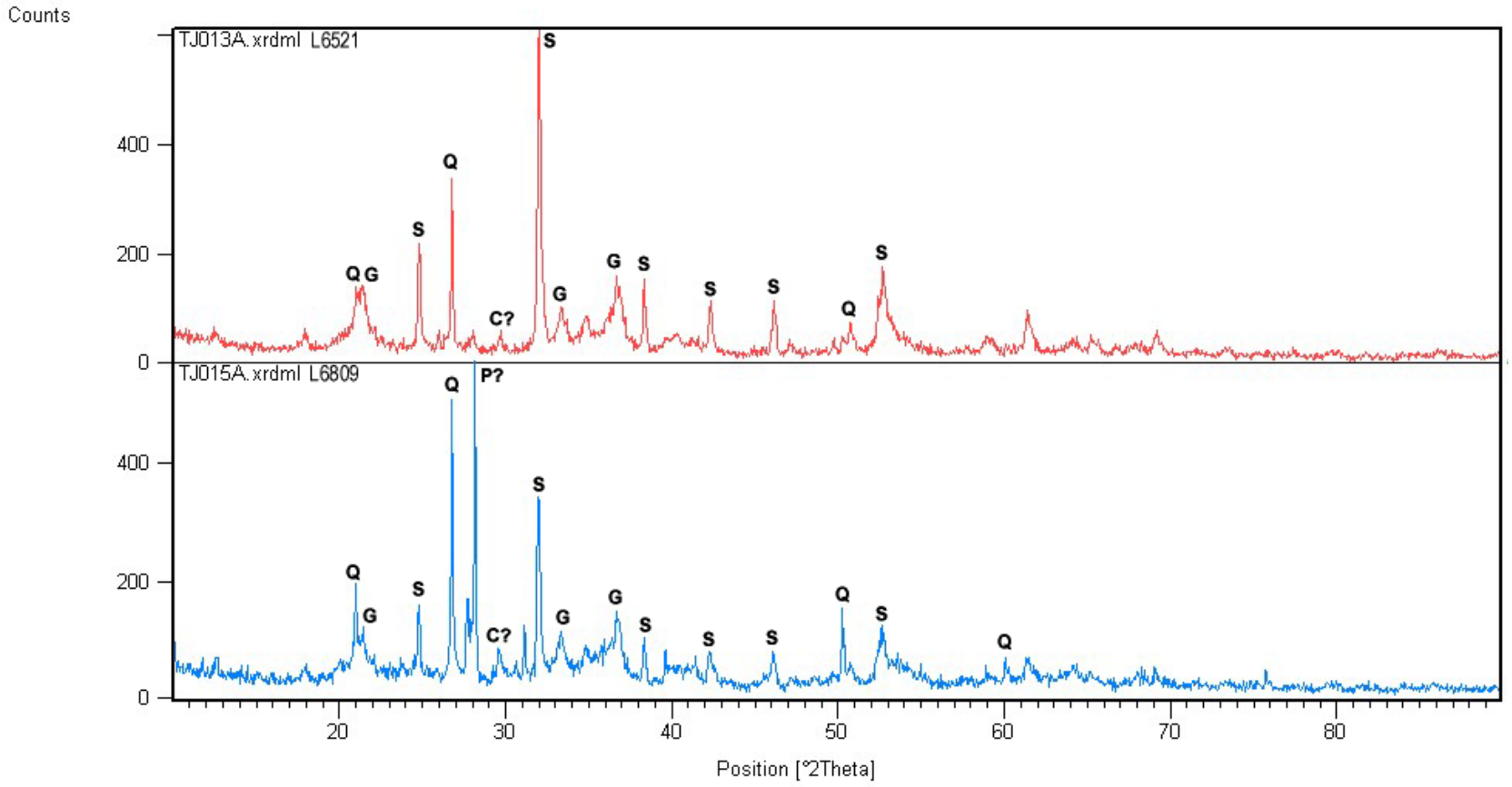
Counts
TJ013A.xrdml L6521
TJ015A.xrdml L6809
Q G
S
Q
S
C?
G
G S
S
S
Q
S
P?
Q
S
G
S
C?
G
G
S
S
S
Q
S
Q
0
200
400
20
30
40
50
60
70
80
Position [°2Theta]

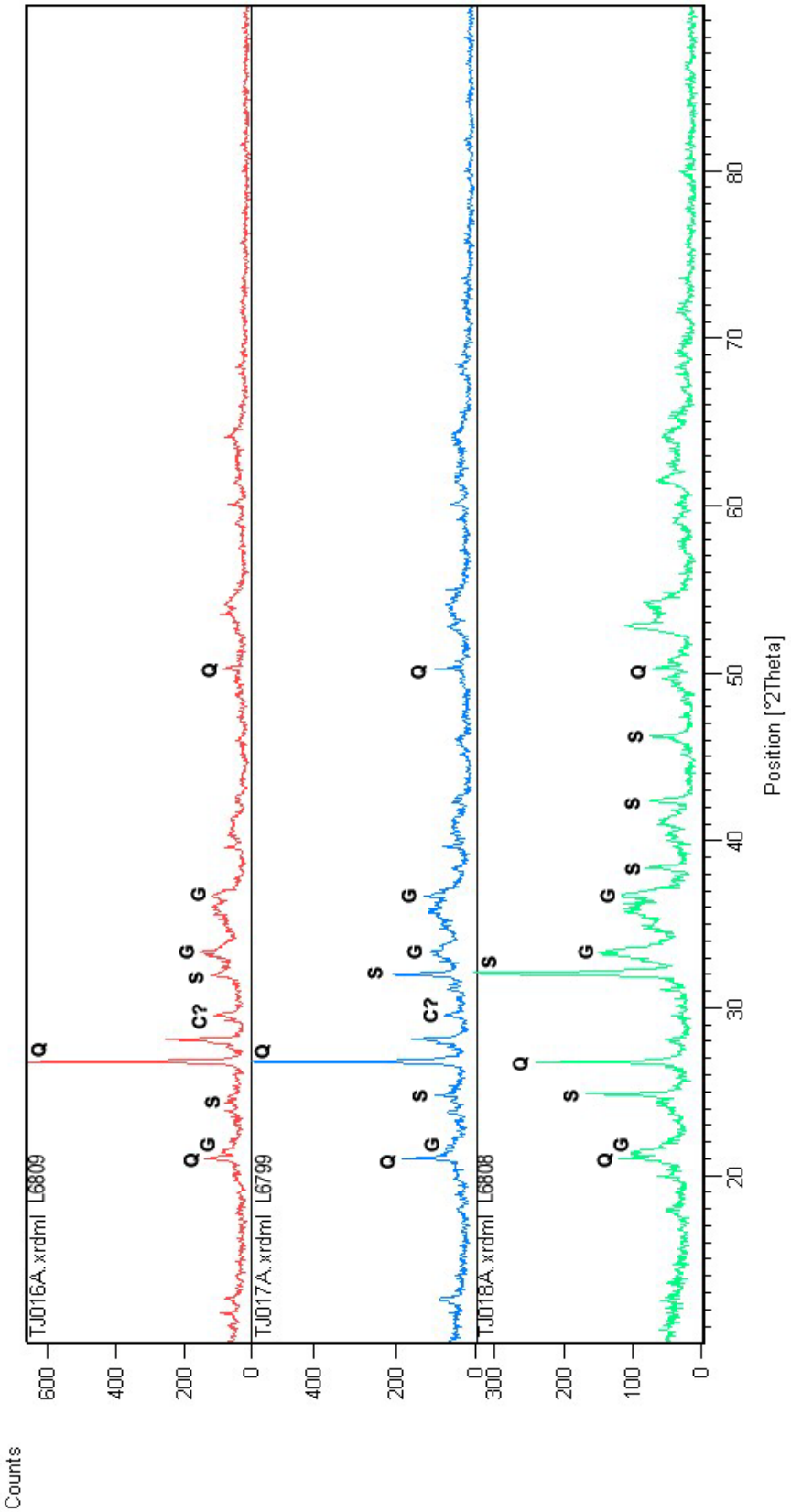
Counts
TJ016A.xrdml L6809
TJ017A.xrdml L6799
TJ018A.xrdml L6808
Q
G
S
C?
Position [°2Theta]

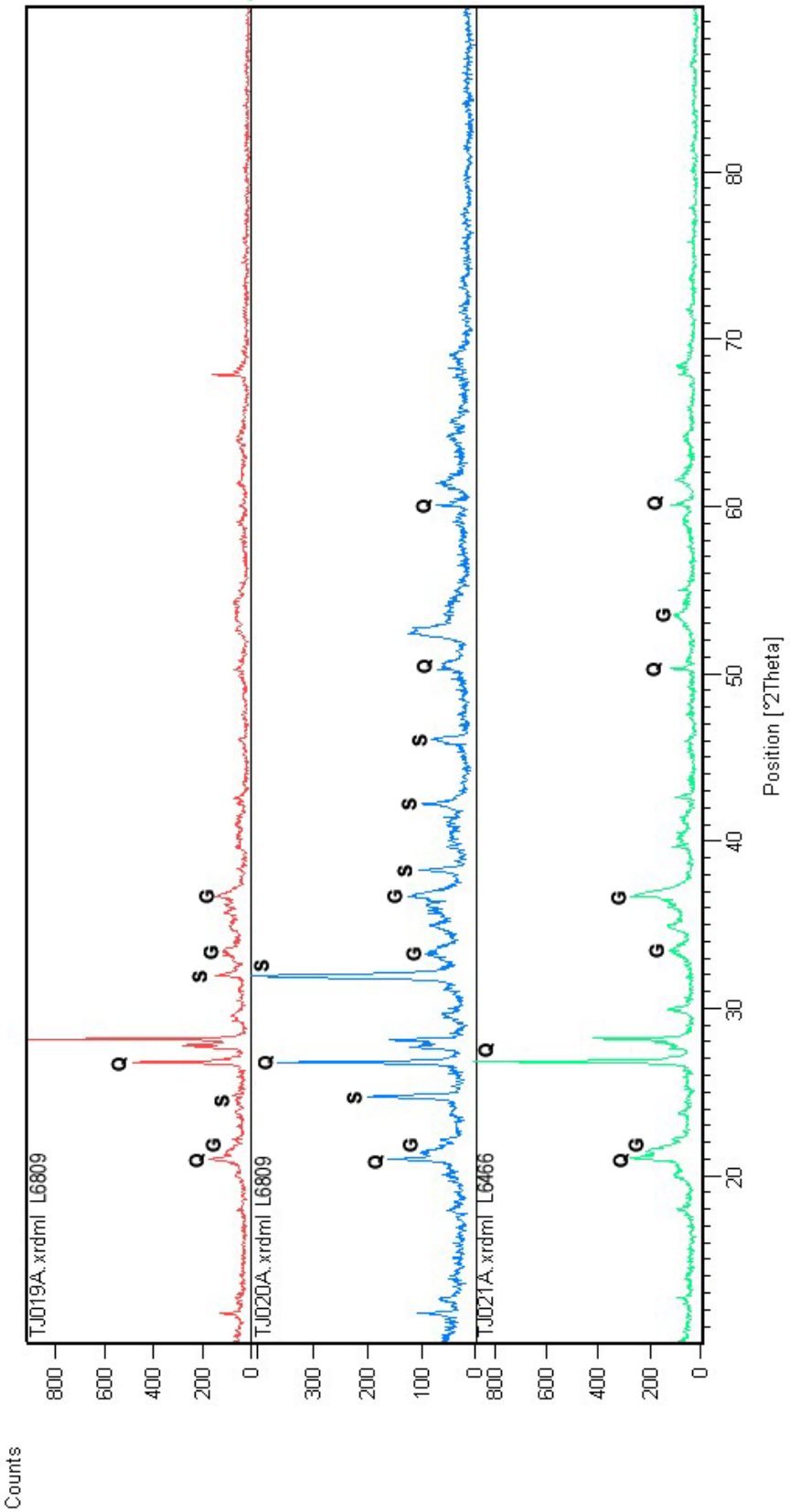
TJ019A.xrdml L6809
TJ020A.xrdml L6809
TJ021A.xrdml L6466
Counts
Position [°2Theta]

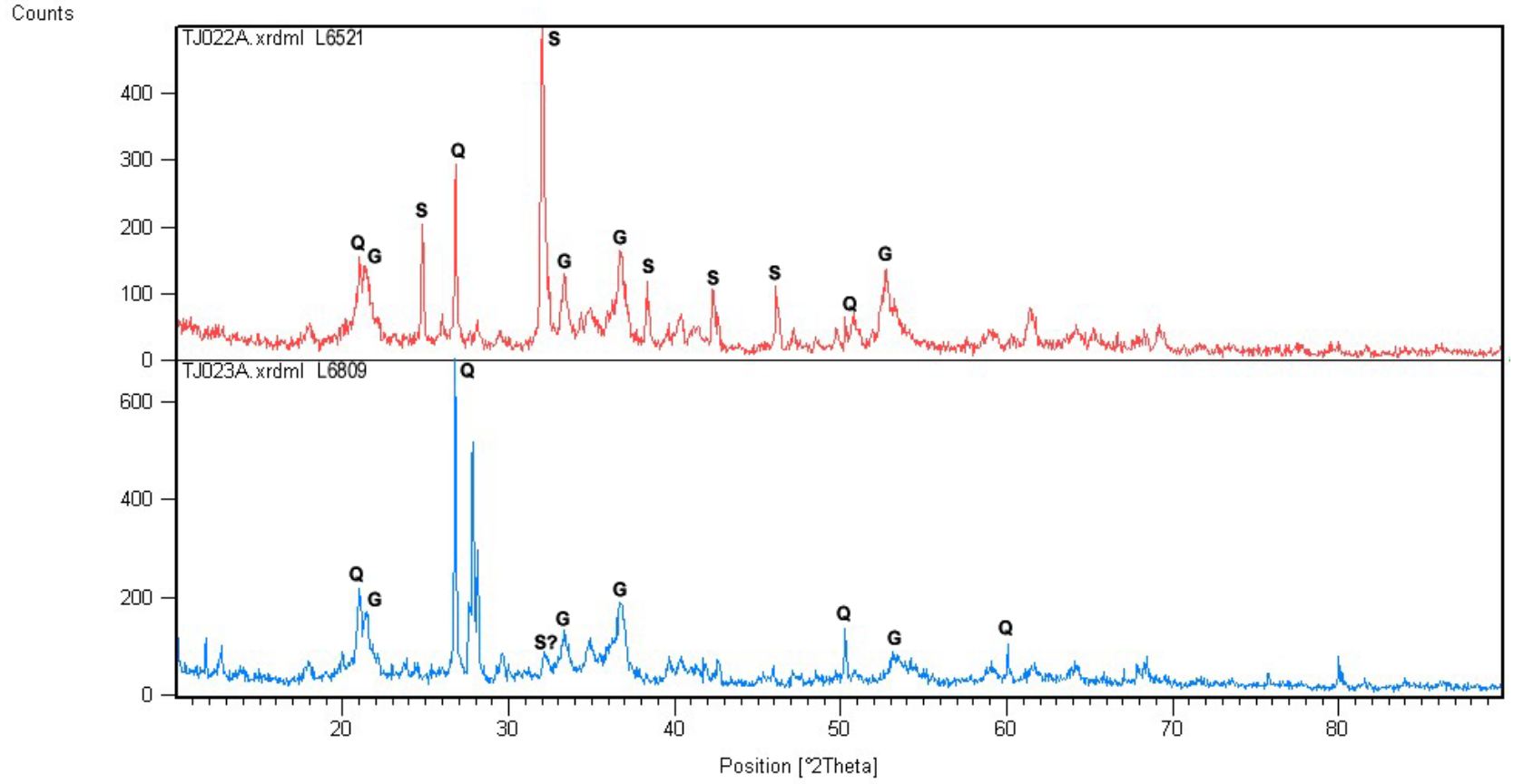
Counts
TJ022A.xrdml L6521
TJ023A.xrdml L6809
Q
G
S
S?
Position [°2Theta]

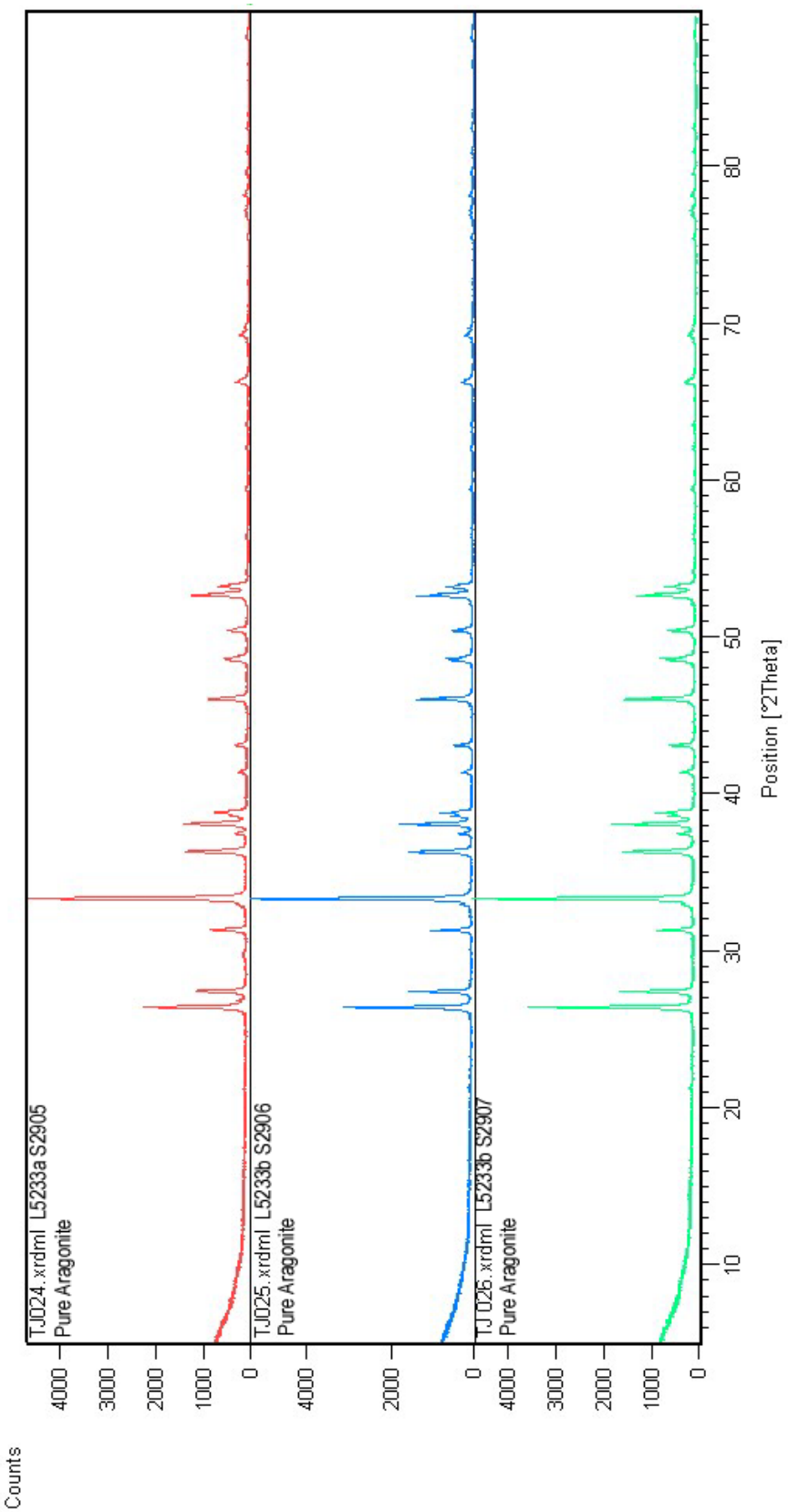
TJ024.xrdml L5233a S2905
Pure Aragonite
TJ025.xrdml L5233b S2906
Pure Aragonite
TJ026.xrdml L5233b S2907
Pure Aragonite
Counts
Position [°2Theta]
0
1000
2000
3000
4000
10
20
30
40
50
60
70
80

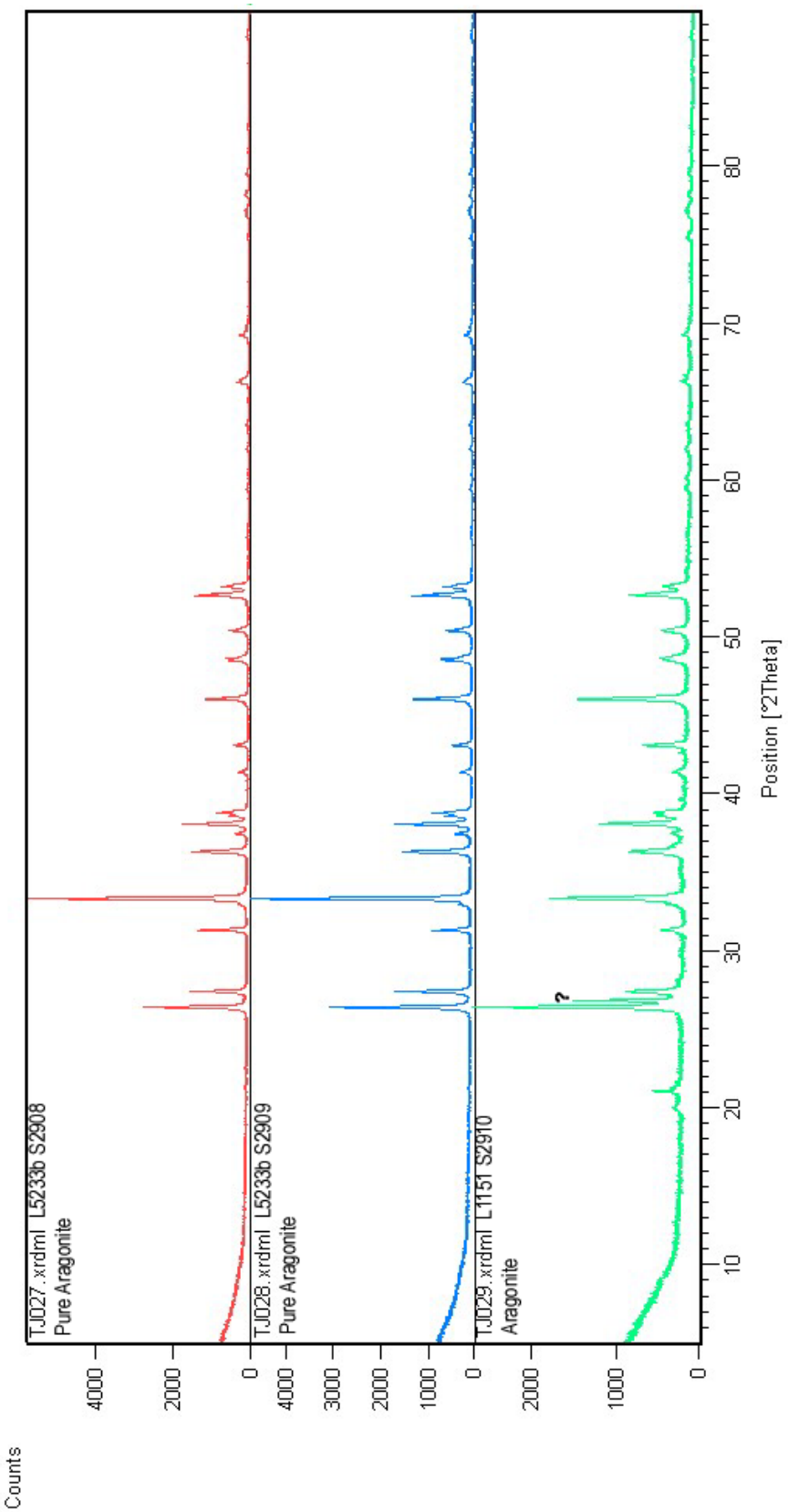
Counts
TJ027.xrdml L5233b S2908
Pure Aragonite
TJ028.xrdml L5233b S2909
Pure Aragonite
TJ029.xrdml L1151 S2910
Aragonite
?
Position [°2Theta]

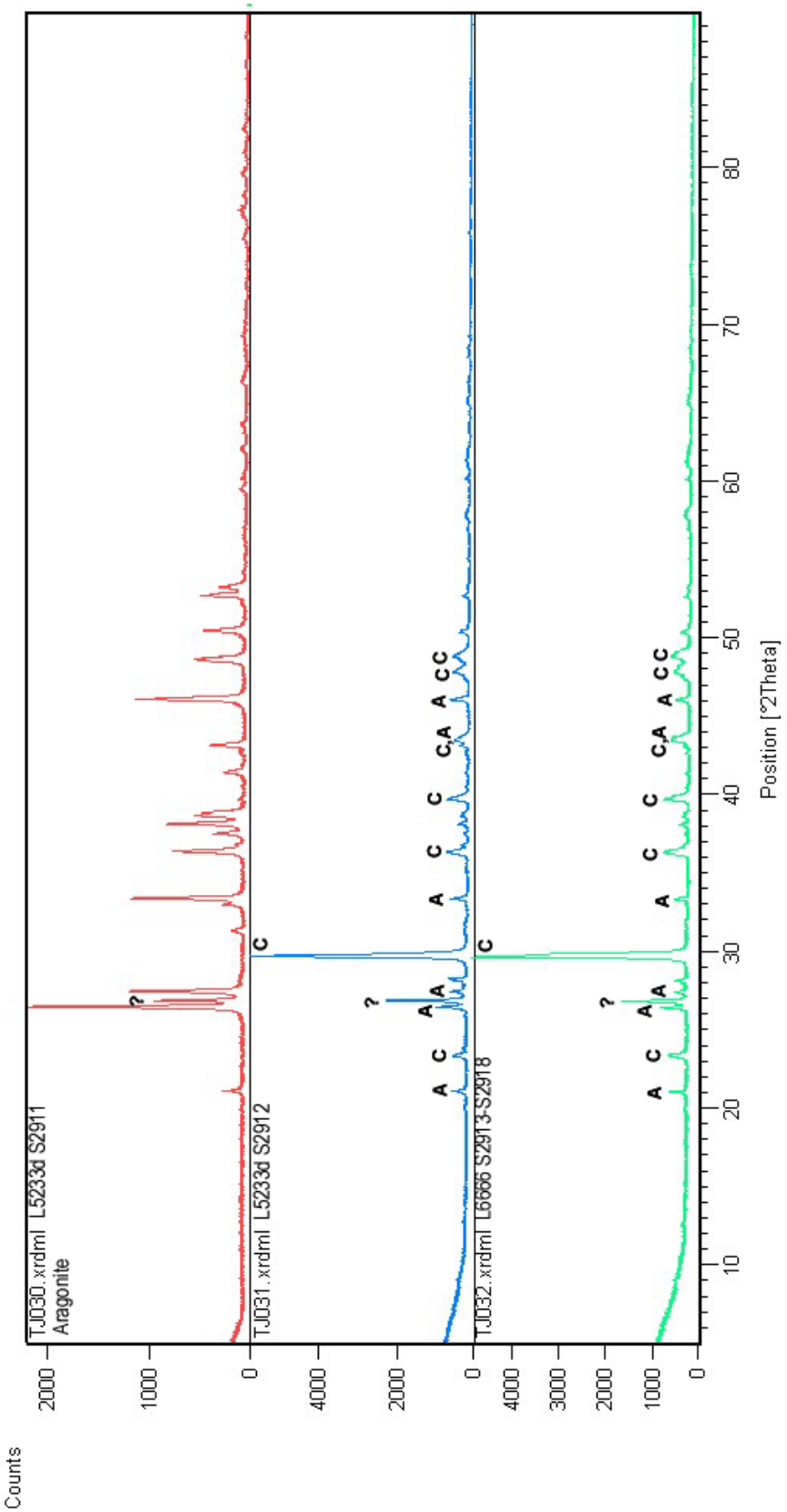
TJ030.xrdml L5233d S2911
Aragonite
TJ031.xrdml L5233d S2912
TJ032.xrdml L6666 S2913-S2918
Counts
Position [°2Theta]
2000
1000
0
4000
2000
0
4000
3000
2000
1000
0
10
20
30
40
50
60
70
80
?
A
C

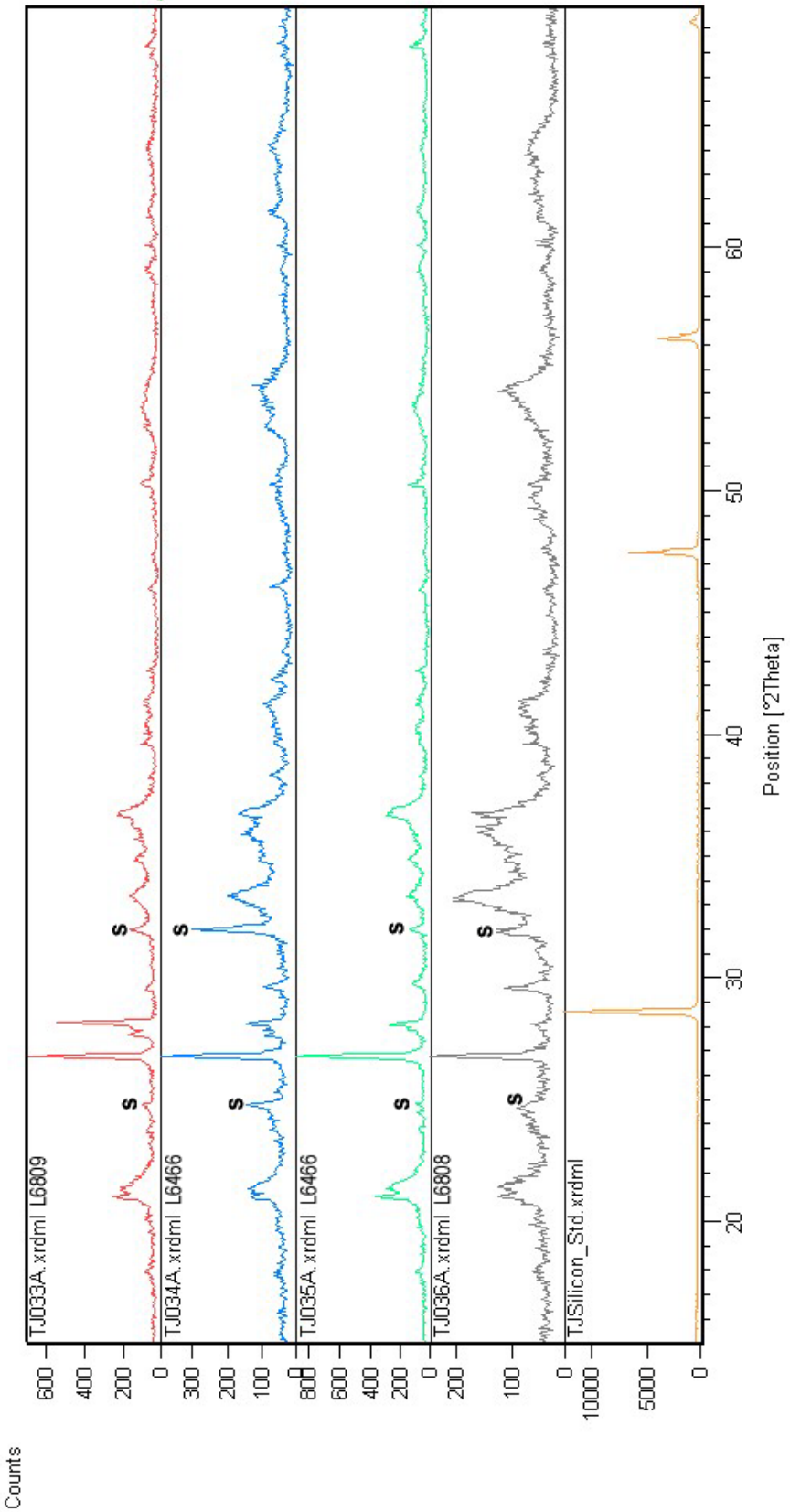
Counts
TJ033A.xrdml L6809
TJ034A.xrdml L6466
TJ035A.xrdml L6466
TJ036A.xrdml L6808
TJSilicon_Std.xrdml
S
Position [°2Theta]

Appendix B

Scanning Electron Microscopy EDS Results and Photographs

Locality L6466, S4704, *Proparreysia percorrugata* (Whitfield, 1903)
SEM Location 1, EDS Runs 1 – 3
Magnification x35

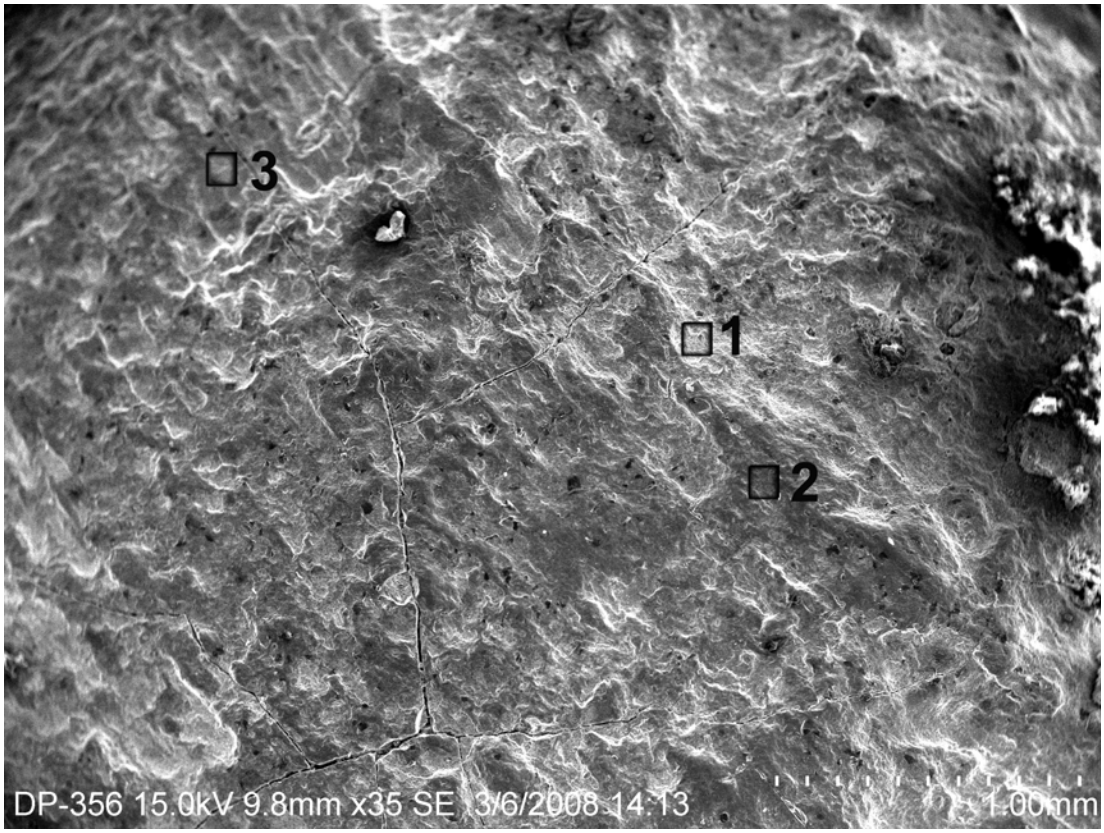

Locality L6466, S4704, *Proparreysia percorrugata*
SEM Location 1, EDS Run 1

Component	Conc.		
Mn	1.688	wt.%	
Si	12.006	wt.%	
Fe	26.035	wt.%	
C	5.036	wt.%	
Co	1.666	wt.%	
Ni	0.394	wt.%	
Mo	0.405	wt.%	
O	42.605	wt.%	
F	5.355	wt.%	
Mg	0.853	wt.%	
Al	2.875	wt.%	
Ca	1.083	wt.%	
	100.000	wt.%	Total

Elt.	Line	Intensity (c/s)	Error 2-sig	Atomic %	Atomic Ratio	Conc		
C	Ka	9.19	1.356	9.325	0.1575	5.036	wt.%	
O	Ka	260.34	7.215	59.224	1.0000	42.605	wt.%	
F	Ka	23.44	2.165	6.269	0.1059	5.355	wt.%	
Mg	Ka	12.27	1.566	0.781	0.0132	0.853	wt.%	
Al	Ka	47.91	3.095	2.370	0.0400	2.875	wt.%	
Si	Ka	220.59	6.641	9.507	0.1605	12.006	wt.%	
Ca	Ka	15.54	1.763	0.601	0.0101	1.083	wt.%	
Mn	Ka	12.00	1.549	0.683	0.0115	1.688	wt.%	
Fe	Ka	152.83	5.528	10.369	0.1751	26.035	wt.%	
Co	Ka	7.75	1.245	0.629	0.0106	1.666	wt.%	
Ni	Ka	1.46	0.541	0.149	0.0025	0.394	wt.%	
Mo	La	3.01	0.775	0.094	0.0016	0.405	wt.%	
				100.000		100.000	wt.%	Total

kV	15.0
Takeoff Angle	35.0°
Elapsed Livetime	20.0

Locality L6466, S4704, *Proparreysia percorrugata*
SEM Location 1, EDS Run 2

Component	Conc.		
Mn	0.824	wt.%	
Si	6.737	wt.%	
Fe	27.994	wt.%	
C	15.391	wt.%	
Co	1.221	wt.%	
Ni	0.514	wt.%	
Mo	0.102	wt.%	
O	38.517	wt.%	
F	4.640	wt.%	
Na	0.855	wt.%	
Mg	0.549	wt.%	
Al	0.851	wt.%	
Cl	0.462	wt.%	
Ca	1.301	wt.%	
Ru	0.042	wt.%	
	100.000	wt.%	Total

Elt.	Line	Intensity (c/s)	Error 2-sig	Atomic %	Atomic Ratio	Conc		
C	Ka	35.12	2.650	26.384	0.5323	15.391	wt.%	
O	Ka	209.26	6.469	49.566	1.0000	38.517	wt.%	
F	Ka	21.16	2.057	5.029	0.1015	4.640	wt.%	
Na	Ka	8.59	1.311	0.765	0.0154	0.855	wt.%	
Mg	Ka	7.95	1.261	0.465	0.0094	0.549	wt.%	
Al	Ka	14.35	1.694	0.649	0.0131	0.851	wt.%	
Si	Ka	127.89	5.057	4.939	0.0996	6.737	wt.%	
Cl	Ka	7.82	1.251	0.268	0.0054	0.462	wt.%	
Ca	Ka	19.32	1.965	0.668	0.0135	1.301	wt.%	
Mn	Ka	6.01	1.096	0.309	0.0062	0.824	wt.%	
Fe	Ka	167.59	5.789	10.321	0.2082	27.994	wt.%	
Co	Ka	5.79	1.077	0.427	0.0086	1.221	wt.%	
Ni	Ka	1.94	0.623	0.180	0.0036	0.514	wt.%	
Mo	La	0.81	0.403	0.022	0.0004	0.102	wt.%	
Ru	La	0.33	0.255	0.009	0.0002	0.042	wt.%	
				100.000		100.000	wt.%	Total

kV	15.0
Takeoff Angle	35.0°
Elapsed Livetime	20.0

Locality L6466, S4704, *Proparreysia percorrugata*
SEM Location 1, EDS Run 3

Component	Conc.		
Mn	0.498	wt.%	
Si	5.853	wt.%	
Fe	31.479	wt.%	
C	6.076	wt.%	
Co	1.996	wt.%	
Ni	0.057	wt.%	
Mo	0.397	wt.%	
O	41.305	wt.%	
F	6.280	wt.%	
Al	0.838	wt.%	
Ca	1.410	wt.%	
Rb	3.810	wt.%	
	100.000	wt.%	Total

Elt.	Line	Intensity (c/s)	Error 2-sig	Atomic %	Atomic Ratio	Conc		
C	Ka	13.52	1.644	11.633	0.1960	6.076	wt.%	
O	Ka	237.64	6.893	59.361	1.0000	41.305	wt.%	
F	Ka	27.63	2.351	7.600	0.1280	6.280	wt.%	
Al	Ka	13.03	1.614	0.714	0.0120	0.838	wt.%	
Si	Ka	102.99	4.538	4.792	0.0807	5.853	wt.%	
Ca	Ka	19.56	1.977	0.809	0.0136	1.410	wt.%	
Mn	Ka	3.43	0.828	0.208	0.0035	0.498	wt.%	
Fe	Ka	177.97	5.965	12.961	0.2183	31.479	wt.%	
Co	Ka	8.96	1.339	0.779	0.0131	1.996	wt.%	
Ni	Ka	0.20	0.202	0.022	0.0004	0.057	wt.%	
Rb	La	30.14	2.455	1.025	0.0173	3.810	wt.%	
Mo	La	2.86	0.756	0.095	0.0016	0.397	wt.%	
				100.000		100.000	wt.%	Total

kV	15.0
Takeoff Angle	35.0°
Elapsed Livetime	20.0

Locality L6466, S4704, *Proparreysia percorrugata*
SEM Location 2, EDS Runs 1 – 2
Magnification x55

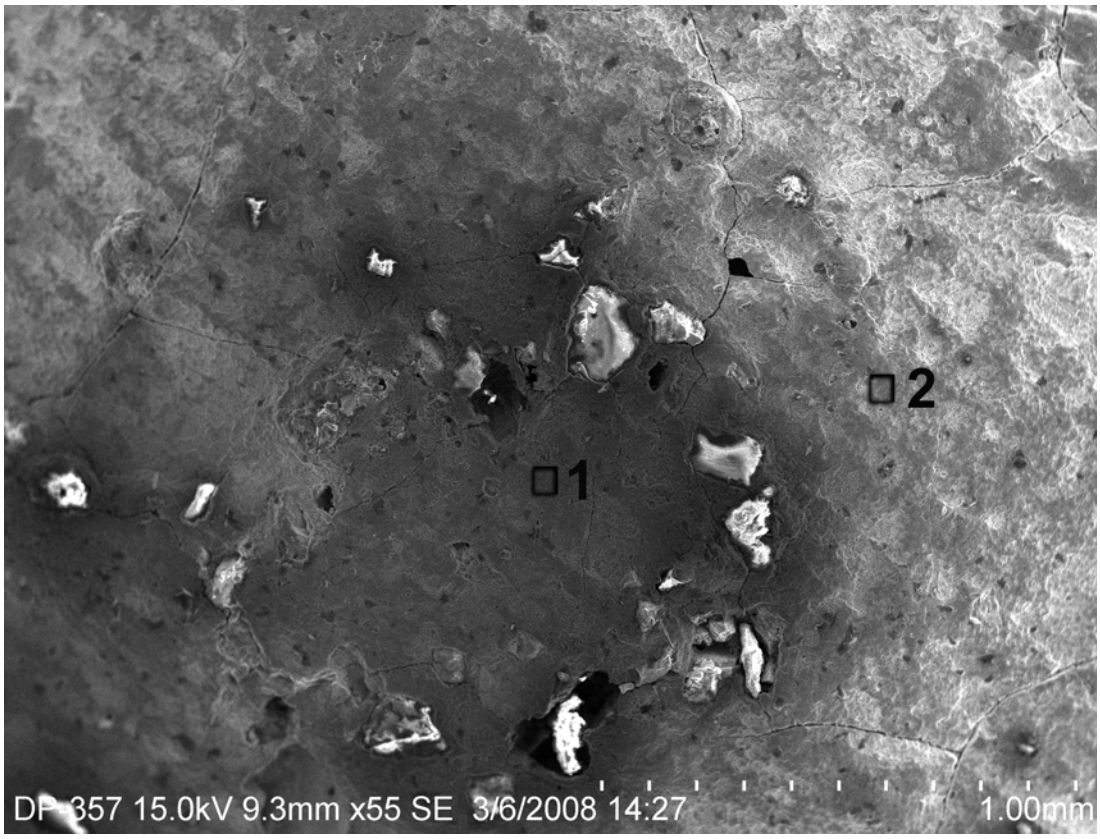

Locality L6466, S4704, *Proparreysia percorrugata*
SEM Location 2, EDS Run 1

Component	Conc.		
Mn	3.534	wt.%	
Si	5.801	wt.%	
Fe	35.354	wt.%	
C	6.502	wt.%	
Co	1.975	wt.%	
Ni	0.448	wt.%	
Mo	0.252	wt.%	
O	36.877	wt.%	
F	5.375	wt.%	
Na	0.491	wt.%	
Mg	1.202	wt.%	
Al	1.048	wt.%	
Ca	1.140	wt.%	
	100.000	wt.%	Total

Elt.	Line	Intensity (c/s)	Error 2-sig	Atomic %	Atomic Ratio	Conc		
C	Ka	14.02	1.674	12.844	0.2349	6.502	wt.%	
O	Ka	233.18	6.828	54.683	1.0000	36.877	wt.%	
F	Ka	25.62	2.263	6.713	0.1228	5.375	wt.%	
Na	Ka	4.52	0.950	0.507	0.0093	0.491	wt.%	
Mg	Ka	16.15	1.797	1.173	0.0215	1.202	wt.%	
Al	Ka	16.53	1.818	0.921	0.0169	1.048	wt.%	
Si	Ka	104.23	4.565	4.901	0.0896	5.801	wt.%	
Ca	Ka	16.88	1.837	0.675	0.0123	1.140	wt.%	
Mn	Ka	25.82	2.272	1.526	0.0279	3.534	wt.%	
Fe	Ka	211.56	6.504	15.019	0.2747	35.354	wt.%	
Co	Ka	9.35	1.367	0.795	0.0145	1.975	wt.%	
Ni	Ka	1.69	0.581	0.181	0.0033	0.448	wt.%	
Mo	La	1.96	0.626	0.062	0.0011	0.252	wt.%	
				100.000		100.000	wt.%	Total

kV	15.0
Takeoff Angle	35.0°
Elapsed Livetime	20.0

Locality L6466, S4704, *Proparreysia percorrugata*
SEM Location 2, EDS Run 2

Component	Conc.	
Mn	3.444	wt.%
Si	6.520	wt.%
Fe	42.912	wt.%
C	11.499	wt.%
Co	2.130	wt.%
Ni	0.189	wt.%
Mo	0.255	wt.%
O	26.131	wt.%
F	2.815	wt.%
Na	0.627	wt.%
Mg	0.608	wt.%
Al	0.652	wt.%
K	0.853	wt.%
Ca	1.069	wt.%
Np	0.164	wt.%
Pu	0.133	wt.%
	100.000	wt.% Total

Elt.	Line	Intensity (c/s)	Error 2-sig	Atomic %	Atomic Ratio	Conc	
C	Ka	17.23	1.856	24.114	0.5862	11.499	wt.%
O	Ka	102.03	4.517	41.137	1.0000	26.131	wt.%
F	Ka	10.83	1.472	3.733	0.0907	2.815	wt.%
Na	Ka	4.06	0.902	0.686	0.0167	0.627	wt.%
Mg	Ka	5.76	1.073	0.631	0.0153	0.608	wt.%
Al	Ka	7.28	1.207	0.608	0.0148	0.652	wt.%
Si	Ka	83.29	4.081	5.847	0.1421	6.520	wt.%
K	Ka	9.44	1.374	0.550	0.0134	0.853	wt.%
Ca	Ka	11.33	1.505	0.672	0.0163	1.069	wt.%
Mn	Ka	18.11	1.903	1.579	0.0384	3.444	wt.%
Fe	Ka	184.21	6.069	19.354	0.4705	42.912	wt.%
Co	Ka	7.25	1.204	0.910	0.0221	2.130	wt.%
Ni	Ka	0.51	0.319	0.081	0.0020	0.189	wt.%
Mo	La	1.42	0.534	0.067	0.0016	0.255	wt.%
Np	Ma	0.77	0.392	0.017	0.0004	0.164	wt.%
Pu	Ma	0.63	0.356	0.014	0.0003	0.133	wt.%
				100.000		100.000	wt.% Tc

kV	15.0
Takeoff Angle	35.0°
Elapsed Livetime	20.0

Locality L6521, S4712, *Sphaerium* sp. (Scopoli, 1777)
SEM Location 1 on umbo, EDS Runs 1 – 3
Magnification x35

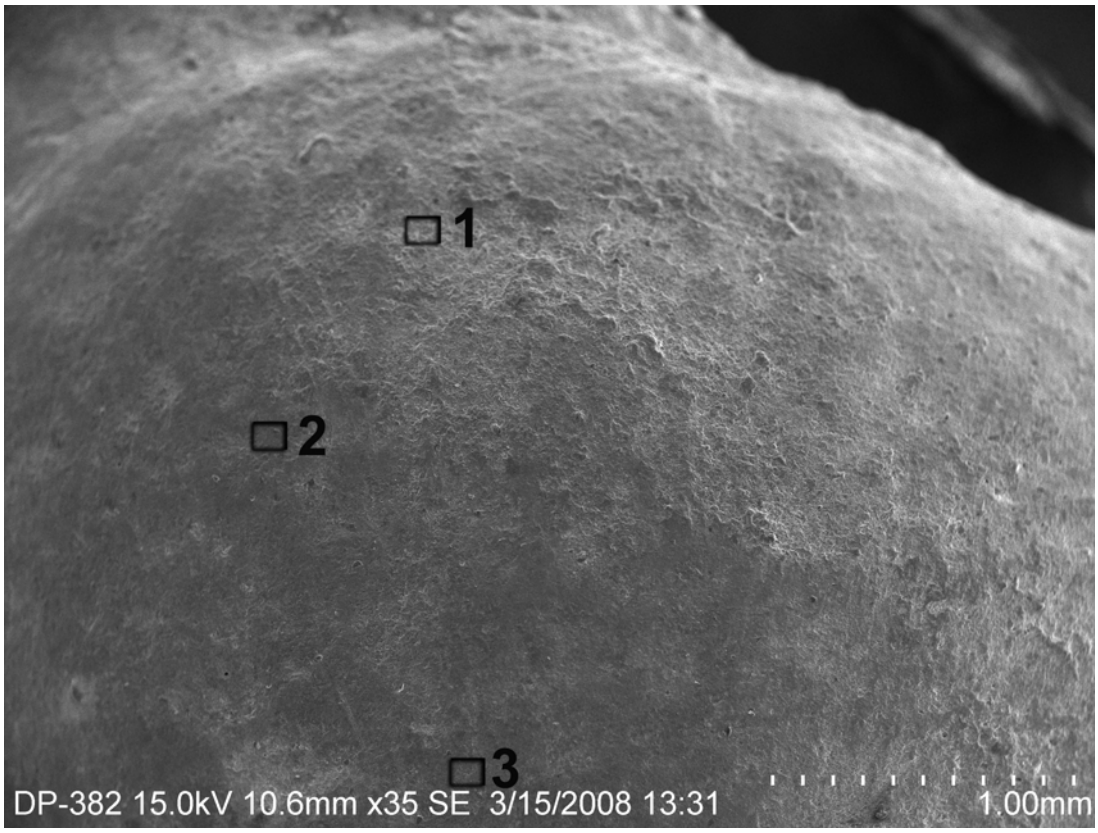

Locality L6521, S4712, *Sphaerium* sp.
SEM Location 1 on umbo, EDS run 1

Component	Conc.		
Mn	0.712	wt.%	
Si	22.130	wt.%	
Fe	8.054	wt.%	
Cr	0.037	wt.%	
C	7.720	wt.%	
V	0.090	wt.%	
Co	0.726	wt.%	
Ni	0.387	wt.%	
O	39.131	wt.%	
F	0.000	wt.%	
Na	0.833	wt.%	
Mg	0.941	wt.%	
Al	9.823	wt.%	
K	1.774	wt.%	
Rb	7.641	wt.%	
	100.000	wt.%	Total

Elt.	Line	Intensity (c/s)	Error 2-sig	Atomic %	Atomic Ratio	Conc		
C	Ka	9.84	1.403	13.886	0.2628	7.720	wt.%	
O	Ka	158.08	5.623	52.837	1.0000	39.131	wt.%	
F	Ka	0.00	0.000	0.000	0.0000	0.000	wt.%	
Na	Ka	9.88	1.406	0.783	0.0148	0.833	wt.%	
Mg	Ka	15.11	1.738	0.836	0.0158	0.941	wt.%	
Al	Ka	173.20	5.885	7.865	0.1489	9.823	wt.%	
Si	Ka	384.68	8.771	17.022	0.3222	22.130	wt.%	
K	Ka	22.66	2.128	0.980	0.0186	1.774	wt.%	
V	Ka	0.76	0.389	0.038	0.0007	0.090	wt.%	
Cr	Ka	0.28	0.237	0.015	0.0003	0.037	wt.%	
Mn	Ka	4.40	0.938	0.280	0.0053	0.712	wt.%	
Fe	Ka	41.91	2.895	3.116	0.0590	8.054	wt.%	
Co	Ka	3.00	0.775	0.266	0.0050	0.726	wt.%	
Ni	Ka	1.30	0.509	0.142	0.0027	0.387	wt.%	
Rb	La	59.52	3.450	1.931	0.0366	7.641	wt.%	
				100.000		100.000	wt.%	Total

kV	15.0
Takeoff Angle	35.0°
Elapsed Livetime	20.0

Locality L6521, S4712, *Sphaerium* sp.
SEM Location 1 on umbo, EDS run 2

Component	Conc.		
Mn	2.549	wt.%	
Si	11.411	wt.%	
Fe	14.312	wt.%	
Cr	0.092	wt.%	
C	11.425	wt.%	
Co	0.871	wt.%	
Ni	0.304	wt.%	
O	42.709	wt.%	
F	2.961	wt.%	
Na	0.993	wt.%	
Mg	1.111	wt.%	
Al	5.637	wt.%	
K	0.998	wt.%	
Rb	4.628	wt.%	
	100.000	wt.%	Total

Elt.	Line	Intensity (c/s)	Error 2-sig	Atomic %	Atomic Ratio	Conc		
C	Ka	21.45	2.071	19.474	0.3563	11.425	wt.%	
O	Ka	212.33	6.516	54.649	1.0000	42.709	wt.%	
F	Ka	11.30	1.503	3.190	0.0584	2.961	wt.%	
Na	Ka	10.93	1.478	0.884	0.0162	0.993	wt.%	
Mg	Ka	17.08	1.848	0.936	0.0171	1.111	wt.%	
Al	Ka	97.73	4.421	4.277	0.0783	5.637	wt.%	
Si	Ka	208.62	6.459	8.317	0.1522	11.411	wt.%	
K	Ka	14.20	1.685	0.523	0.0096	0.998	wt.%	
Cr	Ka	0.78	0.395	0.036	0.0007	0.092	wt.%	
Mn	Ka	17.17	1.853	0.950	0.0174	2.549	wt.%	
Fe	Ka	80.57	4.014	5.247	0.0960	14.312	wt.%	
Co	Ka	3.88	0.881	0.302	0.0055	0.871	wt.%	
Ni	Ka	1.09	0.468	0.106	0.0019	0.304	wt.%	
Rb	La	37.90	2.753	1.109	0.0203	4.628	wt.%	
				100.000		100.000	wt.%	Total

kV	15.0
Takeoff Angle	35.0°
Elapsed Livetime	20.0

Locality L6521, S4712, *Sphaerium* sp.
SEM Location 1 on umbo, EDS run 3

Component	Conc.		
Mn	1.270	wt.%	
Si	16.483	wt.%	
Fe	19.405	wt.%	
Cr	0.181	wt.%	
C	11.362	wt.%	
Co	0.808	wt.%	
Ni	0.295	wt.%	
O	39.858	wt.%	
F	0.000	wt.%	
Na	0.620	wt.%	
Mg	1.094	wt.%	
Al	7.161	wt.%	
K	1.462	wt.%	
	100.000	wt.%	Total

Elt.	Line	Intensity (c/s)	Error 2-sig	Atomic %	Atomic Ratio	Conc		
C	Ka	13.87	1.665	19.743	0.3797	11.362	wt.%	
O	Ka	156.78	5.599	51.990	1.0000	39.858	wt.%	
F	Ka	0.00	0.000	0.000	0.0000	0.000	wt.%	
Na	Ka	5.44	1.043	0.563	0.0108	0.620	wt.%	
Mg	Ka	13.50	1.643	0.940	0.0181	1.094	wt.%	
Al	Ka	99.85	4.468	5.539	0.1065	7.161	wt.%	
Si	Ka	238.59	6.907	12.248	0.2356	16.483	wt.%	
K	Ka	16.77	1.831	0.781	0.0150	1.462	wt.%	
Cr	Ka	1.27	0.504	0.073	0.0014	0.181	wt.%	
Mn	Ka	6.89	1.174	0.482	0.0093	1.270	wt.%	
Fe	Ka	87.72	4.188	7.252	0.1395	19.405	wt.%	
Co	Ka	2.90	0.761	0.286	0.0055	0.808	wt.%	
Ni	Ka	0.85	0.412	0.105	0.0020	0.295	wt.%	
				100.000		100.000	wt.%	Total

kV	15.0
Takeoff Angle	35.0°
Elapsed Livetime	20.0

Locality L6521, S4712, *Sphaerium* sp.
SEM Location 2 on margin, EDS Runs 1 – 3
Magnification x35

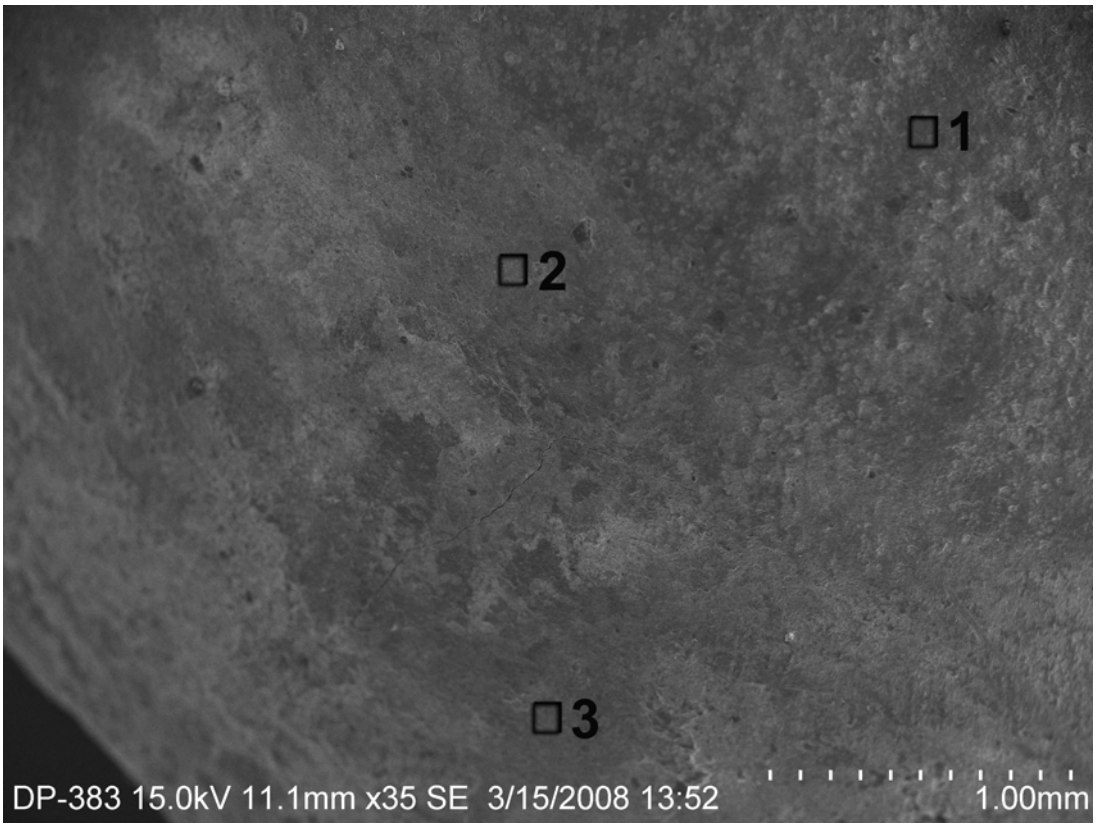

Locality L6521, S4712, *Sphaerium* sp.
SEM Location 2 on margin, EDS run 1

Component	Conc.		
Mn	2.636	wt.%	
Si	10.930	wt.%	
Fe	26.551	wt.%	
Cr	0.232	wt.%	
C	7.159	wt.%	
Co	1.730	wt.%	
Ni	0.265	wt.%	
Mo	0.049	wt.%	
O	34.492	wt.%	
F	0.000	wt.%	
Na	0.732	wt.%	
Mg	0.952	wt.%	
Al	5.767	wt.%	
S	0.251	wt.%	
Cl	0.463	wt.%	
K	1.820	wt.%	
Rb	5.742	wt.%	
Ru	0.229	wt.%	
	100.000	wt.%	Total

Elt.	Line	Intensity (c/s)	Error 2-sig	Atomic %	Atomic Ratio	Conc		
C	Ka	14.64	1.711	14.450	0.2765	7.159	wt.%	
O	Ka	199.59	6.317	52.263	1.0000	34.492	wt.%	
F	Ka	0.00	0.000	0.000	0.0000	0.000	wt.%	
Na	Ka	8.72	1.320	0.771	0.0148	0.732	wt.%	
Mg	Ka	16.09	1.793	0.950	0.0182	0.952	wt.%	
Al	Ka	111.52	4.722	5.182	0.0992	5.767	wt.%	
Si	Ka	225.88	6.720	9.434	0.1805	10.930	wt.%	
S	Ka	4.53	0.952	0.190	0.0036	0.251	wt.%	
Cl	Ka	8.22	1.282	0.316	0.0061	0.463	wt.%	
K	Ka	30.27	2.460	1.128	0.0216	1.820	wt.%	
Cr	Ka	2.41	0.694	0.108	0.0021	0.232	wt.%	
Mn	Ka	21.16	2.057	1.163	0.0223	2.636	wt.%	
Fe	Ka	177.14	5.951	11.526	0.2205	26.551	wt.%	
Co	Ka	9.16	1.353	0.712	0.0136	1.730	wt.%	
Ni	Ka	1.12	0.474	0.110	0.0021	0.265	wt.%	
Rb	La	53.45	3.269	1.629	0.0312	5.742	wt.%	
Mo	La	0.40	0.282	0.012	0.0002	0.049	wt.%	
Ru	La	1.82	0.604	0.055	0.0011	0.229	wt.%	
				100.000		100.000	wt.%	Tc

kV	15.0
Takeoff Angle	35.0°

Locality L6521, S4712, *Sphaerium* sp.
SEM Location 2 on margin, EDS run 2

Component	Conc.		
Mn	3.300	wt.%	
Si	6.942	wt.%	
Fe	43.283	wt.%	
Cr	0.188	wt.%	
C	4.946	wt.%	
Co	2.975	wt.%	
Ni	0.242	wt.%	
Mo	0.413	wt.%	
O	27.040	wt.%	
F	2.802	wt.%	
Na	0.332	wt.%	
Mg	0.786	wt.%	
Al	3.691	wt.%	
K	0.736	wt.%	
Rb	2.324	wt.%	
	100.000	wt.%	Total

Elt.	Line	Intensity (c/s)	Error 2-sig	Atomic %	Atomic Ratio	Conc		
C	Ka	8.75	1.323	11.364	0.2437	4.946	wt.%	
O	Ka	148.03	5.440	46.638	1.0000	27.040	wt.%	
F	Ka	14.26	1.689	4.070	0.0873	2.802	wt.%	
Na	Ka	2.77	0.744	0.398	0.0085	0.332	wt.%	
Mg	Ka	9.59	1.385	0.893	0.0191	0.786	wt.%	
Al	Ka	52.98	3.255	3.775	0.0809	3.691	wt.%	
Si	Ka	111.18	4.715	6.821	0.1463	6.942	wt.%	
K	Ka	10.29	1.434	0.520	0.0111	0.736	wt.%	
Cr	Ka	1.77	0.595	0.100	0.0021	0.188	wt.%	
Mn	Ka	22.36	2.114	1.658	0.0355	3.300	wt.%	
Fe	Ka	239.64	6.922	21.388	0.4586	43.283	wt.%	
Co	Ka	13.06	1.616	1.393	0.0299	2.975	wt.%	
Ni	Ka	0.84	0.410	0.114	0.0024	0.242	wt.%	
Rb	La	16.73	1.829	0.750	0.0161	2.324	wt.%	
Mo	La	2.84	0.753	0.119	0.0025	0.413	wt.%	
				100.000		100.000	wt.%	Total

kV	15.0
Takeoff Angle	35.0°
Elapsed Livetime	20.0

Locality L6521, S4712, *Sphaerium* sp.
SEM Location 2 on margin, EDS run 3

Component	Conc.		
Mn	23.757	wt.%	
Si	7.255	wt.%	
Fe	27.022	wt.%	
Cr	0.168	wt.%	
C	6.491	wt.%	
Co	0.760	wt.%	
Ni	0.219	wt.%	
Mo	0.417	wt.%	
O	23.310	wt.%	
F	3.672	wt.%	
Na	0.920	wt.%	
Mg	0.571	wt.%	
Al	3.633	wt.%	
K	0.971	wt.%	
Ca	0.832	wt.%	
	100.000	wt.%	Total

Elt.	Line	Intensity (c/s)	Error 2-sig	Atomic %	Atomic Ratio	Conc		
C	Ka	10.20	1.428	14.874	0.3709	6.491	wt.%	
O	Ka	110.58	4.703	40.100	1.0000	23.310	wt.%	
F	Ka	11.52	1.518	5.320	0.1327	3.672	wt.%	
Na	Ka	6.91	1.176	1.101	0.0275	0.920	wt.%	
Mg	Ka	6.23	1.116	0.647	0.0161	0.571	wt.%	
Al	Ka	46.68	3.055	3.706	0.0924	3.633	wt.%	
Si	Ka	103.50	4.549	7.110	0.1773	7.255	wt.%	
K	Ka	12.16	1.559	0.684	0.0170	0.971	wt.%	
Ca	Ka	10.00	1.414	0.571	0.0142	0.832	wt.%	
Cr	Ka	1.26	0.502	0.089	0.0022	0.168	wt.%	
Mn	Ka	138.94	5.271	11.902	0.2968	23.757	wt.%	
Fe	Ka	132.26	5.143	13.318	0.3321	27.022	wt.%	
Co	Ka	2.90	0.761	0.355	0.0089	0.760	wt.%	
Ni	Ka	0.67	0.366	0.103	0.0026	0.219	wt.%	
Mo	La	2.63	0.725	0.120	0.0030	0.417	wt.%	
				100.000		100.000	wt.%	Total

kV	15.0
Takeoff Angle	35.0°
Elapsed Livetime	20.0

Locality L6809, *Campeloma* sp. Nodule
SEM Location 1, tiny, distorted gastropod, S4726, EDS Runs 1 – 2
Magnification x400

Locality L6809, *Campeloma* sp. Nodule
SEM Location 1, tiny, distorted gastropod, S4726, EDS Run 1

Component	Conc.		
Mn	0.137	wt.%	
Si	46.643	wt.%	
Fe	0.901	wt.%	
Cr	0.052	wt.%	
C	2.053	wt.%	
Co	0.129	wt.%	
Ni	0.233	wt.%	
Mo	0.156	wt.%	
B	0.000	wt.%	
O	47.933	wt.%	
Al	0.700	wt.%	
P	0.271	wt.%	
Ca	0.791	wt.%	
Zr	0.000	wt.%	
	100.000	wt.%	Total

Elt.	Line	Intensity (c/s)	Error 2-sig	Atomic %	Atomic Ratio	Conc		
B	Ka	0.00	0.000	0.000	0.0000	0.000	wt.%	
C	Ka	1.74	0.589	3.482	0.0571	2.053	wt.%	
O	Ka	214.56	6.550	61.024	1.0000	47.933	wt.%	
Al	Ka	13.97	1.671	0.529	0.0087	0.700	wt.%	
Si	Ka	963.03	13.876	33.827	0.5543	46.643	wt.%	
P	Ka	3.58	0.846	0.178	0.0029	0.271	wt.%	
Ca	Ka	9.91	1.407	0.402	0.0066	0.791	wt.%	
Cr	Ka	0.40	0.282	0.021	0.0003	0.052	wt.%	
Mn	Ka	0.86	0.415	0.051	0.0008	0.137	wt.%	
Fe	Ka	4.80	0.980	0.328	0.0054	0.901	wt.%	
Co	Ka	0.55	0.331	0.045	0.0007	0.129	wt.%	
Ni	Ka	0.80	0.401	0.081	0.0013	0.233	wt.%	
Zr	La	0.00	0.000	0.000	0.0000	0.000	wt.%	
Mo	La	0.94	0.433	0.033	0.0005	0.156	wt.%	
				100.000		100.000	wt.%	Total

kV	15.0
Takeoff Angle	35.0°
Elapsed Livetime	20.0

Locality L6809, *Campeloma* sp. Nodule
SEM Location 1, tiny, distorted gastropod, S4726, EDS Run 2

Component	Conc.		
Mn	2.425	wt.%	
Si	0.973	wt.%	
Fe	41.735	wt.%	
Cr	0.147	wt.%	
C	10.317	wt.%	
Co	2.137	wt.%	
Ni	0.268	wt.%	
Mo	0.137	wt.%	
O	35.812	wt.%	
F	0.000	wt.%	
Mg	0.320	wt.%	
Al	0.527	wt.%	
P	0.679	wt.%	
Ca	3.981	wt.%	
Zr	0.000	wt.%	
I	0.544	wt.%	
	100.000	wt.%	Total

Elt.	Line	Intensity (c/s)	Error 2-sig	Atomic %	Atomic Ratio	Conc		
C	Ka	18.35	1.916	20.814	0.3837	10.317	wt.%	
O	Ka	141.13	5.312	54.241	1.0000	35.812	wt.%	
F	Ka	0.00	0.000	0.000	0.0000	0.000	wt.%	
Mg	Ka	2.97	0.771	0.319	0.0059	0.320	wt.%	
Al	Ka	5.81	1.078	0.473	0.0087	0.527	wt.%	
Si	Ka	12.35	1.572	0.840	0.0155	0.973	wt.%	
P	Ka	8.42	1.297	0.532	0.0098	0.679	wt.%	
Ca	Ka	42.46	2.914	2.407	0.0444	3.981	wt.%	
Cr	Ka	1.07	0.463	0.068	0.0013	0.147	wt.%	
Mn	Ka	12.65	1.590	1.070	0.0197	2.425	wt.%	
Fe	Ka	177.81	5.963	18.110	0.3339	41.735	wt.%	
Co	Ka	7.22	1.202	0.879	0.0162	2.137	wt.%	
Ni	Ka	0.72	0.378	0.111	0.0020	0.268	wt.%	
Zr	La	0.00	0.000	0.000	0.0000	0.000	wt.%	
Mo	La	0.79	0.398	0.035	0.0006	0.137	wt.%	
I	La	2.54	0.712	0.104	0.0019	0.544	wt.%	
				100.000		100.000	wt.%	Tc

kV	15.0
Takeoff Angle	35.0°
Elapsed Livetime	20.0

Locality L6809, *Campeloma* sp. Nodule
SEM Location 2, matrix near *Campeloma* sp., S4725, EDS Runs 1 – 2
Magnification x65

Locality L6809, *Campeloma* sp. Nodule
SEM Location 2, matrix near *Campeloma* sp., S4725, EDS Run 1

Component	Conc.		
Mn	2.069	wt.%	
Si	4.274	wt.%	
Fe	54.713	wt.%	
Cr	0.114	wt.%	
C	4.570	wt.%	
Co	4.395	wt.%	
Ni	0.647	wt.%	
O	22.188	wt.%	
F	2.294	wt.%	
Mg	0.572	wt.%	
Al	2.086	wt.%	
S	0.342	wt.%	
Ca	1.736	wt.%	
	100.000	wt.%	Total

Elt.	Line	Intensity (c/s)	Error 2-sig	Atomic %	Atomic Ratio	Conc		
C	Ka	3.97	0.891	11.530	0.2744	4.570	wt.%	
O	Ka	59.03	3.436	42.021	1.0000	22.188	wt.%	
F	Ka	6.34	1.126	3.659	0.0871	2.294	wt.%	
Mg	Ka	3.11	0.788	0.713	0.0170	0.572	wt.%	
Al	Ka	13.55	1.646	2.343	0.0558	2.086	wt.%	
Si	Ka	31.80	2.522	4.612	0.1097	4.274	wt.%	
S	Ka	2.52	0.710	0.323	0.0077	0.342	wt.%	
Ca	Ka	11.48	1.515	1.312	0.0312	1.736	wt.%	
Cr	Ka	0.56	0.335	0.066	0.0016	0.114	wt.%	
Mn	Ka	6.87	1.172	1.141	0.0272	2.069	wt.%	
Fe	Ka	146.05	5.404	29.686	0.7065	54.713	wt.%	
Co	Ka	9.31	1.364	2.260	0.0538	4.395	wt.%	
Ni	Ka	1.07	0.464	0.334	0.0080	0.647	wt.%	
				100.000		100.000	wt.%	Total

kV	15.0
Takeoff Angle	35.0°
Elapsed Livetime	20.0

Locality L6809, *Campeloma* sp. Nodule
SEM Location 2, matrix near *Campeloma* sp., S4725, EDS Run 2

Component	Conc.		
Mn	1.328	wt.%	
Si	7.980	wt.%	
Fe	30.616	wt.%	
C	6.712	wt.%	
Co	2.052	wt.%	
Ni	0.223	wt.%	
O	37.550	wt.%	
F	5.527	wt.%	
Na	0.727	wt.%	
Mg	0.679	wt.%	
Al	2.911	wt.%	
P	0.380	wt.%	
S	0.267	wt.%	
K	0.671	wt.%	
Ca	2.377	wt.%	
Zr	0.000	wt.%	
	100.000	wt.%	Total

Elt.	Line	Intensity (c/s)	Error 2-sig	Atomic %	Atomic Ratio	Conc	
C	Ka	35.77	2.674	12.828	0.2381	6.712	wt.%
O	Ka	576.48	10.736	53.874	1.0000	37.550	wt.%
F	Ka	69.68	3.733	6.678	0.1240	5.527	wt.%
Na	Ka	18.89	1.944	0.726	0.0135	0.727	wt.%
Mg	Ka	25.49	2.258	0.641	0.0119	0.679	wt.%
Al	Ka	127.71	5.053	2.477	0.0460	2.911	wt.%
Si	Ka	388.95	8.819	6.522	0.1211	7.980	wt.%
P	Ka	17.04	1.846	0.281	0.0052	0.380	wt.%
S	Ka	12.14	1.558	0.191	0.0036	0.267	wt.%
K	Ka	27.51	2.345	0.394	0.0073	0.671	wt.%
Ca	Ka	92.76	4.307	1.361	0.0253	2.377	wt.%
Mn	Ka	25.65	2.265	0.555	0.0103	1.328	wt.%
Fe	Ka	486.46	9.863	12.584	0.2336	30.616	wt.%
Co	Ka	25.87	2.274	0.799	0.0148	2.052	wt.%
Ni	Ka	2.24	0.670	0.087	0.0016	0.223	wt.%
Zr	La	0.00	0.000	0.000	0.0000	0.000	wt.%
				100.000		100.000	wt.%

kV	15.0
Takeoff Angle	35.0°
Elapsed Livetime	20.0

Locality L6809, S4725, *Campeloma* sp.
SEM Location 1, EDS Runs 1 – 5

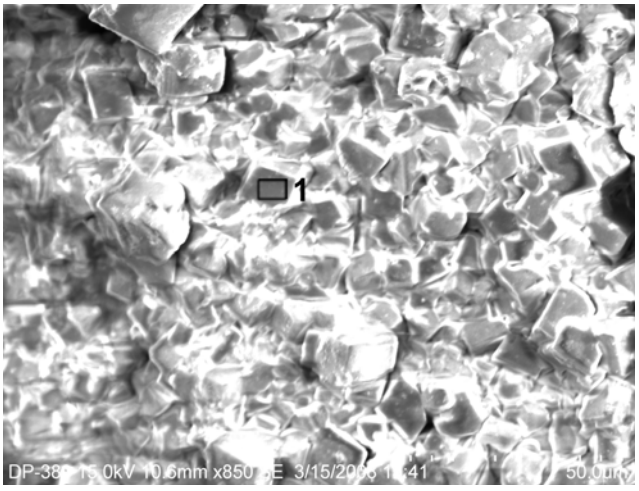

EDS Run 1 on *Campeloma* sp.

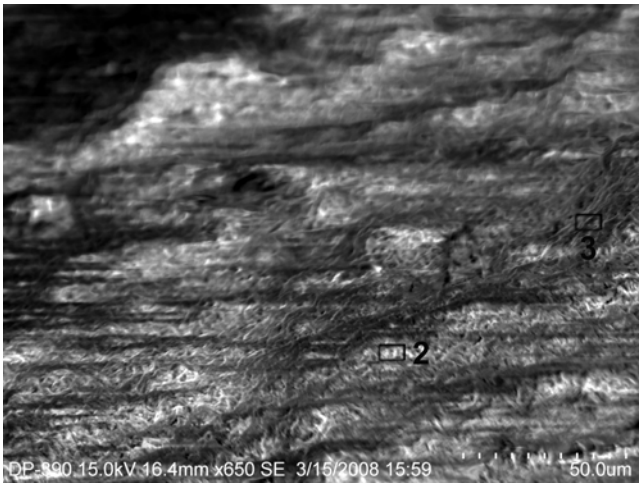

EDS Runs 2 – 3 on *Campeloma* sp.

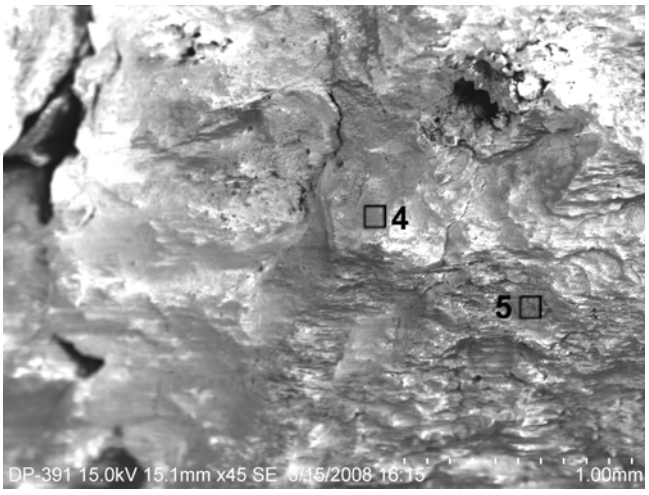

EDS Runs 4 – 5 on *Campeloma* sp.

Locality L6809, S4725, *Campeloma* sp.
SEM Location 1, EDS Run 1

Component	Conc.		
Mn	2.809	wt.%	
Si	0.973	wt.%	
Fe	44.936	wt.%	
C	0.000	wt.%	
Co	2.905	wt.%	
Ni	0.375	wt.%	
O	38.849	wt.%	
F	6.011	wt.%	
Mg	0.702	wt.%	
Ca	2.403	wt.%	
Rb	0.037	wt.%	
	100.000	wt.%	Total

Elt.	Line	Intensity (c/s)	Error 2-sig	Atomic %	Atomic Ratio	Conc		
C	Ka	0.00	0.000	0.000	0.0000	0.000	wt.%	
O	Ka	174.83	5.913	64.238	1.0000	38.849	wt.%	
F	Ka	18.76	1.937	8.371	0.1303	6.011	wt.%	
Mg	Ka	5.46	1.045	0.764	0.0119	0.702	wt.%	
Si	Ka	10.57	1.454	0.916	0.0143	0.973	wt.%	
Ca	Ka	22.65	2.128	1.586	0.0247	2.403	wt.%	
Mn	Ka	13.07	1.617	1.353	0.0211	2.809	wt.%	
Fe	Ka	169.36	5.820	21.288	0.3314	44.936	wt.%	
Co	Ka	8.68	1.317	1.304	0.0203	2.905	wt.%	
Ni	Ka	0.88	0.420	0.169	0.0026	0.375	wt.%	
Rb	La	0.18	0.191	0.012	0.0002	0.037	wt.%	
				100.000		100.000	wt.%	Total

kV	15.0
Takeoff Angle	35.0°
Elapsed Livetime	20.0

Locality L6809, S4725, *Campeloma* sp.
SEM Location 1, EDS Run 2

Component	Conc.		
Mn	0.841	wt.%	
Si	5.592	wt.%	
Fe	10.208	wt.%	
C	9.250	wt.%	
Co	0.631	wt.%	
Ni	0.137	wt.%	
O	49.070	wt.%	
F	3.451	wt.%	
Na	0.407	wt.%	
Mg	0.646	wt.%	
Al	2.782	wt.%	
P	1.340	wt.%	
S	0.560	wt.%	
Ca	14.946	wt.%	
Zr	0.000	wt.%	
Mo	0.140	wt.%	
	100.000	wt.%	Total

Elt.	Line	Intensity (c/s)	Error 2-sig	Atomic %	Atomic Ratio	Conc		
C	Ka	21.28	2.063	15.367	0.2511	9.250	wt.%	
O	Ka	183.96	6.065	61.199	1.0000	49.070	wt.%	
F	Ka	10.94	1.479	3.625	0.0592	3.451	wt.%	
Na	Ka	4.35	0.933	0.353	0.0058	0.407	wt.%	
Mg	Ka	9.80	1.400	0.530	0.0087	0.646	wt.%	
Al	Ka	48.22	3.105	2.057	0.0336	2.782	wt.%	
Si	Ka	105.80	4.600	3.973	0.0649	5.592	wt.%	
P	Ka	23.21	2.154	0.863	0.0141	1.340	wt.%	
S	Ka	9.58	1.384	0.348	0.0057	0.560	wt.%	
Ca	Ka	207.54	6.442	7.441	0.1216	14.946	wt.%	
Mn	Ka	5.60	1.058	0.305	0.0050	0.841	wt.%	
Fe	Ka	57.22	3.382	3.648	0.0596	10.208	wt.%	
Co	Ka	2.81	0.750	0.214	0.0035	0.631	wt.%	
Ni	Ka	0.49	0.314	0.046	0.0008	0.137	wt.%	
Zr	La	0.00	0.000	0.000	0.0000	0.000	wt.%	
Mo	La	1.14	0.477	0.029	0.0005	0.140	wt.%	
				100.000		100.000	wt.%	Tc

kV	15.0
Takeoff Angle	35.0°
Elapsed Livetime	20.0

Locality L6809, S4725, *Campeloma* sp.
SEM Location 1, EDS Run 3

Component	Conc.		
Mn	0.598	wt.%	
Si	2.842	wt.%	
Fe	10.014	wt.%	
C	13.111	wt.%	
Co	0.732	wt.%	
Ni	0.645	wt.%	
O	49.942	wt.%	
F	1.825	wt.%	
Na	0.462	wt.%	
Mg	0.648	wt.%	
Al	1.370	wt.%	
P	0.256	wt.%	
S	0.659	wt.%	
Ca	16.893	wt.%	
Zr	0.000	wt.%	
	100.000	wt.%	Total

Elt.	Line	Intensity (c/s)	Error 2-sig	Atomic %	Atomic Ratio	Conc		
C	Ka	37.28	2.730	21.106	0.3497	13.111	wt.%	
O	Ka	177.13	5.951	60.355	1.0000	49.942	wt.%	
F	Ka	5.64	1.062	1.858	0.0308	1.825	wt.%	
Na	Ka	4.95	0.994	0.389	0.0064	0.462	wt.%	
Mg	Ka	9.87	1.405	0.516	0.0085	0.648	wt.%	
Al	Ka	23.87	2.185	0.982	0.0163	1.370	wt.%	
Si	Ka	54.98	3.316	1.957	0.0324	2.842	wt.%	
P	Ka	4.63	0.963	0.160	0.0027	0.256	wt.%	
S	Ka	11.78	1.535	0.397	0.0066	0.659	wt.%	
Ca	Ka	240.09	6.929	8.150	0.1350	16.893	wt.%	
Mn	Ka	4.05	0.900	0.211	0.0035	0.598	wt.%	
Fe	Ka	57.04	3.377	3.467	0.0574	10.014	wt.%	
Co	Ka	3.31	0.813	0.240	0.0040	0.732	wt.%	
Ni	Ka	2.36	0.687	0.213	0.0035	0.645	wt.%	
Zr	La	0.00	0.000	0.000	0.0000	0.000	wt.%	
				100.000		100.000	wt.%	Total

kV	15.0
Takeoff Angle	35.0°
Elapsed Livetime	20.0

Locality L6809, S4725, *Campeloma* sp.
SEM Location 1, EDS Run 4

Component	Conc.		
Mn	1.232	wt.%	
Si	8.120	wt.%	
Fe	26.433	wt.%	
C	10.589	wt.%	
Co	1.906	wt.%	
Ni	0.126	wt.%	
O	39.506	wt.%	
F	3.871	wt.%	
Na	0.518	wt.%	
Mg	0.808	wt.%	
Al	3.364	wt.%	
P	0.753	wt.%	
S	0.152	wt.%	
Ca	2.187	wt.%	
Zr	0.000	wt.%	
Mo	0.434	wt.%	
	100.000	wt.%	Total

Elt.	Line	Intensity (c/s)	Error 2-sig	Atomic %	Atomic Ratio	Conc		
C	Ka	41.42	2.878	18.990	0.3570	10.589	wt.%	
O	Ka	421.56	9.181	53.186	1.0000	39.506	wt.%	
F	Ka	33.70	2.596	4.389	0.0825	3.871	wt.%	
Na	Ka	10.27	1.433	0.485	0.0091	0.518	wt.%	
Mg	Ka	23.03	2.146	0.716	0.0135	0.808	wt.%	
Al	Ka	111.07	4.713	2.686	0.0505	3.364	wt.%	
Si	Ka	294.51	7.674	6.227	0.1171	8.120	wt.%	
P	Ka	24.96	2.234	0.523	0.0098	0.753	wt.%	
S	Ka	5.07	1.007	0.102	0.0019	0.152	wt.%	
Ca	Ka	62.32	3.530	1.175	0.0221	2.187	wt.%	
Mn	Ka	17.31	1.861	0.483	0.0091	1.232	wt.%	
Fe	Ka	306.30	7.826	10.196	0.1917	26.433	wt.%	
Co	Ka	17.53	1.872	0.697	0.0131	1.906	wt.%	
Ni	Ka	0.93	0.431	0.046	0.0009	0.126	wt.%	
Zr	La	0.00	0.000	0.000	0.0000	0.000	wt.%	
Mo	La	6.52	1.142	0.098	0.0018	0.434	wt.%	
				100.000		100.000	wt.%	Tc

kV	15.0
Takeoff Angle	35.0°
Elapsed Livetime	20.0

Locality L6809, S4725, *Campeloma* sp.
SEM Location 1, EDS Run 5

Component	Conc.		
Mn	0.719	wt.%	
Si	8.566	wt.%	
Fe	13.217	wt.%	
C	13.518	wt.%	
Co	2.437	wt.%	
Ni	1.388	wt.%	
O	46.909	wt.%	
F	5.539	wt.%	
Na	0.682	wt.%	
Mg	0.964	wt.%	
Al	3.036	wt.%	
P	0.590	wt.%	
Ca	2.435	wt.%	
Zr	0.000	wt.%	
	100.000	wt.%	Total

Elt.	Line	Intensity (c/s)	Error 2-sig	Atomic %	Atomic Ratio	Conc		
C	Ka	5.43	1.042	21.518	0.3839	13.518	wt.%	
O	Ka	46.52	3.050	56.056	1.0000	46.909	wt.%	
F	Ka	4.00	0.894	5.575	0.0994	5.539	wt.%	
Na	Ka	1.38	0.525	0.568	0.0101	0.682	wt.%	
Mg	Ka	2.77	0.744	0.758	0.0135	0.964	wt.%	
Al	Ka	9.97	1.412	2.151	0.0384	3.036	wt.%	
Si	Ka	30.67	2.477	5.832	0.1040	8.566	wt.%	
P	Ka	1.90	0.616	0.364	0.0065	0.590	wt.%	
Ca	Ka	6.56	1.145	1.161	0.0207	2.435	wt.%	
Mn	Ka	0.95	0.437	0.250	0.0045	0.719	wt.%	
Fe	Ka	14.56	1.706	4.525	0.0807	13.217	wt.%	
Co	Ka	2.12	0.651	0.790	0.0141	2.437	wt.%	
Ni	Ka	0.97	0.441	0.452	0.0081	1.388	wt.%	
Zr	La	0.00	0.000	0.000	0.0000	0.000	wt.%	
				100.000		100.000	wt.%	Total

kV	15.0
Takeoff Angle	35.0°
Elapsed Livetime	20.0

Locality L6521, Nodule T13
SEM EDS Runs 1 – 5, run locations were not recorded on images
Magnifications as noted on image

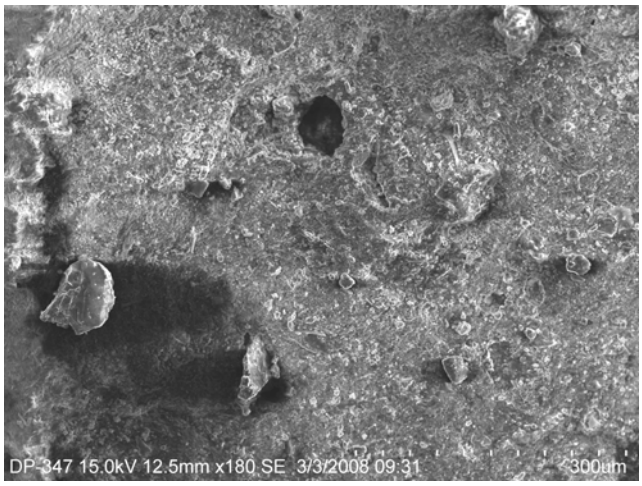

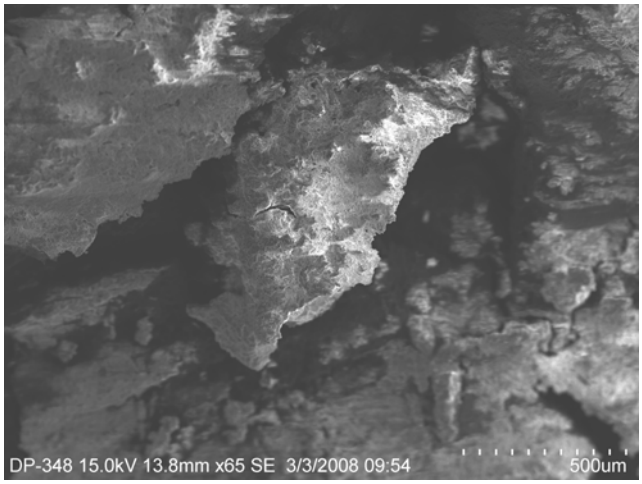

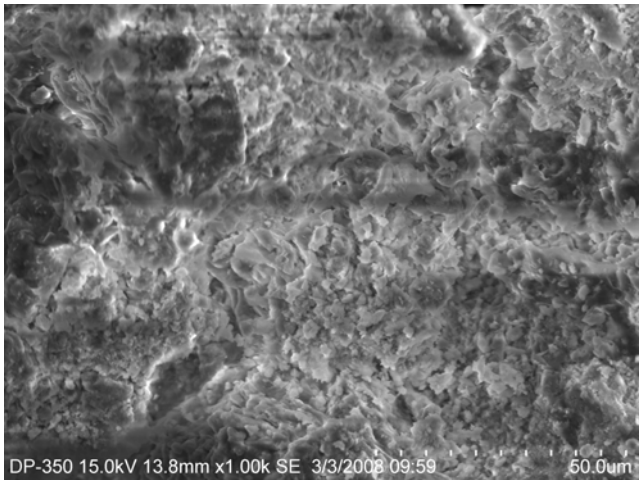

Locality L6521, Nodule T13
SEM EDS Run 1

Component	Conc.		
H	0.000	wt.%	
Mn	0.209	wt.%	
Zn	0.173	wt.%	
Ti	0.469	wt.%	
F	0.000	wt.%	
Cl	0.048	wt.%	
Fe	3.749	wt.%	
Cu	0.279	wt.%	
Cr	0.114	wt.%	
N	0.000	wt.%	
C	7.671	wt.%	
O	44.166	wt.%	
Si	29.448	wt.%	
Al	11.711	wt.%	
Na	0.749	wt.%	
Mg	1.212	wt.%	
S	0.000	wt.%	
K	0.000	wt.%	
Ca	0.000	wt.%	
Rb	0.000	wt.%	
Mo	0.000	wt.%	
Np	0.000	wt.%	
Pu	0.000	wt.%	
	100.000	wt.%	Total

Elt.	Line	Intensity (c/s)	Error 2-sig	Atomic %	Atomic Ratio	Conc	
H	Ka	0.00	0.000	0.000	0.0000	0.000	wt.%
C	Ka	11.04	1.485	12.633	0.2314	7.671	wt.%
N	Ka	0.00	0.000	0.000	0.0000	0.000	wt.%
O	Ka	281.32	7.499	54.604	1.0000	44.166	wt.%
F	Ka	0.00	0.000	0.000	0.0000	0.000	wt.%
Na	Ka	13.91	1.668	0.645	0.0118	0.749	wt.%
Mg	Ka	30.20	2.457	0.987	0.0181	1.212	wt.%
Al	Ka	316.51	7.954	8.586	0.1572	11.711	wt.%
Si	Ka	758.12	12.311	20.740	0.3798	29.448	wt.%
S	Ka	0.00	0.000	0.000	0.0000	0.000	wt.%
Cl	Ka	0.97	0.440	0.027	0.0005	0.048	wt.%
K	Ka	0.00	0.000	0.000	0.0000	0.000	wt.%
Ca	Ka	0.00	0.000	0.000	0.0000	0.000	wt.%
Ti	Ka	6.58	1.147	0.194	0.0035	0.469	wt.%
Cr	Ka	1.25	0.500	0.043	0.0008	0.114	wt.%
Mn	Ka	1.89	0.614	0.075	0.0014	0.209	wt.%
Fe	Ka	28.57	2.390	1.328	0.0243	3.749	wt.%

Locality L6521, Nodule T13
SEM EDS Run 2

Component	Conc.		
Fe	19.867	wt.%	
O	41.855	wt.%	
Si	18.699	wt.%	
Al	8.098	wt.%	
Ca	4.963	wt.%	
P	2.392	wt.%	
K	1.325	wt.%	
Mg	1.339	wt.%	
Mn	1.461	wt.%	
	100.000	wt.%	Total

Elt.	Line	Intensity (c/s)	Error 2-sig	Atomic %	Atomic Ratio	Conc		
O	Ka	161.82	5.688	61.490	1.0000	41.855	wt.%	
Mg	Ka	16.68	1.826	1.295	0.0211	1.339	wt.%	
Al	Ka	113.61	4.766	7.055	0.1147	8.098	wt.%	
Si	Ka	270.67	7.357	15.650	0.2545	18.699	wt.%	
P	Ka	29.21	2.417	1.815	0.0295	2.392	wt.%	
K	Ka	15.22	1.745	0.797	0.0130	1.325	wt.%	
Ca	Ka	53.95	3.284	2.911	0.0473	4.963	wt.%	
Mn	Ka	7.90	1.257	0.625	0.0102	1.461	wt.%	
Fe	Ka	90.06	4.244	8.362	0.1360	19.867	wt.%	
				100.000		100.000	wt.%	Total

kV	15.0
Takeoff Angle	35.0°
Elapsed Livetime	20.0

Locality L6521, Nodule T13
SEM EDS Run 3

Component	Conc.		
Fe	23.388	wt.%	
O	29.927	wt.%	
Si	18.665	wt.%	
Al	8.898	wt.%	
Ca	5.719	wt.%	
P	1.168	wt.%	
K	2.453	wt.%	
Mg	0.859	wt.%	
Mn	3.542	wt.%	
C	5.382	wt.%	
	100.000	wt.%	Total

Elt.	Line	Intensity (c/s)	Error 2-sig	Atomic %	Atomic Ratio	Conc		
C	Ka	2.70	0.734	10.997	0.2396	5.382	wt.%	
O	Ka	46.07	3.035	45.906	1.0000	29.927	wt.%	
Mg	Ka	4.86	0.986	0.867	0.0189	0.859	wt.%	
Al	Ka	57.10	3.379	8.093	0.1763	8.898	wt.%	
Si	Ka	122.75	4.954	16.310	0.3553	18.665	wt.%	
P	Ka	6.53	1.142	0.926	0.0202	1.168	wt.%	
K	Ka	13.03	1.614	1.539	0.0335	2.453	wt.%	
Ca	Ka	28.63	2.392	3.502	0.0763	5.719	wt.%	
Mn	Ka	8.83	1.329	1.582	0.0345	3.542	wt.%	
Fe	Ka	48.91	3.127	10.278	0.2239	23.388	wt.%	
				100.000		100.000	wt.%	Total

kV	15.0
Takeoff Angle	35.0°
Elapsed Livetime	20.0

Locality L6521, Nodule T13
SEM EDS Run 4

Component	Conc.		
Fe	4.736	wt.%	
O	38.603	wt.%	
Si	21.260	wt.%	
Al	10.632	wt.%	
Ca	10.402	wt.%	
P	0.000	wt.%	
K	0.620	wt.%	
Mg	0.362	wt.%	
Mn	0.666	wt.%	
C	12.060	wt.%	
In	0.658	wt.%	
	100.000	wt.%	Total

Elt.	Line	Intensity (c/s)	Error 2-sig	Atomic %	Atomic Ratio	Conc		
C	Ka	4.30	0.927	20.240	0.4161	12.060	wt.%	
O	Ka	33.56	2.590	48.637	1.0000	38.603	wt.%	
Mg	Ka	1.64	0.572	0.300	0.0062	0.362	wt.%	
Al	Ka	53.05	3.257	7.943	0.1633	10.632	wt.%	
Si	Ka	103.04	4.539	15.259	0.3137	21.260	wt.%	
P	Ka	0.00	0.000	0.000	0.0000	0.000	wt.%	
K	Ka	2.28	0.676	0.320	0.0066	0.620	wt.%	
Ca	Ka	35.76	2.674	5.232	0.1076	10.402	wt.%	
Mn	Ka	1.12	0.473	0.244	0.0050	0.666	wt.%	
Fe	Ka	6.74	1.161	1.709	0.0351	4.736	wt.%	
In	La	0.88	0.420	0.116	0.0024	0.658	wt.%	
				100.000		100.000	wt.%	Total

kV	15.0
Takeoff Angle	35.0°
Elapsed Livetime	20.0

Locality L6521, Nodule T13
SEM EDS Run 5

Component	Conc.		
Fe	18.295	wt.%	
O	35.642	wt.%	
Si	8.596	wt.%	
Al	3.311	wt.%	
Ca	22.350	wt.%	
P	1.302	wt.%	
K	0.579	wt.%	
Mg	0.920	wt.%	
Mn	0.570	wt.%	
In	0.352	wt.%	
C	3.685	wt.%	
F	2.380	wt.%	
Na	0.516	wt.%	
S	0.318	wt.%	
I	1.185	wt.%	
	100.000	wt.%	Total

Elt.	Line	Intensity (c/s)	Error 2-sig	Atomic %	Atomic Ratio	Conc		
C	Ka	3.17	0.796	7.441	0.1377	3.685	wt.%	
O	Ka	48.48	3.114	54.023	1.0000	35.642	wt.%	
F	Ka	3.66	0.855	3.038	0.0562	2.380	wt.%	
Na	Ka	2.28	0.676	0.544	0.0101	0.516	wt.%	
Mg	Ka	5.76	1.074	0.918	0.0170	0.920	wt.%	
Al	Ka	23.77	2.180	2.976	0.0551	3.311	wt.%	
Si	Ka	67.39	3.671	7.422	0.1374	8.596	wt.%	
P	Ka	9.25	1.360	1.020	0.0189	1.302	wt.%	
S	Ka	2.26	0.672	0.240	0.0044	0.318	wt.%	
K	Ka	3.79	0.871	0.359	0.0066	0.579	wt.%	
Ca	Ka	132.07	5.139	13.523	0.2503	22.350	wt.%	
Mn	Ka	1.62	0.569	0.251	0.0047	0.570	wt.%	
Fe	Ka	43.85	2.961	7.944	0.1471	18.295	wt.%	
In	La	0.87	0.418	0.074	0.0014	0.352	wt.%	
I	La	2.23	0.668	0.226	0.0042	1.185	wt.%	
				100.000		100.000	wt.%	Total

kV	15.0
Takeoff Angle	35.0°
Elapsed Livetime	20.0

Appendix C

Geochemist's Workbench® Rxn Calculations for Siderite Replacement of Aragonite

Standard Conditions Aragonite + Fe^{2+} = Ca^{2+} + Siderite

Log K's:

0 ˚C:	1.9824	150 ˚C:	2.4849
25 ˚C:	2.0993	200 ˚C:	2.5989
60 ˚C:	2.2317	250 ˚C:	2.7117
100 ˚C:	2.3562	300 ˚C:	2.8473

Polynomial fit:

$\log K = 1.983 + (0.004922)T - (1.453 \times 10^{-5})T^2 + (2.772 \times 10^{-8})T^3 - (6.584 \times 10^{-12})T^4$

Log K at 25 ˚C = 2.0993

Assumptions implicit in equilibrium equation:

temperature = 25 ˚C
activity of Ca^{2+} = 1 mol/kg
activity of Fe^{2+} = 1 mol/kg

Equilibrium equation:

Products are favored

Test 1 (pH 6) Aragonite + Fe^{2+} = Ca^{2+} + Siderite

Log K's:

0 ˚C:	1.9824	150 ˚C:	2.4849
25 ˚C:	2.0993	200 ˚C:	2.5989
60 ˚C:	2.2317	250 ˚C:	2.7117
100 ˚C:	2.3562	300 ˚C:	2.8473

Polynomial fit:

$\log K = 1.983 + (0.004922)T - (1.453 \times 10^{-5})T^2 + (2.772 \times 10^{-8})T^3 - (6.584 \times 10^{-12})T^4$

Log K at 10 ˚C = 2.0310
(Value interpolated using polynomial fit)

Assumptions implicit in equilibrium equation:

temperature = 10 ˚C
activity of Ca^{2+} = 10^{-3} mol/kg
activity of Fe^{2+} = 10^{-7} mol/kg

Equilibrium equation:

Reactants are favored

Test 2 (pH 2) Aragonite + Fe^{2+} = Ca^{2+} + Siderite

Log K's:

0 ˚C:	1.9824	150 ˚C:	2.4849
25 ˚C:	2.0993	200 ˚C:	2.5989
60 ˚C:	2.2317	250 ˚C:	2.7117
100 ˚C:	2.3562	300 ˚C:	2.8473

Polynomial fit:

$\log K = 1.983 + (0.004922)T - (1.453 \times 10^{-5})T^2 + (2.772 \times 10^{-8})T^3 - (6.584 \times 10^{-12})T^4$

Log K at 10 ˚C = 2.0310

(Value interpolated using polynomial fit)

Assumptions implicit in equilibrium equation:

temperature = 10 ˚C

activity of Ca^{2+} = 10^{-3} mol/kg

activity of Fe^{2+} = 10^{-7} mol/kg

Equilibrium equation:

Reactants are favored

Test 3 (pH 13) Aragonite + Fe^{2+} = Ca^{2+} + Siderite

Log K's:

0 ˚C:	1.9824	150 ˚C:	2.4849
25 ˚C:	2.0993	200 ˚C:	2.5989
60 ˚C:	2.2317	250 ˚C:	2.7117
100 ˚C:	2.3562	300 ˚C:	2.8473

Polynomial fit:

$\log K = 1.983 + (0.004922)T - (1.453 \times 10^{-5})T^2 + (2.772 \times 10^{-8})T^3 - (6.584 \times 10^{-12})T^4$

Log K at 10 ˚C = 2.0310

(Value interpolated using polynomial fit)

Assumptions implicit in equilibrium equation:

temperature = 10 ˚C

activity of Ca^{2+} = 10^{-3} mol/kg

activity of Fe^{2+} = 10^{-7} mol/kg

Equilibrium equation:

Reactants are favored

Test 4 (pH 6) Aragonite + Fe^{2+} = Ca^{2+} + Siderite

Log K's:

0 ˚C:	1.9824	150 ˚C:	2.4849
25 ˚C:	2.0993	200 ˚C:	2.5989
60 ˚C:	2.2317	250 ˚C:	2.7117
100 ˚C:	2.3562	300 ˚C:	2.8473

Polynomial fit:

$\log K = 1.983 + (0.004922)T - (1.453 \times 10^{-5})T^2 + (2.772 \times 10^{-8})T^3 - (6.584 \times 10^{-12})T^4$

Log K at 30 ˚C = 2.1186

(Value interpolated using polynomial fit)

Assumptions implicit in equilibrium equation:

temperature = 30 ˚C

activity of Ca^{2+} = 10^{-3} mol/kg

activity of Fe^{2+} = 10^{-7} mol/kg

Equilibrium equation:

Reactants are favored

Test 5 (pH 6) Aragonite + Fe^{2+} = Ca^{2+} + Siderite

Log K's:

0 ˚C:	1.9824	150 ˚C:	2.4849
25 ˚C:	2.0993	200 ˚C:	2.5989
60 ˚C:	2.2317	250 ˚C:	2.7117
100 ˚C:	2.3562	300 ˚C:	2.8473

Polynomial fit:

$\log K = 1.983 + (0.004922)T - (1.453 \times 10^{-5})T^2 + (2.772 \times 10^{-8})T^3 - (6.584 \times 10^{-12})T^4$

Log K at 10 ˚C = 2.0310

(Value interpolated using polynomial fit)

Assumptions implicit in equilibrium equation:

temperature = 10 ˚C

activity of Ca^{2+} = 10^{-3} mol/kg

activity of Fe^{2+} = 10^{-5} mol/kg

Equilibrium equation:

Products are favored

Test 6 (pH 2) Aragonite + Fe^{2+} = Ca^{2+} + Siderite

Log K's:

0 ˚C:	1.9824	150 ˚C:	2.4849
25 ˚C:	2.0993	200 ˚C:	2.5989
60 ˚C:	2.2317	250 ˚C:	2.7117
100 ˚C:	2.3562	300 ˚C:	2.8473

Polynomial fit:

$\log K = 1.983 + (0.004922)T - (1.453 \times 10^{-5})T^2 + (2.772 \times 10^{-8})T^3 - (6.584 \times 10^{-12})T^4$

Log K at 10 ˚C = 2.0310

(Value interpolated using polynomial fit)

Assumptions implicit in equilibrium equation:

temperature = 10 ˚C

activity of Ca^{2+} = 10^{-3} mol/kg

activity of Fe^{2+} = 10^{-5} mol/kg

Equilibrium equation:

Products are favored

Test 7 (pH 13) Aragonite + Fe^{2+} = Ca^{2+} + Siderite

Log K's:

0 ˚C:	1.9824	150 ˚C:	2.4849
25 ˚C:	2.0993	200 ˚C:	2.5989
60 ˚C:	2.2317	250 ˚C:	2.7117
100 ˚C:	2.3562	300 ˚C:	2.8473

Polynomial fit:

$\log K = 1.983 + (0.004922)T - (1.453 \times 10^{-5})T^2 + (2.772 \times 10^{-8})T^3 - (6.584 \times 10^{-12})T^4$

Log K at 10 ˚C = 2.0310

(Value interpolated using polynomial fit)

Assumptions implicit in equilibrium equation:

temperature = 10 ˚C

activity of Ca^{2+} = 10^{-3} mol/kg

activity of Fe^{2+} = 10^{-5} mol/kg

Equilibrium equation:

Products are favored

Test 8 (pH 6) Aragonite + Fe^{2+} = Ca^{2+} + Siderite

Log K's:

0 ˚C:	1.9824	150 ˚C:	2.4849
25 ˚C:	2.0993	200 ˚C:	2.5989
60 ˚C:	2.2317	250 ˚C:	2.7117
100 ˚C:	2.3562	300 ˚C:	2.8473

Polynomial fit:

$\log K = 1.983 + (0.004922)T - (1.453 \times 10^{-5})T^2 + (2.772 \times 10^{-8})T^3 - (6.584 \times 10^{-12})T^4$

Log K at 30 ˚C = 2.1186

(Value interpolated using polynomial fit)

Assumptions implicit in equilibrium equation:

temperature = 30 ˚C

activity of Ca^{2+} = 10^{-3} mol/kg

activity of Fe^{2+} = 10^{-5} mol/kg

Equilibrium equation:

Products are favored

Test 9 (pH 7) Aragonite + Fe^{2+} = Ca^{2+} + Siderite

Log K's:

0 ˚C:	1.9824	150 ˚C:	2.4849
25 ˚C:	2.0993	200 ˚C:	2.5989
60 ˚C:	2.2317	250 ˚C:	2.7117
100 ˚C:	2.3562	300 ˚C:	2.8473

Polynomial fit:

$\log K = 1.983 + (0.004922)T - (1.453 \times 10^{-5})T^2 + (2.772 \times 10^{-8})T^3 - (6.584 \times 10^{-12})T^4$

Log K at 10 ˚C = 2.0310

(Value interpolated using polynomial fit)

Assumptions implicit in equilibrium equation:

temperature = 10 ˚C

activity of Ca^{2+} = 10^{-3} mol/kg

activity of Fe^{2+} = 10^{-6} mol/kg

Equilibrium equation:

Reactants are favored

Test 10 (pH 7) Aragonite + Fe^{2+} = Ca^{2+} + Siderite

Log K's:

0 ˚C:	1.9824	150 ˚C:	2.4849
25 ˚C:	2.0993	200 ˚C:	2.5989
60 ˚C:	2.2317	250 ˚C:	2.7117
100 ˚C:	2.3562	300 ˚C:	2.8473

Polynomial fit:

$\log K = 1.983 + (0.004922)T - (1.453 \times 10^{-5})T^2 + (2.772 \times 10^{-8})T^3 - (6.584 \times 10^{-12})T^4$

Log K at 30 ˚C = 2.1186

(Value interpolated using polynomial fit)

Assumptions implicit in equilibrium equation:

temperature = 30 ˚C

activity of Ca^{2+} = 10^{-4} mol/kg

activity of Fe^{2+} = 10^{-6} mol/kg

Equilibrium equation:

Products are favored

Test 11 (pH 7) Aragonite + Fe^{2+} = Ca^{2+} + Siderite

Log K's:

0 ˚C:	1.9824	150 ˚C:	2.4849
25 ˚C:	2.0993	200 ˚C:	2.5989
60 ˚C:	2.2317	250 ˚C:	2.7117
100 ˚C:	2.3562	300 ˚C:	2.8473

Polynomial fit:

$\log K = 1.983 + (0.004922)T - (1.453 \times 10^{-5})T^2 + (2.772 \times 10^{-8})T^3 - (6.584 \times 10^{-12})T^4$

Log K at 30 ˚C = 2.1186

(Value interpolated using polynomial fit)

Assumptions implicit in equilibrium equation:

temperature = 30 ˚C

activity of Ca^{2+} = 10^{-4} mol/kg

activity of Fe^{2+} = 10^{-6} mol/kg

Equilibrium equation:

Products are favored

Test 12 (pH 7) Aragonite + Fe^{2+} = Ca^{2+} + Siderite

Log K's:

0 ˚C:	1.9824	150 ˚C:	2.4849
25 ˚C:	2.0993	200 ˚C:	2.5989
60 ˚C:	2.2317	250 ˚C:	2.7117
100 ˚C:	2.3562	300 ˚C:	2.8473

Polynomial fit:

$\log K = 1.983 + (0.004922)T - (1.453 \times 10^{-5})T^2 + (2.772 \times 10^{-8})T^3 - (6.584 \times 10^{-12})T^4$

Log K at 10 ˚C = 2.0310

(Value interpolated using polynomial fit)

Assumptions implicit in equilibrium equation:

temperature = 10 ˚C

activity of Ca^{2+} = 10^{-5} mol/kg

activity of Fe^{2+} = 10^{-7} mol/kg

Equilibrium equation:

Products are favored

Test 13 (pH 7) Aragonite + Fe^{2+} = Ca^{2+} + Siderite

Log K's:

0 ˚C:	1.9824	150 ˚C:	2.4849
25 ˚C:	2.0993	200 ˚C:	2.5989
60 ˚C:	2.2317	250 ˚C:	2.7117
100 ˚C:	2.3562	300 ˚C:	2.8473

Polynomial fit:

$\log K = 1.983 + (0.004922)T - (1.453 \times 10^{-5})T^2 + (2.772 \times 10^{-8})T^3 - (6.584 \times 10^{-12})T^4$

Log K at 30 ˚C = 2.1186

(Value interpolated using polynomial fit)

Assumptions implicit in equilibrium equation:

temperature = 30 ˚C

activity of Ca^{2+} = 10^{-5} mol/kg

activity of Fe^{2+} = 10^{-7} mol/kg

Equilibrium equation:

Products are favored

Test 14 (pH 6) Aragonite + Fe^{2+} = Ca^{2+} + Siderite

Log K's:

0 ˚C:	1.9824	150 ˚C:	2.4849
25 ˚C:	2.0993	200 ˚C:	2.5989
60 ˚C:	2.2317	250 ˚C:	2.7117
100 ˚C:	2.3562	300 ˚C:	2.8473

Polynomial fit:

$\log K = 1.983 + (0.004922)T - (1.453 \times 10^{-5})T^2 + (2.772 \times 10^{-8})T^3 - (6.584 \times 10^{-12})T^4$

Log K at 10 ˚C = 2.0310

(Value interpolated using polynomial fit)

Assumptions implicit in equilibrium equation:

temperature = 10 ˚C

activity of Ca^{2+} = 10^{-7} mol/kg

activity of Fe^{2+} = 10^{-9} mol/kg

Equilibrium equation:

Products are favored

Test 15 (pH 7) Aragonite + Fe^{2+} = Ca^{2+} + Siderite

Log K's:

0 ˚C:	1.9824	150 ˚C:	2.4849
25 ˚C:	2.0993	200 ˚C:	2.5989
60 ˚C:	2.2317	250 ˚C:	2.7117
100 ˚C:	2.3562	300 ˚C:	2.8473

Polynomial fit:

$\log K = 1.983 + (0.004922)T - (1.453 \times 10^{-5})T^2 + (2.772 \times 10^{-8})T^3 - (6.584 \times 10^{-12})T^4$

Log K at 10 ˚C = 2.0310

(Value interpolated using polynomial fit)

Assumptions implicit in equilibrium equation:

temperature = 10 ˚C

activity of Ca^{2+} = $10^{-3.5}$ mol/kg

activity of Fe^{2+} = $10^{-5.5}$ mol/kg

Equilibrium equation:

Products are favored

Test 16 (pH 7) Aragonite + Fe^{2+} = Ca^{2+} + Siderite

Log K's:

0 ˚C:	1.9824	150 ˚C:	2.4849
25 ˚C:	2.0993	200 ˚C:	2.5989
60 ˚C:	2.2317	250 ˚C:	2.7117
100 ˚C:	2.3562	300 ˚C:	2.8473

Polynomial fit:

$\log K = 1.983 + (0.004922)T - (1.453 \times 10^{-5})T^2 + (2.772 \times 10^{-8})T^3 - (6.584 \times 10^{-12})T^4$

Log K at 10 ˚C = 2.0310

(Value interpolated using polynomial fit)

Assumptions implicit in equilibrium equation:

temperature = 10 ˚C

activity of Ca^{2+} = $10^{-3.5}$ mol/kg

activity of Fe^{2+} = $10^{-5.6}$ mol/kg

Equilibrium equation:

Reactants are favored

Test 17 (pH 7) Aragonite + Fe^{2+} = Ca^{2+} + Siderite

Log K's:

0 ˚C:	1.9824	150 ˚C:	2.4849
25 ˚C:	2.0993	200 ˚C:	2.5989
60 ˚C:	2.2317	250 ˚C:	2.7117
100 ˚C:	2.3562	300 ˚C:	2.8473

Polynomial fit:

$\log K = 1.983 + (0.004922)T - (1.453 \times 10^{-5})T^2 + (2.772 \times 10^{-8})T^3 - (6.584 \times 10^{-12})T^4$

Log K at 30 ˚C = 2.1186

(Value interpolated using polynomial fit)

Assumptions implicit in equilibrium equation:

temperature = 30 ˚C

activity of Ca^{2+} = $10^{-3.5}$ mol/kg

activity of Fe^{2+} = $10^{-5.6}$ mol/kg

Equilibrium equation:

Products are favored

Test 18 (pH 7) Aragonite + Fe^{2+} = Ca^{2+} + Siderite

Log K's:

0 ˚C:	1.9824	150 ˚C:	2.4849
25 ˚C:	2.0993	200 ˚C:	2.5989
60 ˚C:	2.2317	250 ˚C:	2.7117
100 ˚C:	2.3562	300 ˚C:	2.8473

Polynomial fit:

$\log K = 1.983 + (0.004922)T - (1.453 \times 10^{-5})T^2 + (2.772 \times 10^{-8})T^3 - (6.584 \times 10^{-12})T^4$

Log K at 30 ˚C = 2.1186

(Value interpolated using polynomial fit)

Assumptions implicit in equilibrium equation:

temperature = 30 ˚C

activity of Ca^{2+} = $10^{-3.5}$ mol/kg

activity of Fe^{2+} = $10^{-5.7}$ mol/kg

Equilibrium equation:

Reactants are favored

Test 19 (pH 7) Aragonite + Fe^{2+} = Ca^{2+} + Siderite

Log K's:

0 ˚C:	1.9824	150 ˚C:	2.4849
25 ˚C:	2.0993	200 ˚C:	2.5989
60 ˚C:	2.2317	250 ˚C:	2.7117
100 ˚C:	2.3562	300 ˚C:	2.8473

Polynomial fit:

$\log K = 1.983 + (0.004922)T - (1.453 \times 10^{-5})T^2 + (2.772 \times 10^{-8})T^3 - (6.584 \times 10^{-12})T^4$

Log K at 10 ˚C = 2.0310

(Value interpolated using polynomial fit)

Assumptions implicit in equilibrium equation:

temperature = 10 ˚C

activity of Ca^{2+} = $10^{-4.5}$ mol/kg

activity of Fe^{2+} = $10^{-6.5}$ mol/kg

Equilibrium equation:

Products are favored

Test 20 (pH 7) Aragonite + Fe^{2+} = Ca^{2+} + Siderite

Log K's:

0 ˚C:	1.9824	150 ˚C:	2.4849
25 ˚C:	2.0993	200 ˚C:	2.5989
60 ˚C:	2.2317	250 ˚C:	2.7117
100 ˚C:	2.3562	300 ˚C:	2.8473

Polynomial fit:

$\log K = 1.983 + (0.004922)T - (1.453 \times 10^{-5})T^2 + (2.772 \times 10^{-8})T^3 - (6.584 \times 10^{-12})T^4$

Log K at 10 ˚C = 2.0310

(Value interpolated using polynomial fit)

Assumptions implicit in equilibrium equation:

temperature = 10 ˚C

activity of Ca^{2+} = $10^{-4.5}$ mol/kg

activity of Fe^{2+} = $10^{-6.6}$ mol/kg

Equilibrium equation:

Reactants are favored

Test 21 (pH 7) Aragonite + Fe^{2+} = Ca^{2+} + Siderite

Log K's:

0 ˚C:	1.9824	150 ˚C:	2.4849
25 ˚C:	2.0993	200 ˚C:	2.5989
60 ˚C:	2.2317	250 ˚C:	2.7117
100 ˚C:	2.3562	300 ˚C:	2.8473

Polynomial fit:

$\log K = 1.983 + (0.004922)T - (1.453 \times 10^{-5})T^2 + (2.772 \times 10^{-8})T^3 - (6.584 \times 10^{-12})T^4$

Log K at 30 ˚C = 2.1186

(Value interpolated using polynomial fit)

Assumptions implicit in equilibrium equation:

temperature = 30 ˚C

activity of Ca^{2+} = $10^{-4.5}$ mol/kg

activity of Fe^{2+} = $10^{-6.6}$ mol/kg

Equilibrium equation:

Products are favored

Test 22 (pH 7) Aragonite + Fe^{2+} = Ca^{2+} + Siderite

Log K's:

0 ˚C:	1.9824	150 ˚C:	2.4849
25 ˚C:	2.0993	200 ˚C:	2.5989
60 ˚C:	2.2317	250 ˚C:	2.7117
100 ˚C:	2.3562	300 ˚C:	2.8473

Polynomial fit:

$\log K = 1.983 + (0.004922)T - (1.453 \times 10^{-5})T^2 + (2.772 \times 10^{-8})T^3 - (6.584 \times 10^{-12})T^4$

Log K at 30 ˚C = 2.1186

(Value interpolated using polynomial fit)

Assumptions implicit in equilibrium equation:

temperature = 30 ˚C

activity of Ca^{2+} = $10^{-4.5}$ mol/kg

activity of Fe^{2+} = $10^{-6.7}$ mol/kg

Equilibrium equation:

Reactants are favored

Appendix D

Geochemist's Workbench® Act2 Eh-pH iron species stability diagrams

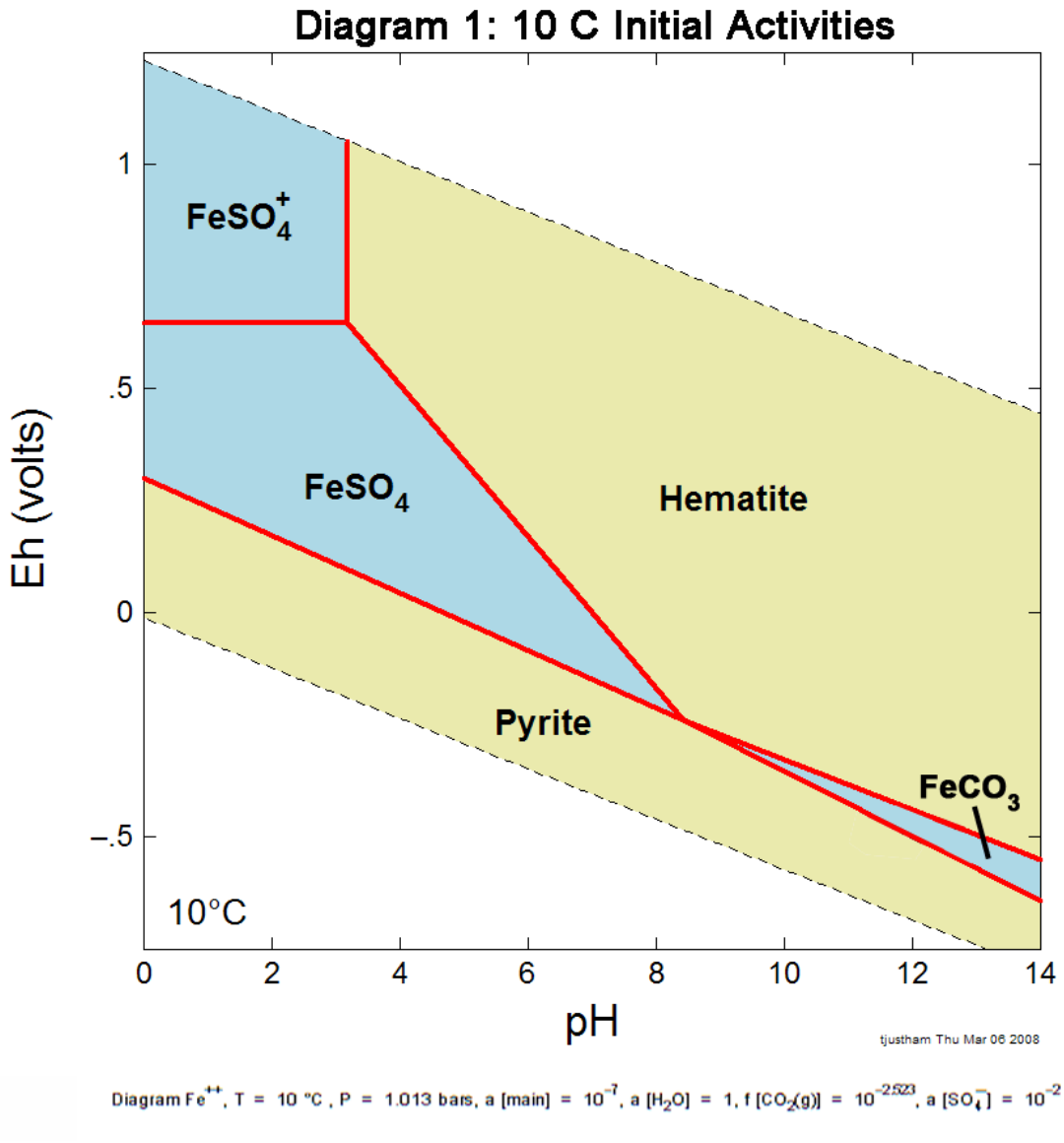

Diagram Fe^{++}, T = 10 °C , P = 1.013 bars, a [main] = 10^{-7}, a [H_2O] = 1, f [CO_2(g)] = $10^{-2.523}$, a [SO_4^{--}] = 10^{-2}

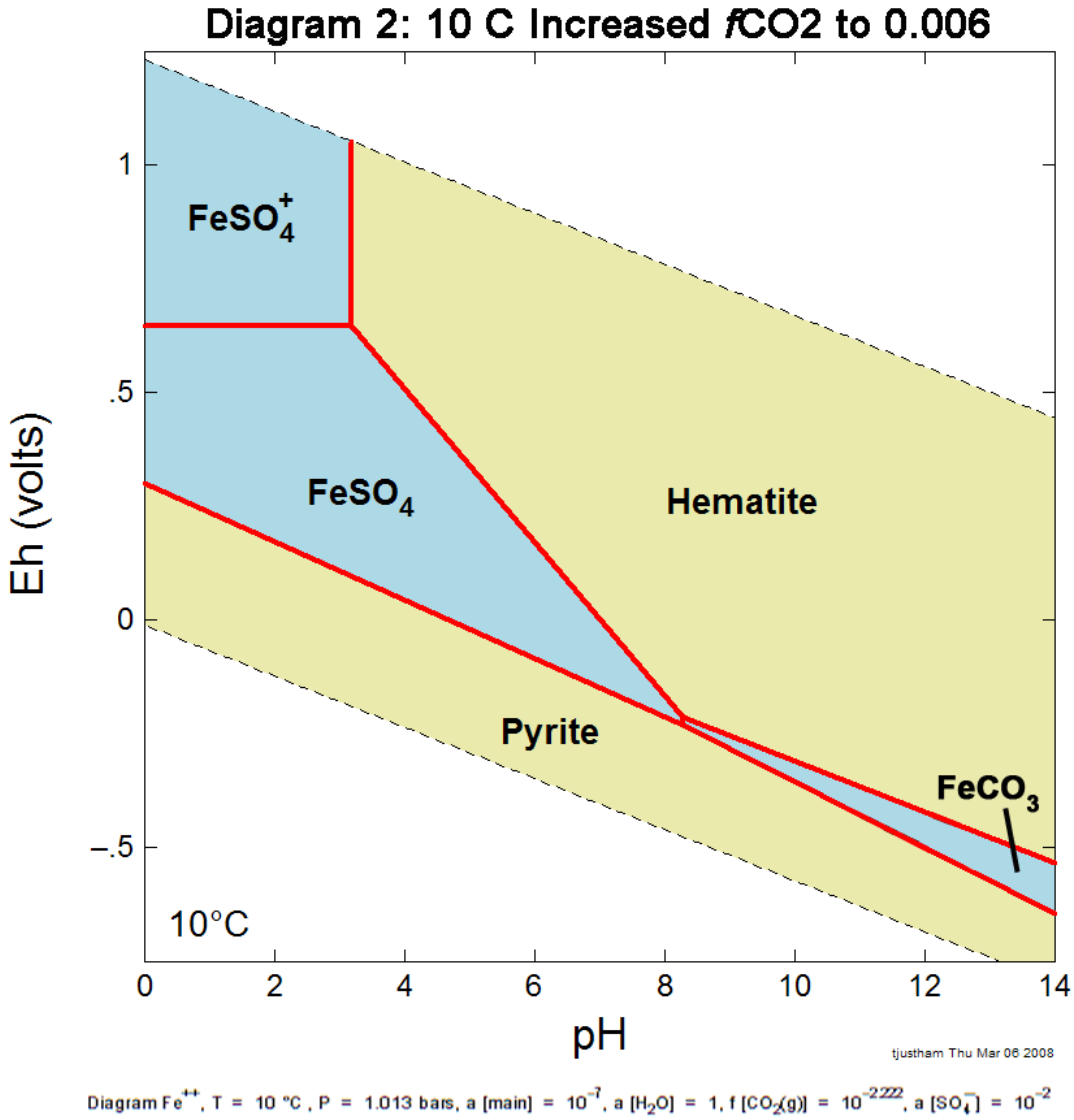
Diagram 2: 10 C Increased fCO2 to 0.006
Eh (volts)
1
.5
0
–.5
FeSO4+
FeSO4
Hematite
Pyrite
FeCO3
10°C
0
2
4
6
8
10
12
14
pH
tjustham Thu Mar 06 2008
Diagram Fe++, T = 10 °C, P = 1.013 bars, a [main] = 10-7, a [H2O] = 1, f [CO2(g)] = 10-2.222, a [SO4--] = 10-2

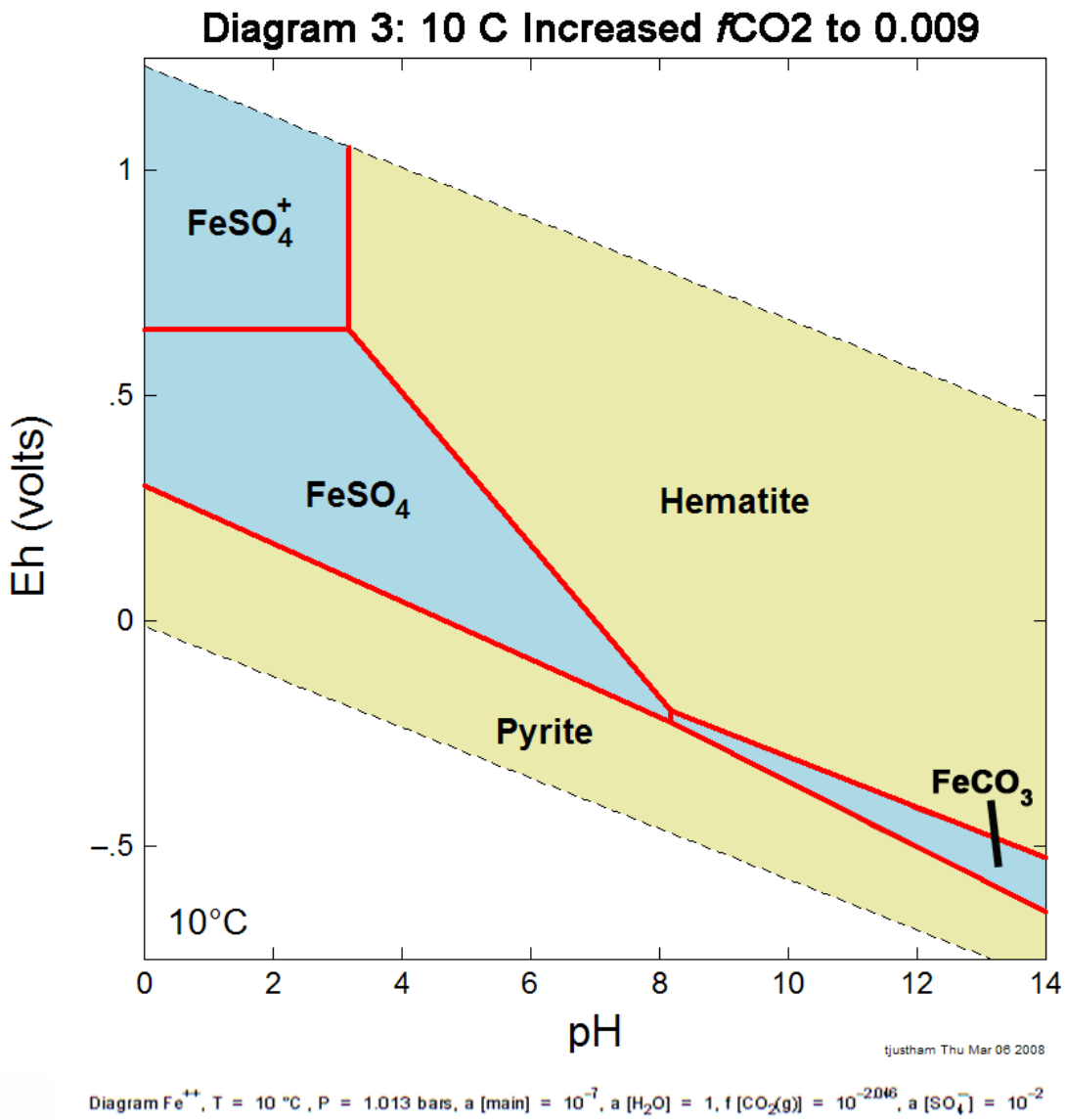
Diagram 3: 10 C Increased fCO2 to 0.009
Eh (volts)
1
.5
0
–.5
FeSO4+
FeSO4
Hematite
Pyrite
FeCO3
10°C
0
2
4
6
8
10
12
14
pH
tjustham Thu Mar 06 2008
Diagram Fe++, T = 10 °C , P = 1.013 bars, a [main] = 10-7, a [H2O] = 1, f [CO2(g)] = 10-2.046, a [SO4--] = 10-2

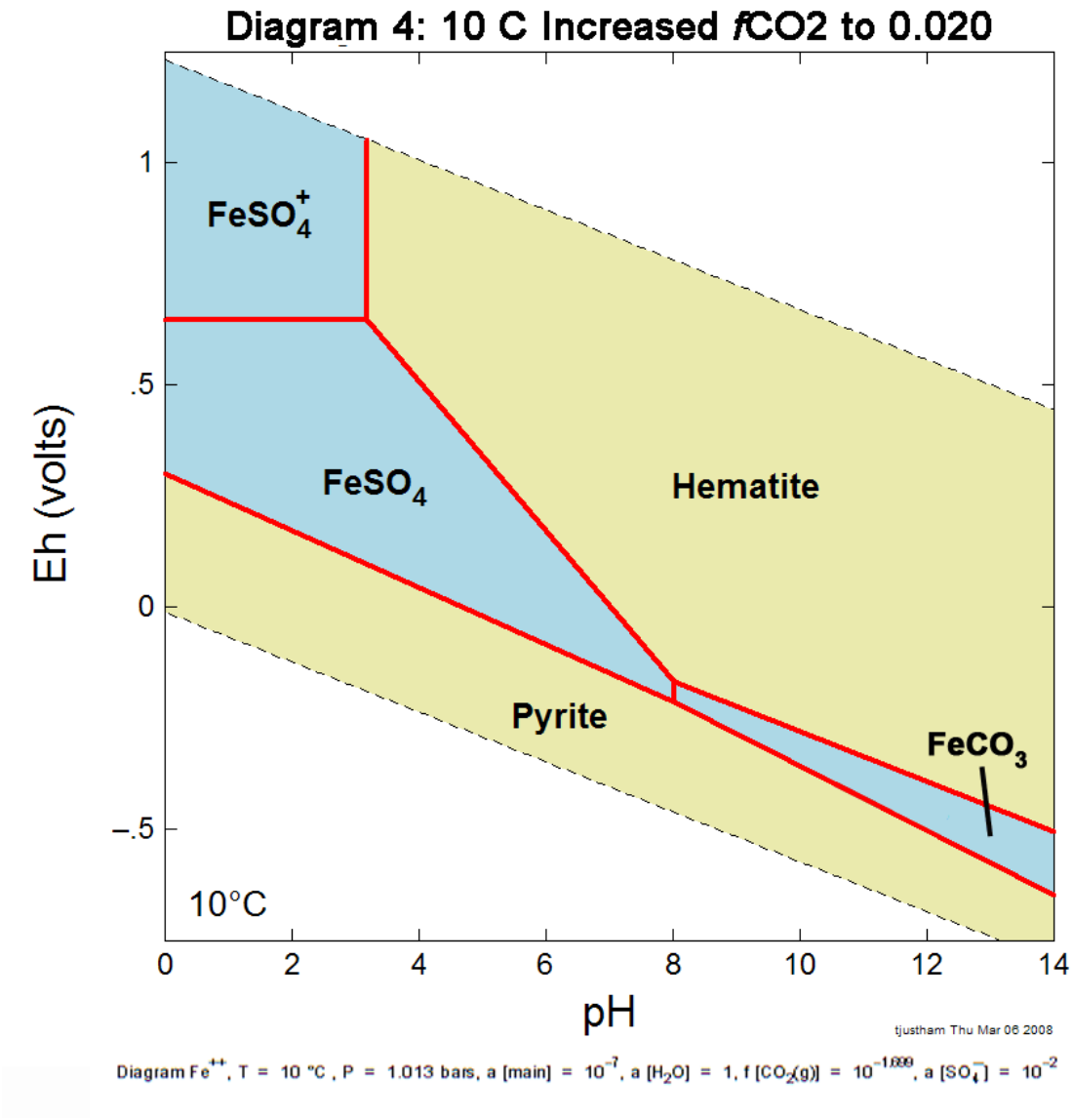
Diagram 4: 10 C Increased fCO2 to 0.020
FeSO4+
FeSO4
Hematite
Pyrite
FeCO3
10°C
Eh (volts)
pH
1
.5
0
–.5
0
2
4
6
8
10
12
14
tjustham Thu Mar 06 2008
Diagram Fe++, T = 10 °C, P = 1.013 bars, a [main] = 10-7, a [H2O] = 1, f [CO2(g)] = 10-1.699, a [SO4--] = 10-2

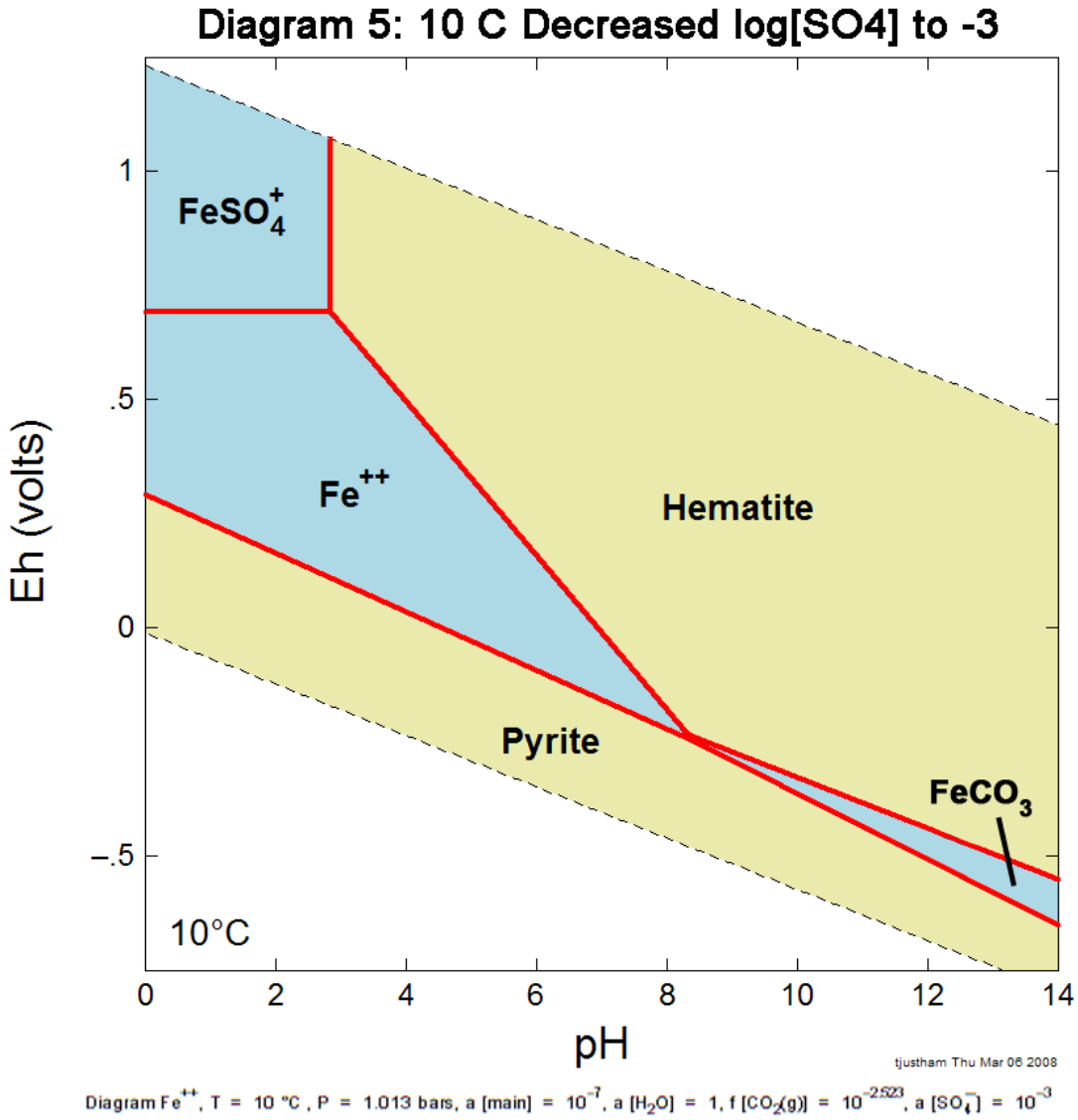
Diagram 5: 10 C Decreased log[SO4] to -3
Eh (volts)
1
.5
0
–.5
FeSO4+
Fe++
Hematite
Pyrite
FeCO3
10°C
0
2
4
6
8
10
12
14
pH
tjustham Thu Mar 06 2008
Diagram Fe++, T = 10 °C, P = 1.013 bars, a [main] = 10-7, a [H2O] = 1, f [CO2(g)] = 10-2.523, a [SO4--] = 10-3

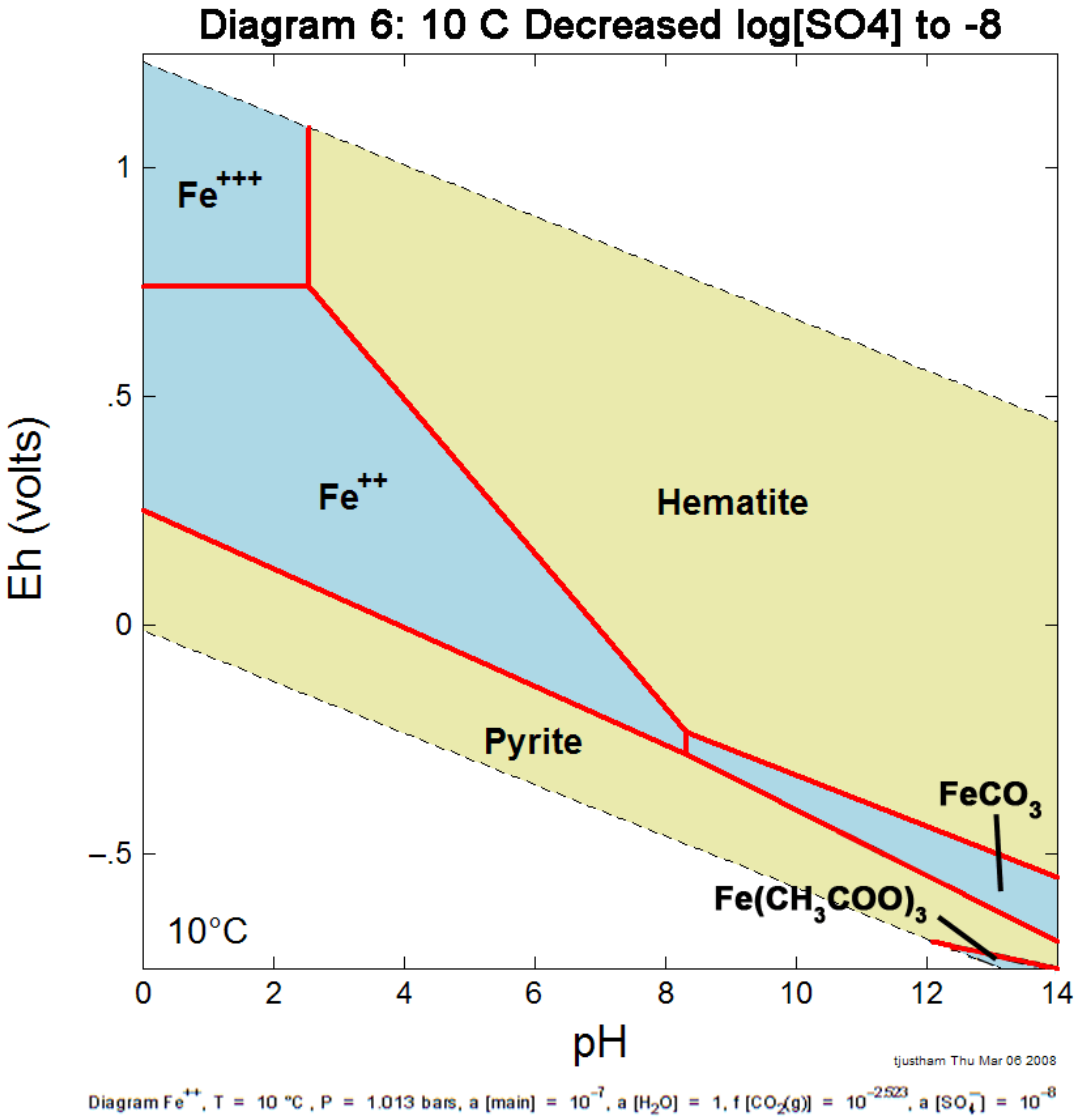
Diagram 6: 10 C Decreased log[SO4] to -8
Eh (volts)
1
.5
0
–.5
Fe+++
Fe++
Hematite
Pyrite
FeCO3
Fe(CH3COO)3
10°C
0
2
4
6
8
10
12
14
pH
tjustham Thu Mar 06 2008
Diagram Fe++, T = 10 °C , P = 1.013 bars, a [main] = 10-7, a [H2O] = 1, f [CO2(g)] = 10-2.523, a [SO4--] = 10-8

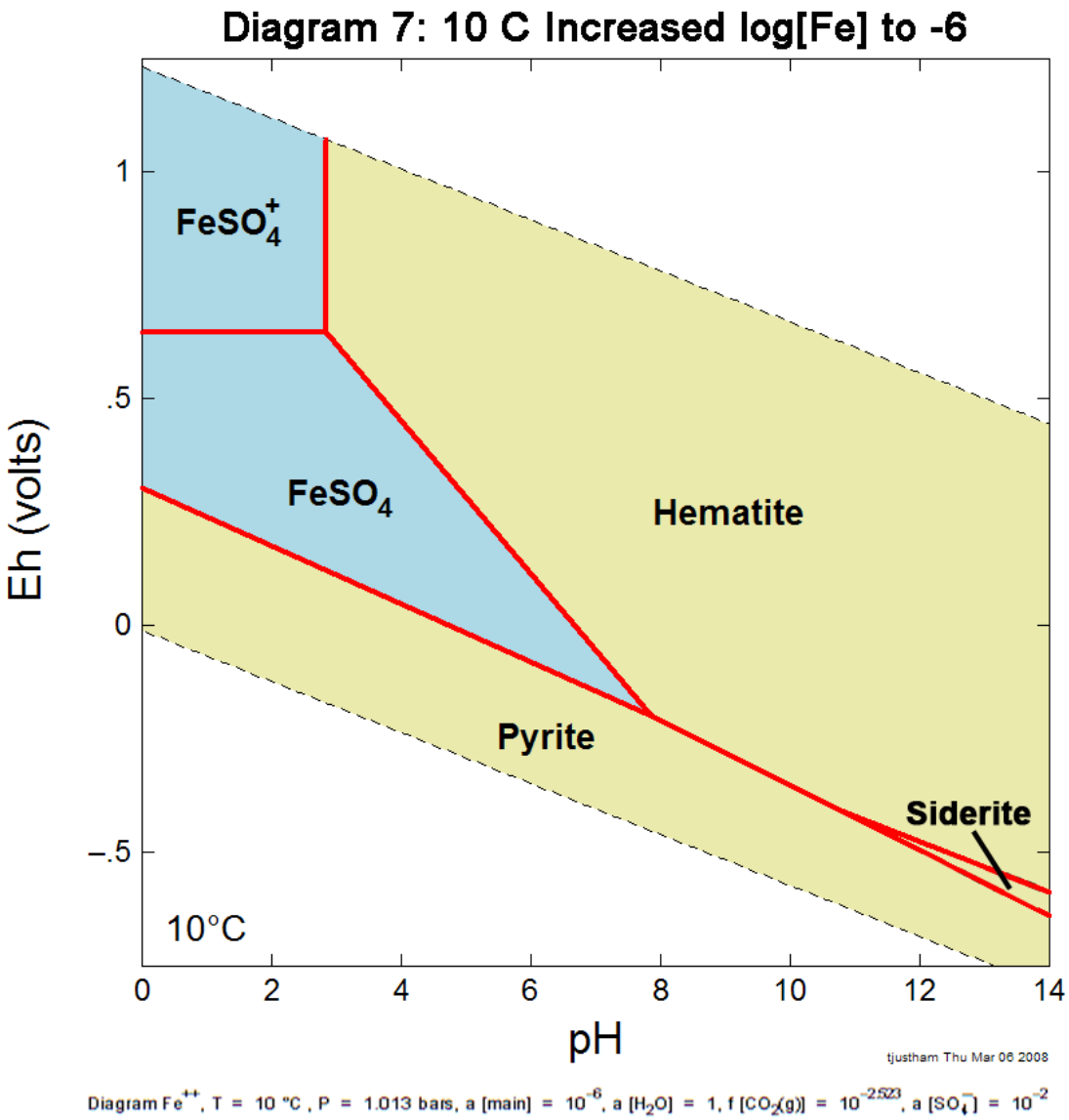
Diagram 7: 10 C Increased log[Fe] to -6
Eh (volts)
1
.5
0
–.5
FeSO4+
FeSO4
Hematite
Pyrite
Siderite
10°C
0
2
4
6
8
10
12
14
pH
tjustham Thu Mar 06 2008
Diagram Fe++, T = 10 °C , P = 1.013 bars, a [main] = 10-6, a [H2O] = 1, f [CO2(g)] = 10-2.523, a [SO4--] = 10-2

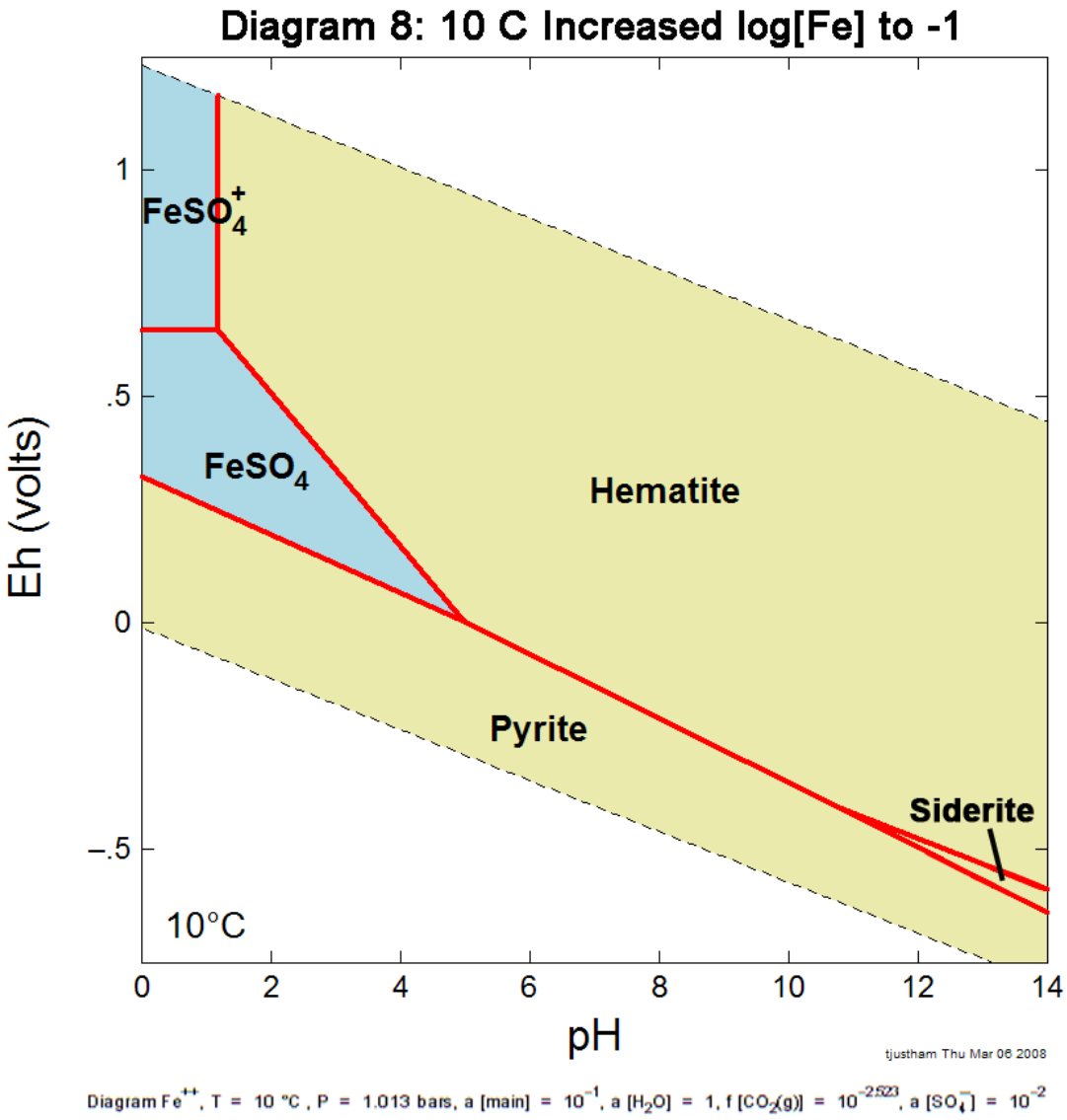
Diagram 8: 10 C Increased log[Fe] to -1
Eh (volts)
1
.5
0
–.5
FeSO4+
FeSO4
Hematite
Pyrite
Siderite
10°C
0
2
4
6
8
10
12
14
pH
tjustham Thu Mar 06 2008
Diagram Fe++, T = 10 °C , P = 1.013 bars, a [main] = 10-1, a [H2O] = 1, f [CO2(g)] = 10-2.523, a [SO4--] = 10-2

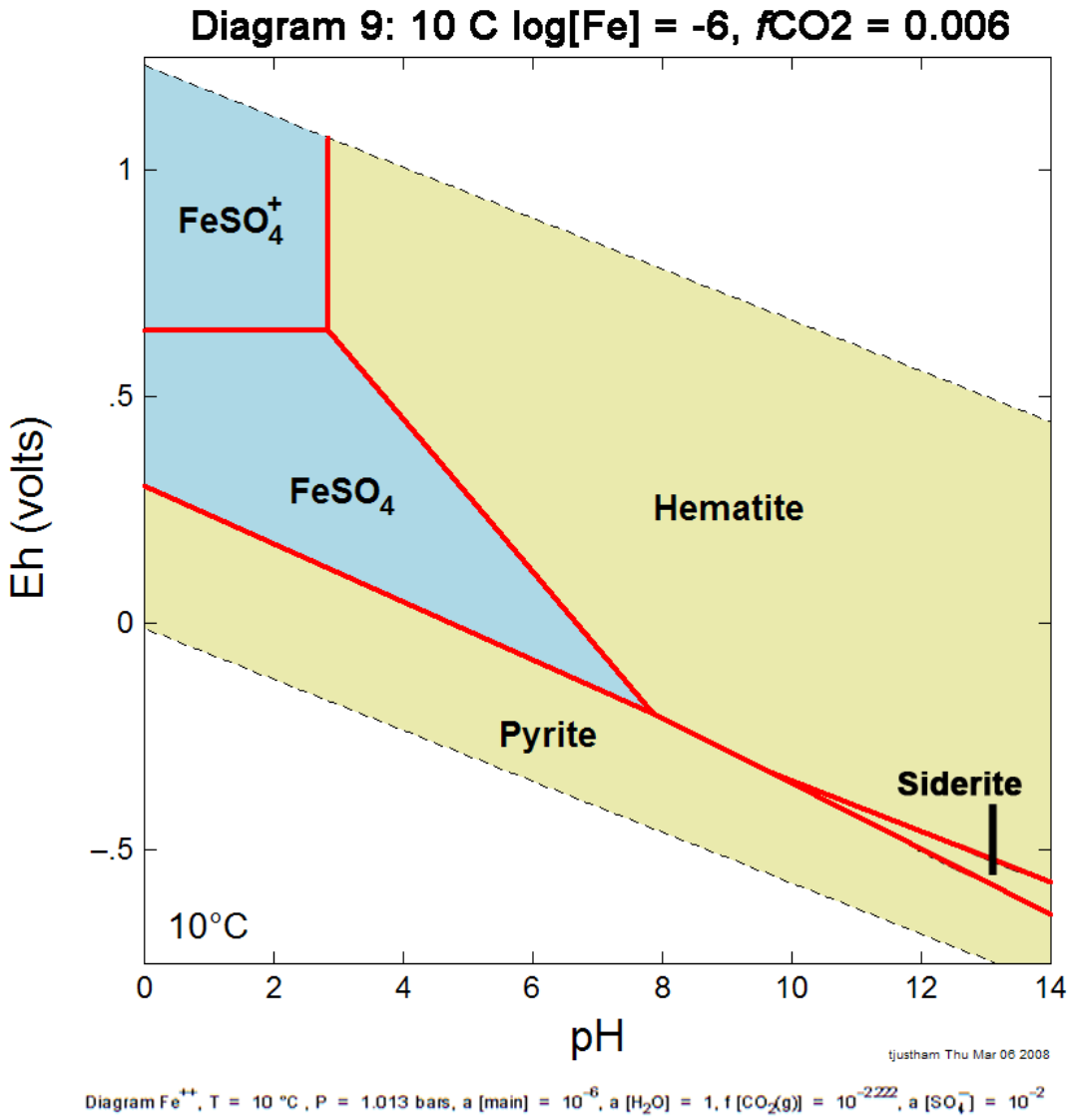
Diagram 9: 10 C log[Fe] = -6, fCO2 = 0.006
FeSO4+
FeSO4
Hematite
Pyrite
Siderite
10°C
Eh (volts)
pH
1
.5
0
–.5
0
2
4
6
8
10
12
14
tjustham Thu Mar 06 2008
Diagram Fe++, T = 10 °C , P = 1.013 bars, a [main] = 10-6, a [H2O] = 1, f [CO2(g)] = 10-2.222, a [SO4--] = 10-2

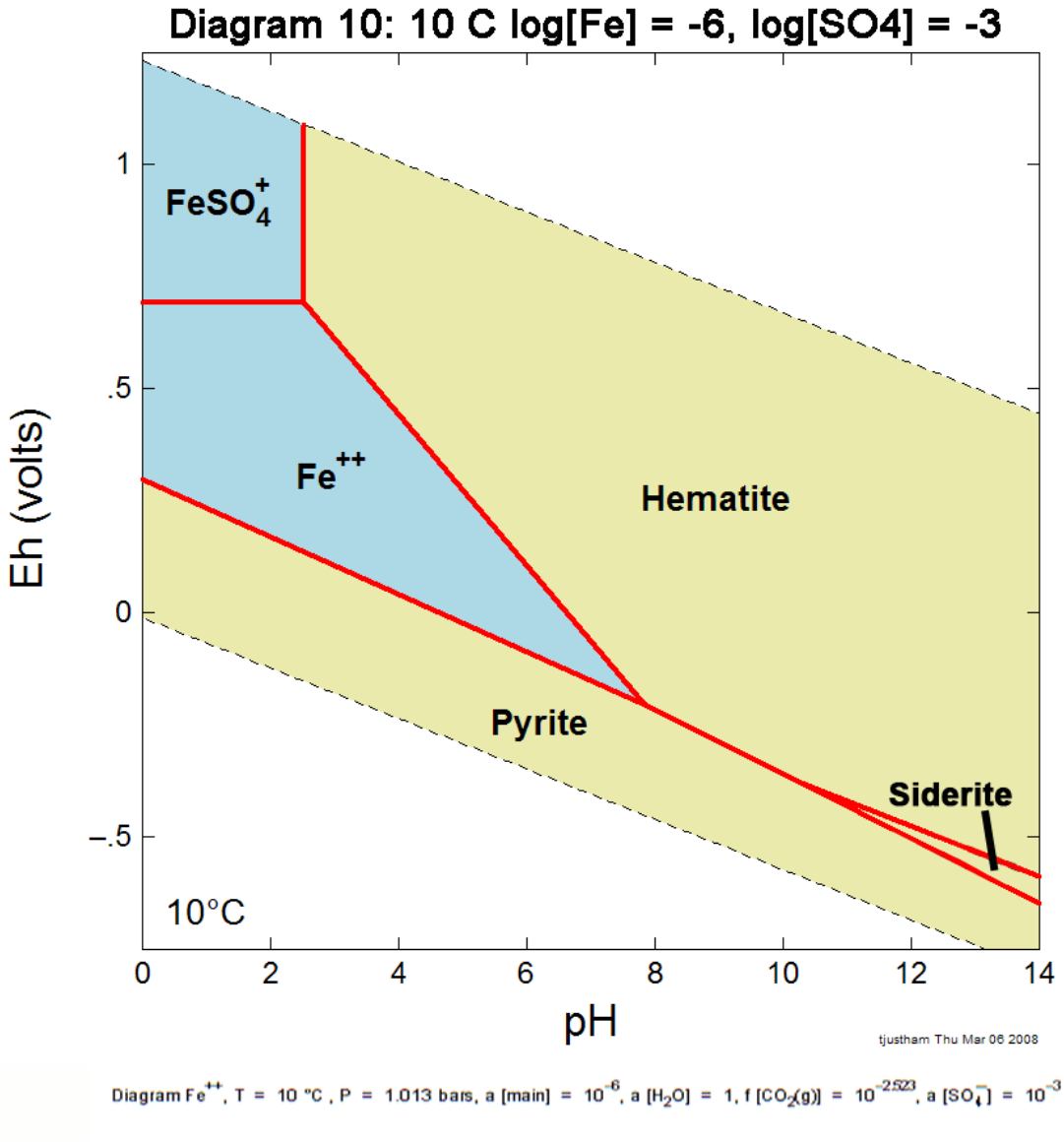
Diagram 10: 10 C log[Fe] = -6, log[SO4] = -3
FeSO4+
Fe++
Hematite
Pyrite
Siderite
10°C
Eh (volts)
pH
1
.5
0
–.5
0
2
4
6
8
10
12
14
tjustham Thu Mar 06 2008
Diagram Fe++, T = 10 °C , P = 1.013 bars, a [main] = 10-6, a [H2O] = 1, f [CO2(g)] = 10-2.523, a [SO4--] = 10-3

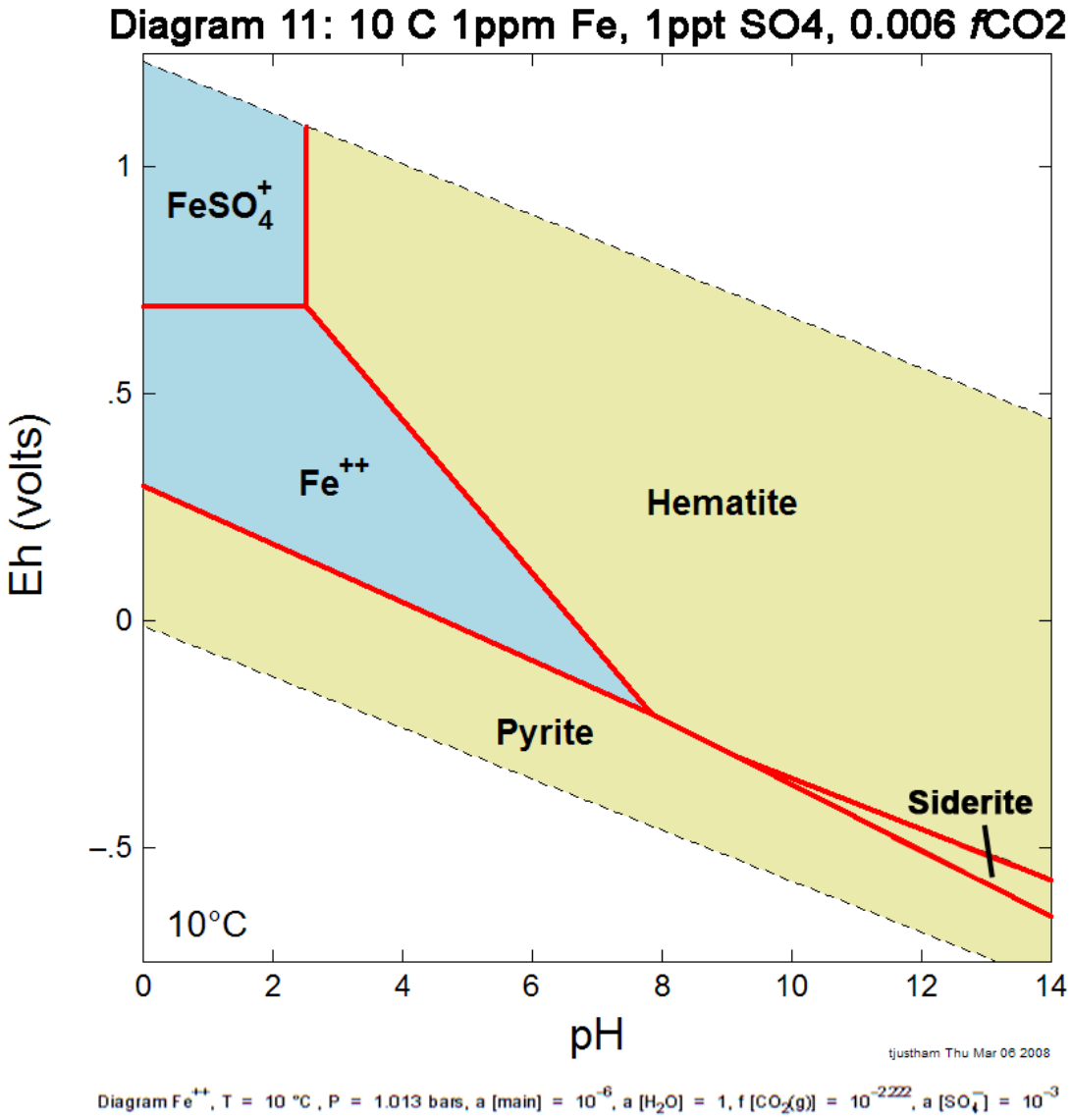
Diagram 11: 10 C 1ppm Fe, 1ppt SO4, 0.006 fCO2
FeSO4+
Fe++
Hematite
Pyrite
Siderite
10°C
Eh (volts)
pH
1
.5
0
–.5
0
2
4
6
8
10
12
14
tjustham Thu Mar 06 2008
Diagram Fe++, T = 10 °C , P = 1.013 bars, a [main] = 10-6, a [H2O] = 1, f [CO2(g)] = 10-2.222, a [SO4--] = 10-3

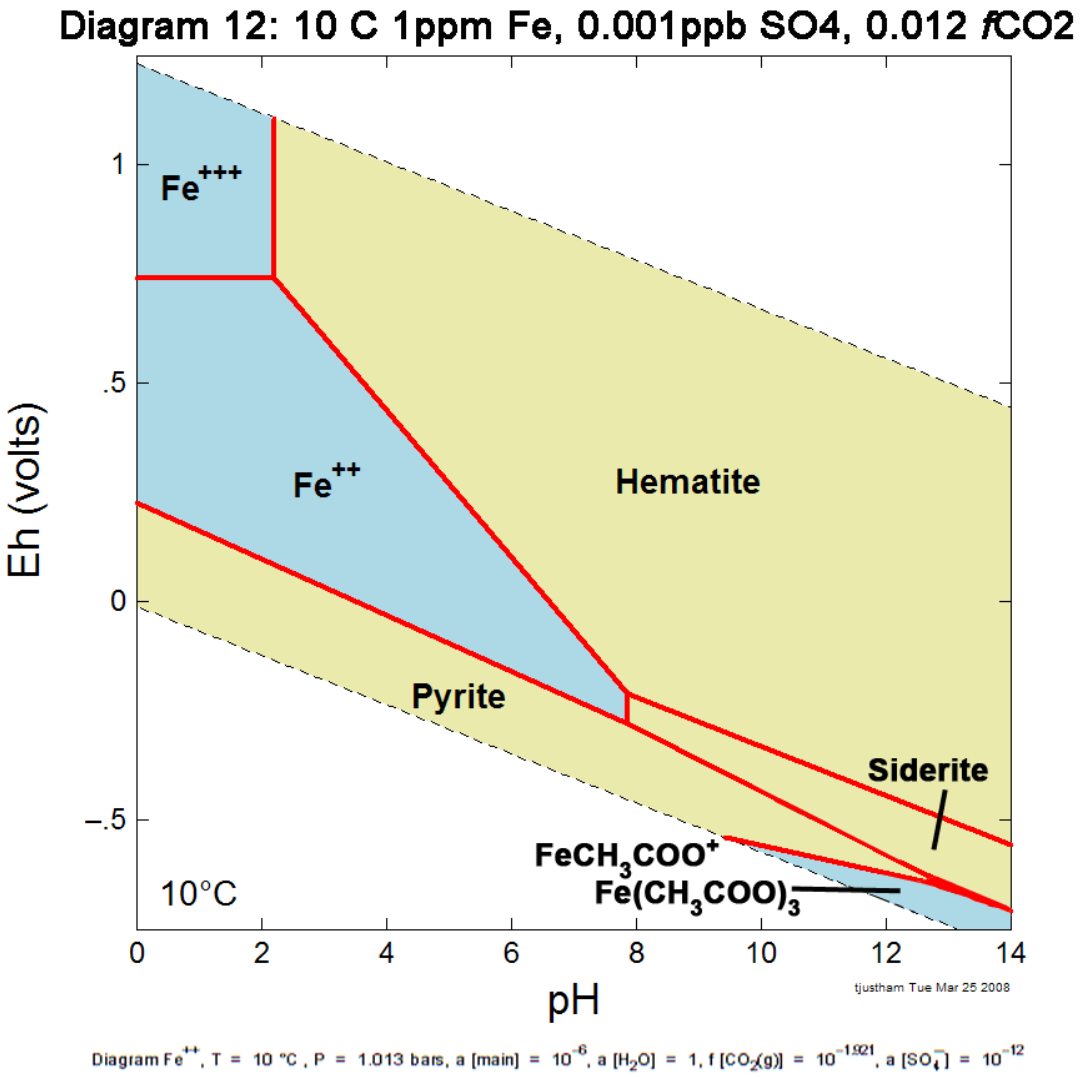
Diagram 12: 10 C 1ppm Fe, 0.001ppb SO4, 0.012 fCO2
Fe+++
Fe++
Hematite
Pyrite
Siderite
FeCH3COO+
Fe(CH3COO)3
10°C
Eh (volts)
pH
1
.5
0
–.5
0
2
4
6
8
10
12
14
tjustham Tue Mar 25 2008
Diagram Fe++, T = 10 °C, P = 1.013 bars, a [main] = 10-6, a [H2O] = 1, f [CO2(g)] = 10-1.921, a [SO4--] = 10-12

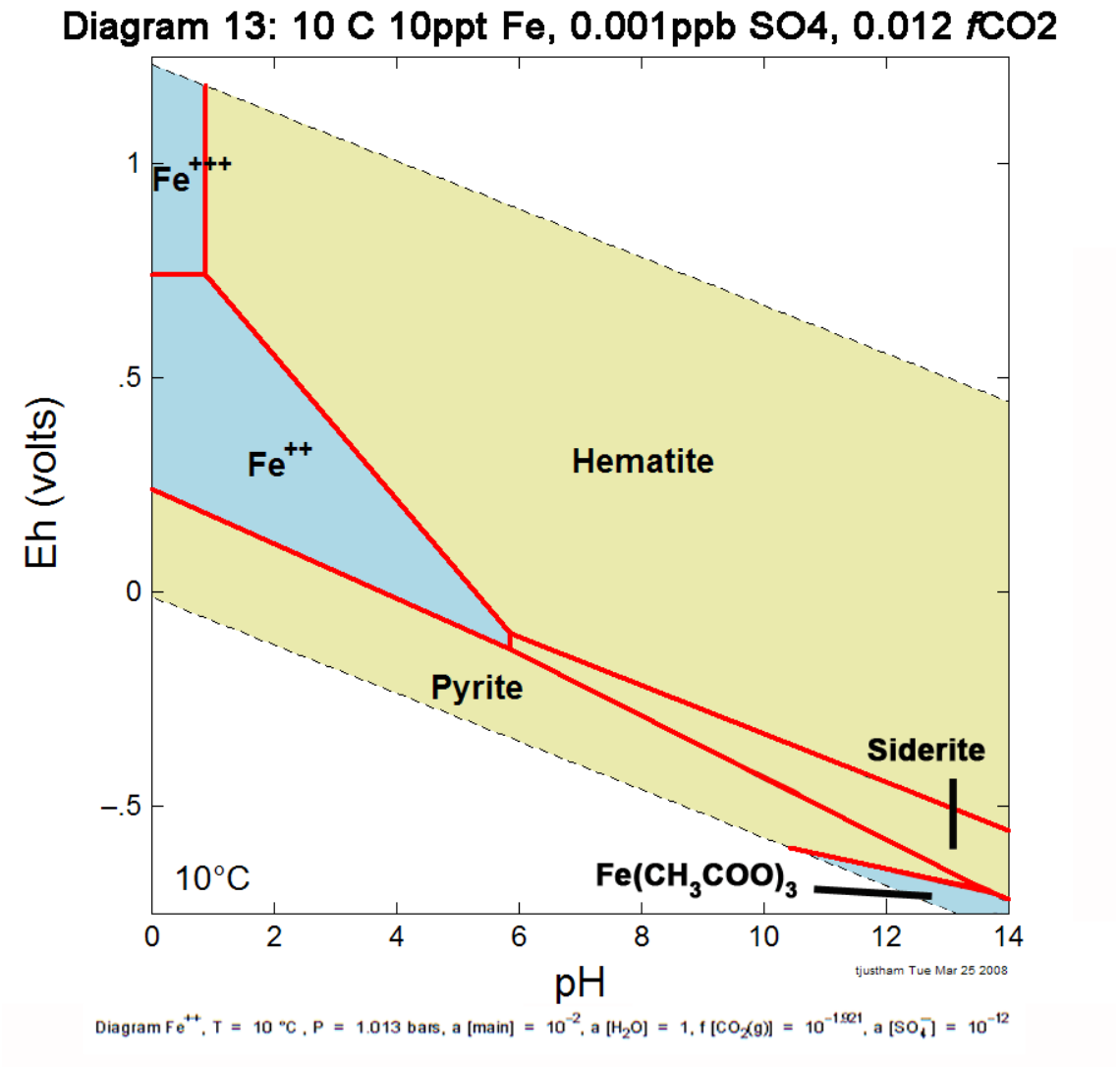
Diagram 13: 10 C 10ppt Fe, 0.001ppb SO4, 0.012 fCO2
Fe+++
Fe++
Hematite
Pyrite
Siderite
Fe(CH3COO)3
10°C
Eh (volts)
pH
1
.5
0
–.5
0
2
4
6
8
10
12
14
tjustham Tue Mar 25 2008
Diagram Fe++, T = 10 °C , P = 1.013 bars, a [main] = 10-2, a [H2O] = 1, f [CO2(g)] = 10-1.921, a [SO4--] = 10-12

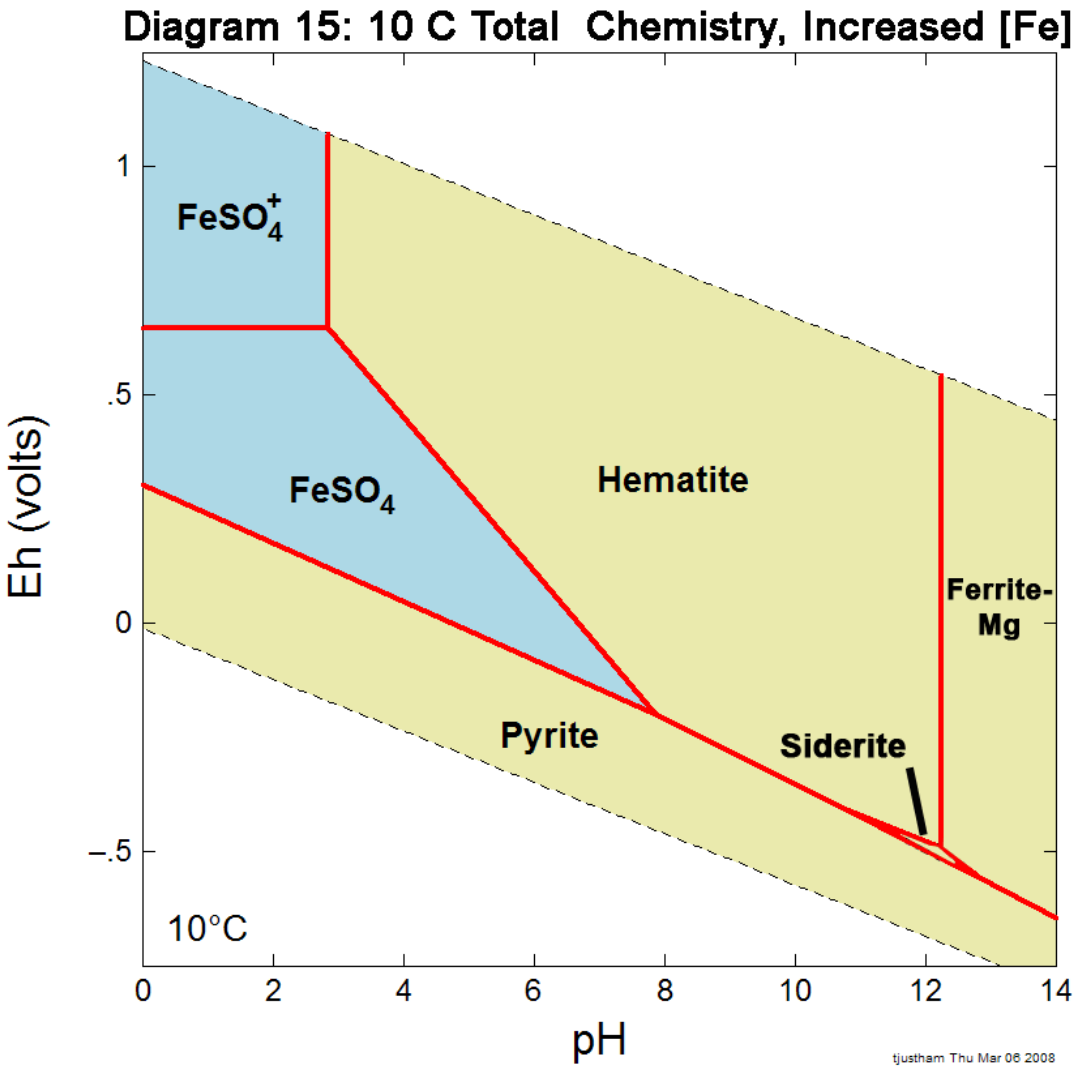

Diagram Fe^{++}, T = 10 °C , P = 1.013 bars, a [main] = 10^{-6}, a [H_2O] = 1, f [CO_2(g)] = $10^{-2.523}$, a [SO_4^{--}] = 10^{-2}, a [Cl^-] = 10^{-3}, a [Na^+] = 10^{-4}, a [Mn^{++}] = 10^{-5}, a [Mg^{++}] = 10^{-2}, a [Ca^{++}] = 10^{-2}

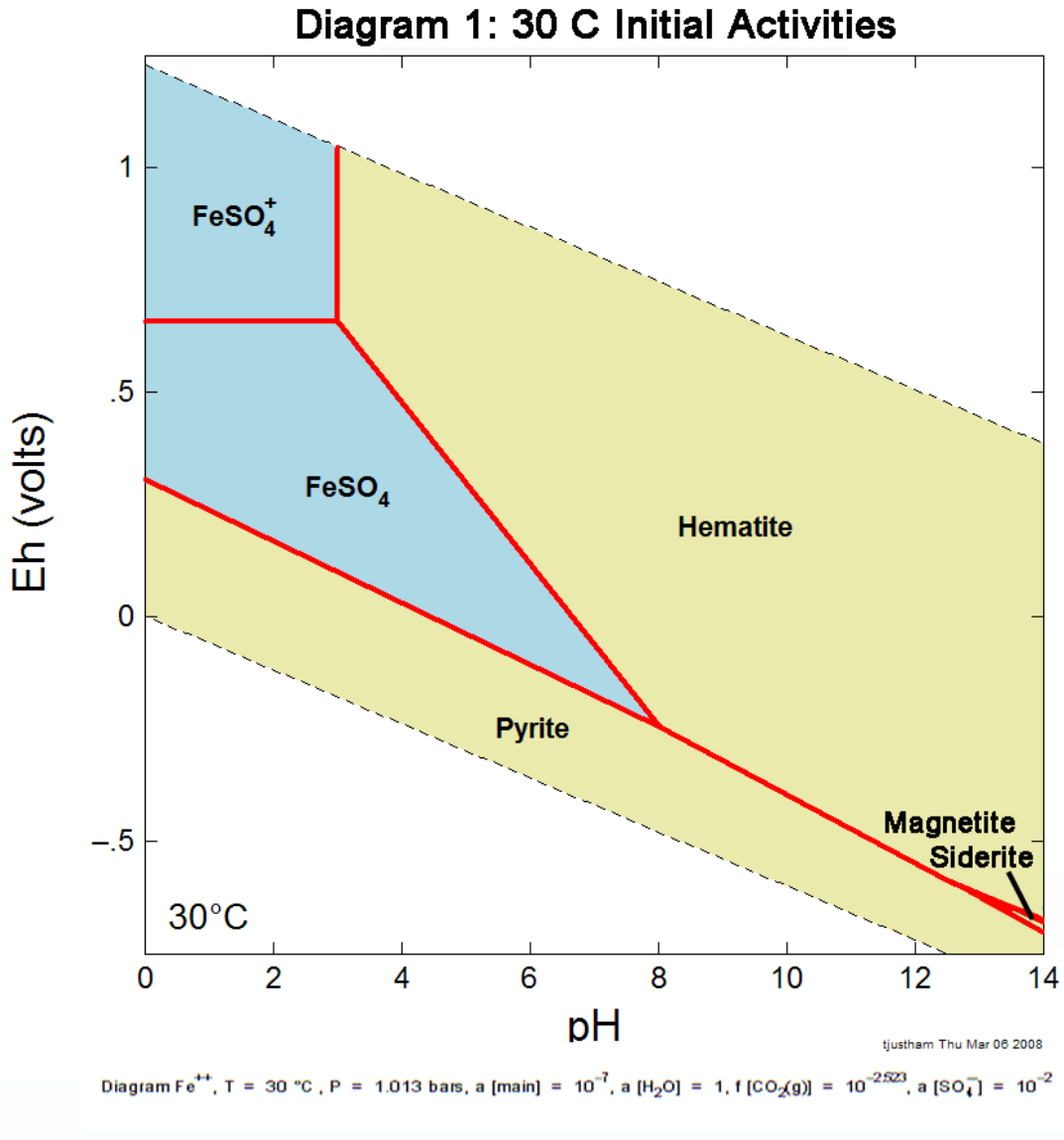
Diagram 1: 30 C Initial Activities
Eh (volts)
1
.5
0
–.5
FeSO4+
FeSO4
Hematite
Pyrite
Magnetite
Siderite
30°C
0
2
4
6
8
10
12
14
pH
tjustham Thu Mar 06 2008
Diagram Fe++, T = 30 °C , P = 1.013 bars, a [main] = 10−7, a [H2O] = 1, f [CO2(g)] = 10−2.523, a [SO4−−] = 10−2

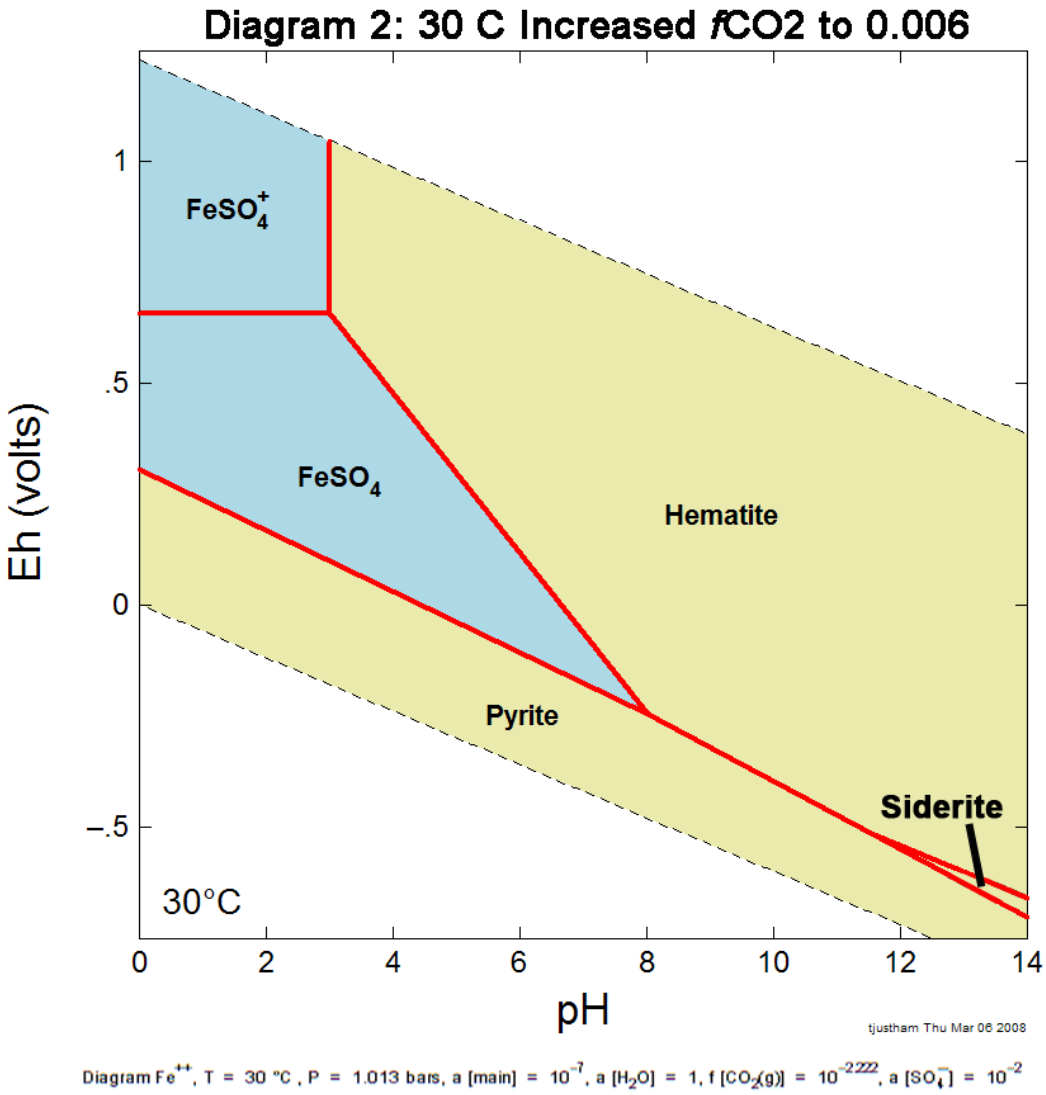
Diagram 2: 30 C Increased fCO2 to 0.006
Eh (volts)
1
.5
0
–.5
FeSO4+
FeSO4
Hematite
Pyrite
Siderite
30°C
0
2
4
6
8
10
12
14
pH
tjustham Thu Mar 06 2008
Diagram Fe++, T = 30 °C , P = 1.013 bars, a [main] = 10-7, a [H2O] = 1, f [CO2(g)] = 10-2.222, a [SO4--] = 10-2

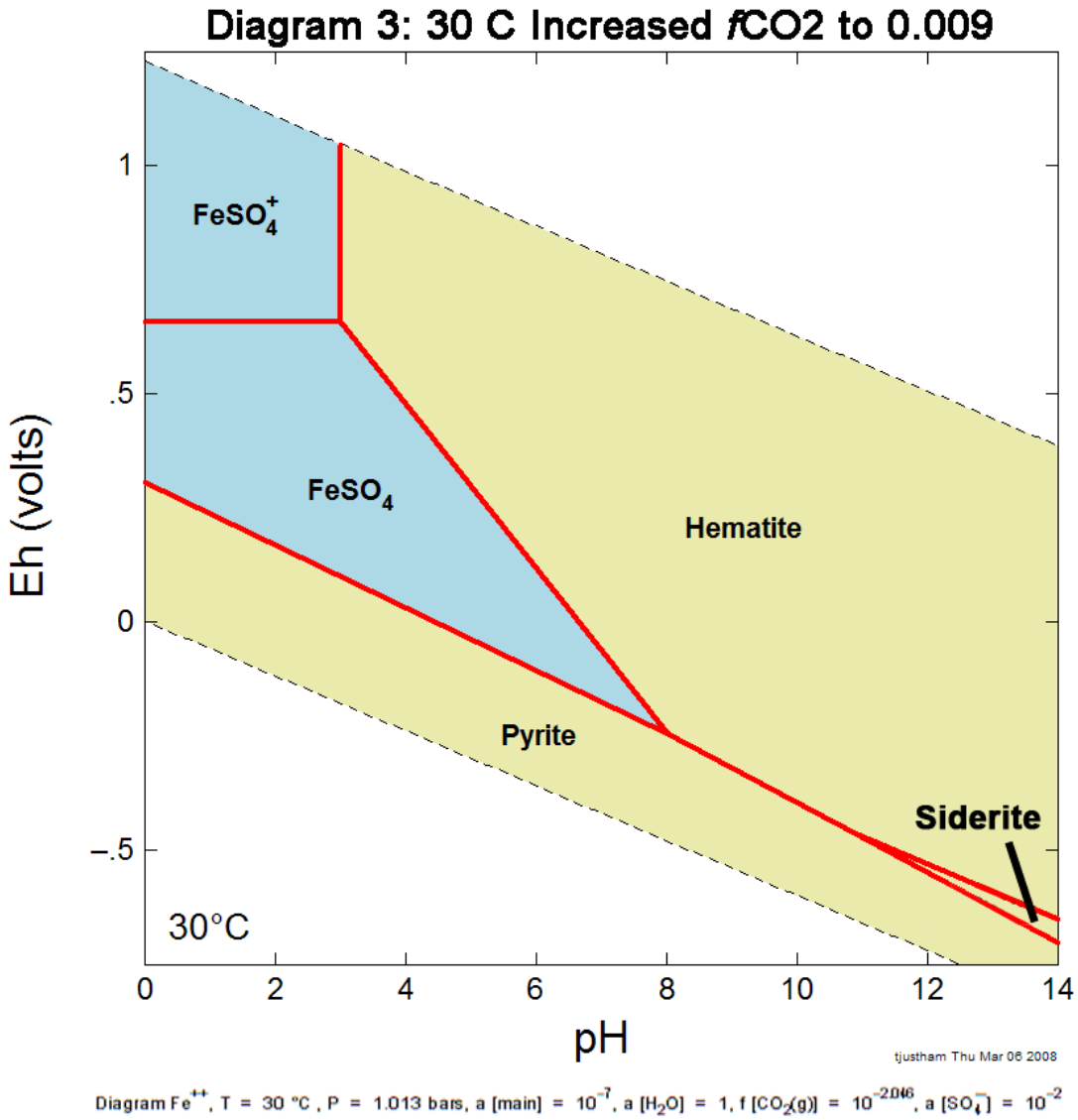
Diagram 3: 30 C Increased fCO2 to 0.009
Eh (volts)
1
.5
0
–.5
FeSO4+
FeSO4
Hematite
Pyrite
Siderite
30°C
0
2
4
6
8
10
12
14
pH
tjustham Thu Mar 06 2008
Diagram Fe++, T = 30 °C, P = 1.013 bars, a [main] = 10-7, a [H2O] = 1, f [CO2(g)] = 10-2.046, a [SO4--] = 10-2

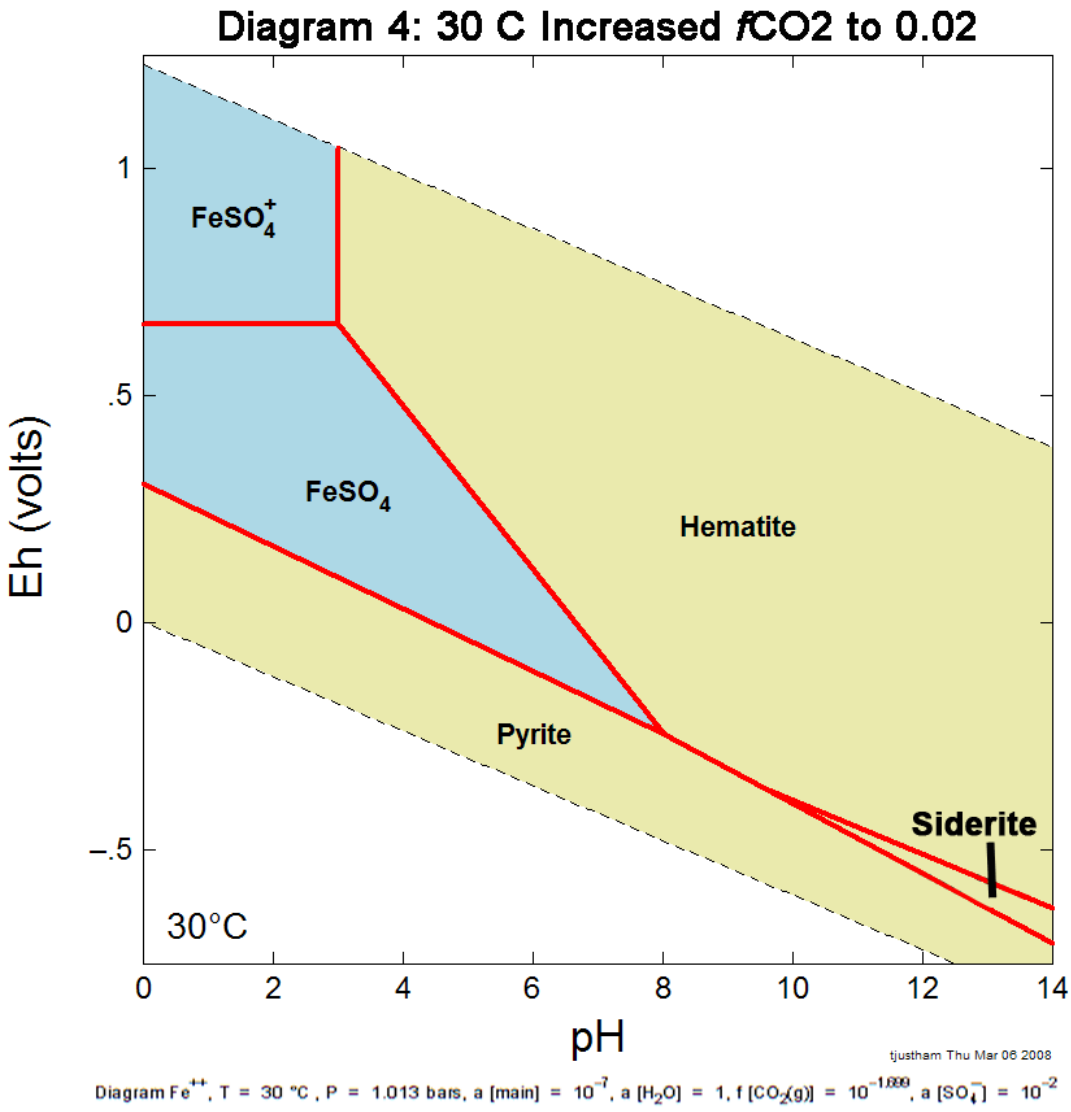
Diagram 4: 30 C Increased fCO2 to 0.02
Eh (volts)
1
.5
0
–.5
FeSO4+
FeSO4
Hematite
Pyrite
Siderite
30°C
0
2
4
6
8
10
12
14
pH
tjustham Thu Mar 06 2008
Diagram Fe++, T = 30 °C , P = 1.013 bars, a [main] = 10-7, a [H2O] = 1, f [CO2(g)] = 10-1.699, a [SO4--] = 10-2

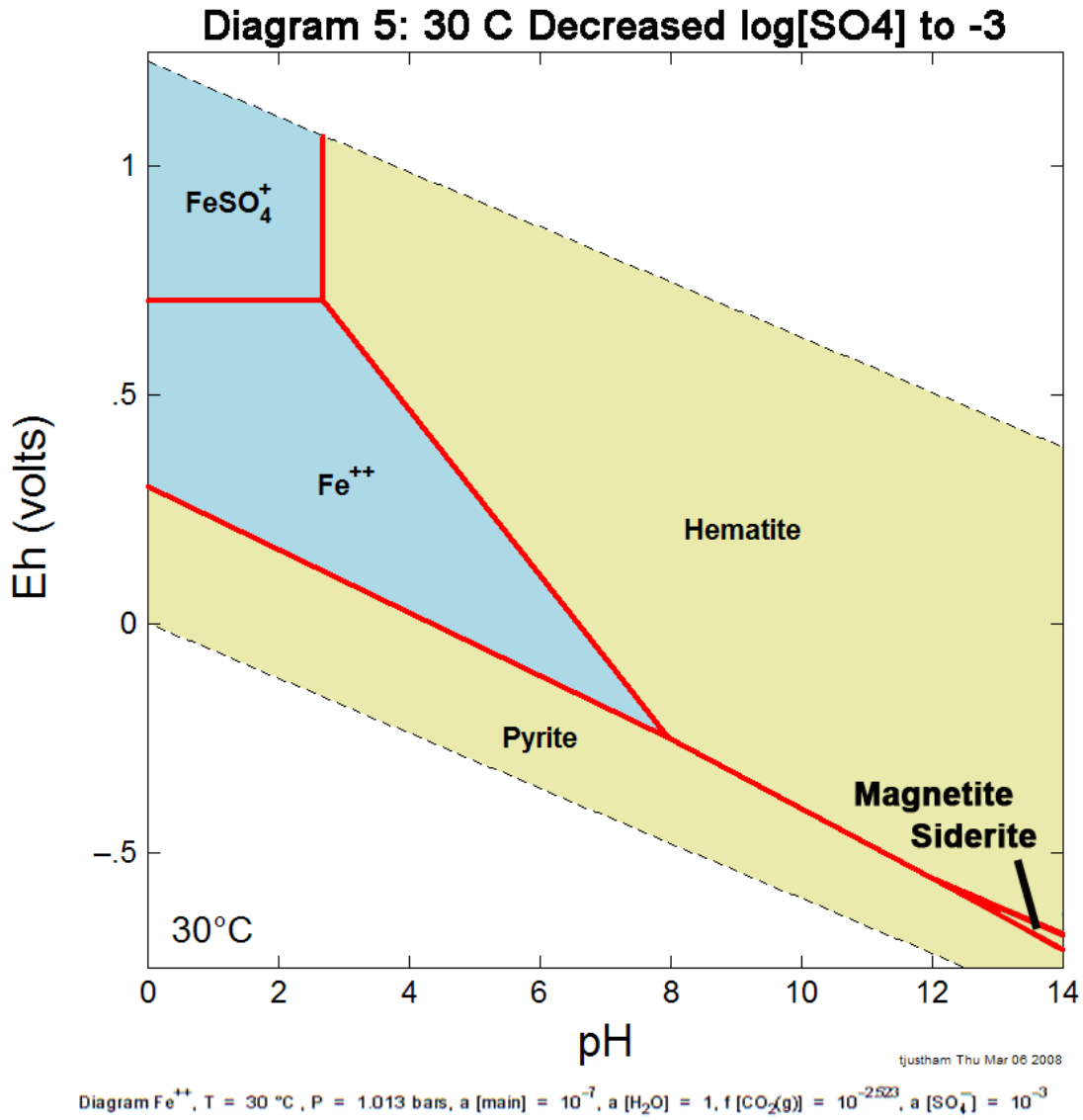
Diagram 5: 30 C Decreased log[SO4] to -3
Eh (volts)
1
.5
0
–.5
FeSO4+
Fe++
Hematite
Pyrite
Magnetite
Siderite
30°C
0
2
4
6
8
10
12
14
pH
tjustham Thu Mar 06 2008
Diagram Fe++, T = 30 °C , P = 1.013 bars, a [main] = 10-7, a [H2O] = 1, f [CO2(g)] = 10-2.523, a [SO4--] = 10-3

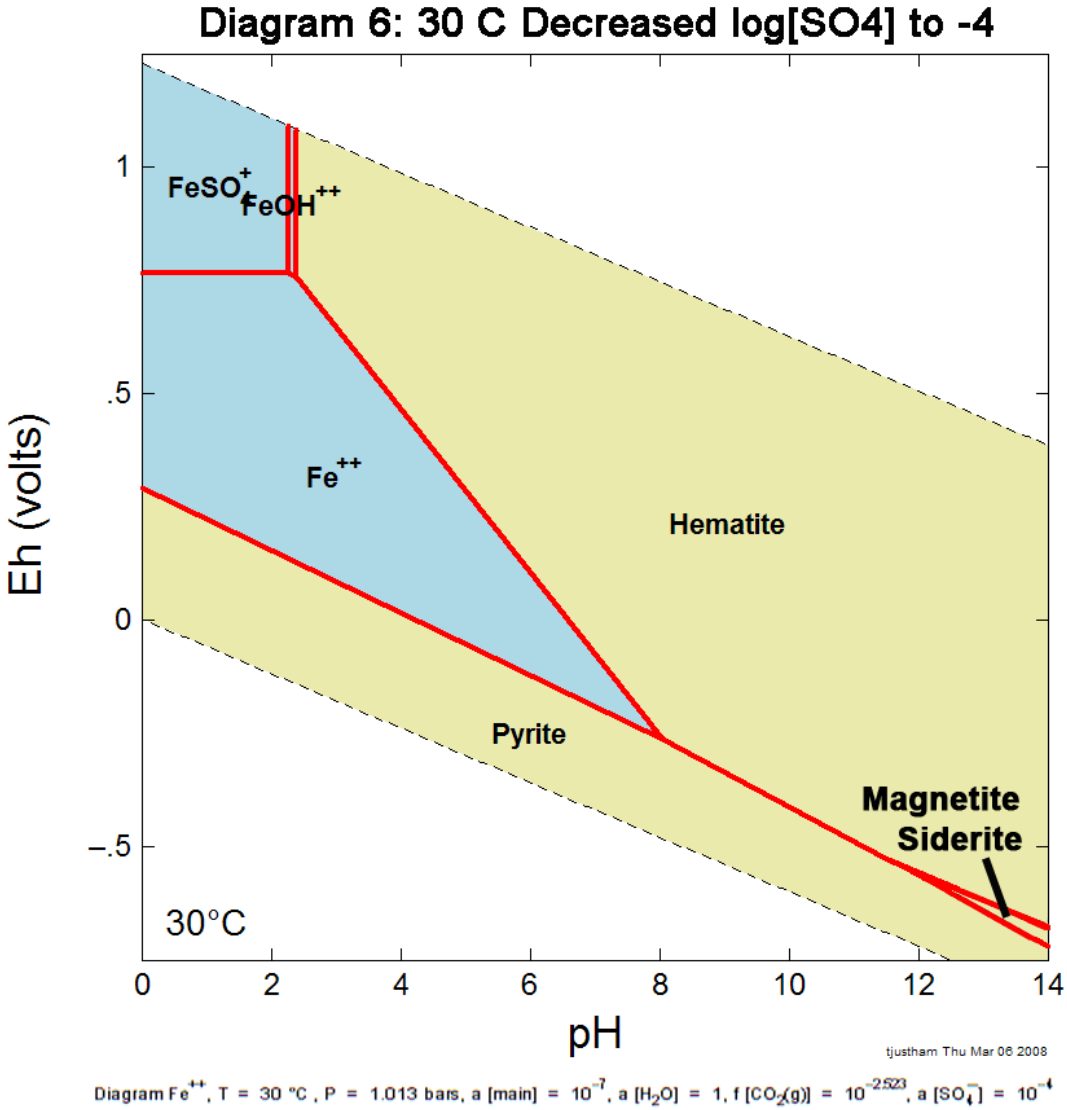
Diagram 6: 30 C Decreased log[SO4] to -4
FeSO4+
FeOH++
Fe++
Hematite
Pyrite
Magnetite
Siderite
30°C
Eh (volts)
pH
1
.5
0
–.5
0
2
4
6
8
10
12
14
tjustham Thu Mar 06 2008
Diagram Fe++, T = 30 °C , P = 1.013 bars, a [main] = 10-7, a [H2O] = 1, f [CO2(g)] = 10-2.523, a [SO4--] = 10-4

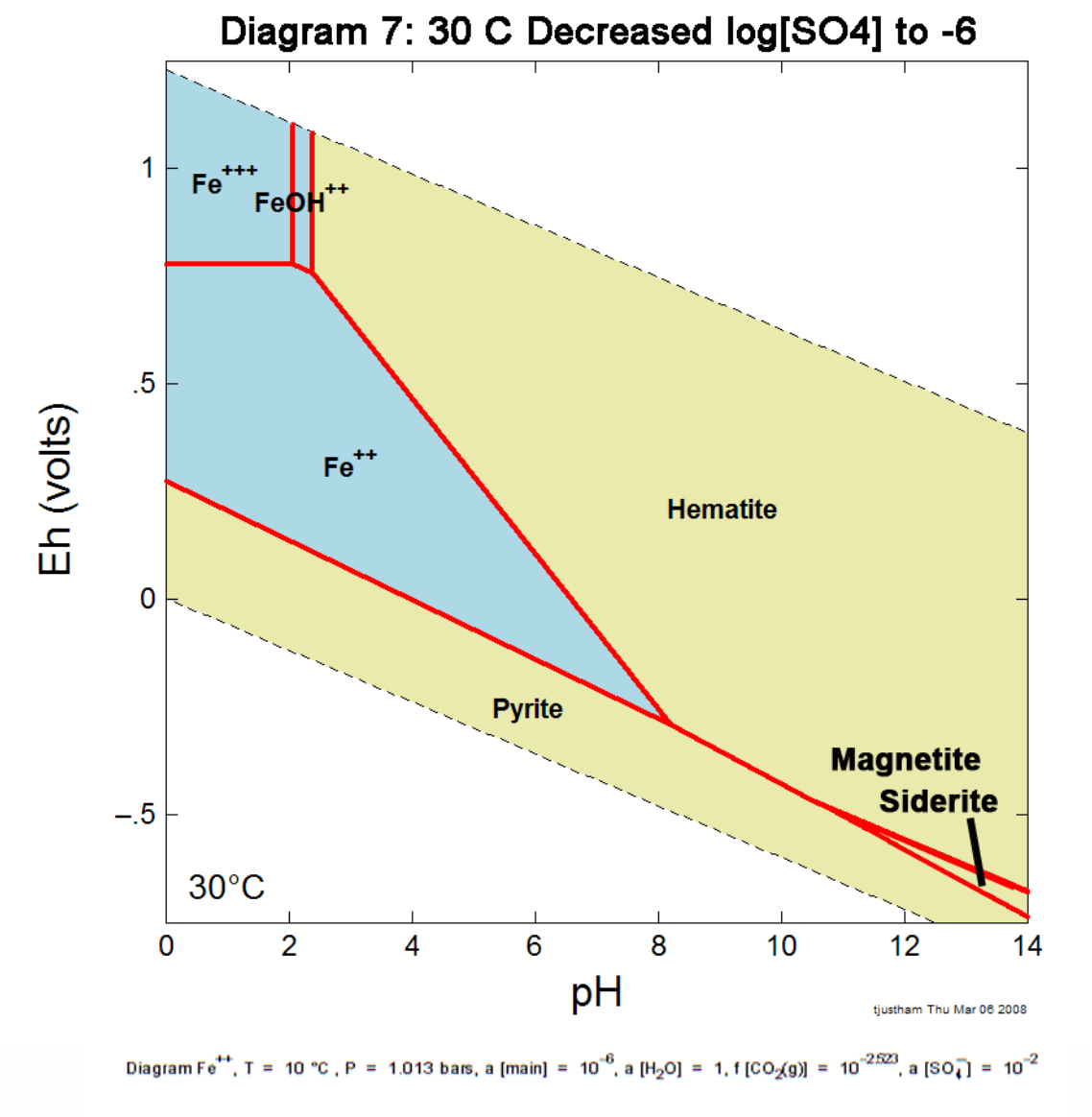
Diagram 7: 30 C Decreased log[SO4] to -6
Fe+++
FeOH++
Fe++
Hematite
Pyrite
Magnetite
Siderite
30°C
Eh (volts)
pH
1
.5
0
–.5
0
2
4
6
8
10
12
14
tjustham Thu Mar 06 2008
Diagram Fe++, T = 10 °C, P = 1.013 bars, a [main] = 10-6, a [H2O] = 1, f [CO2(g)] = 10-2.523, a [SO4--] = 10-2

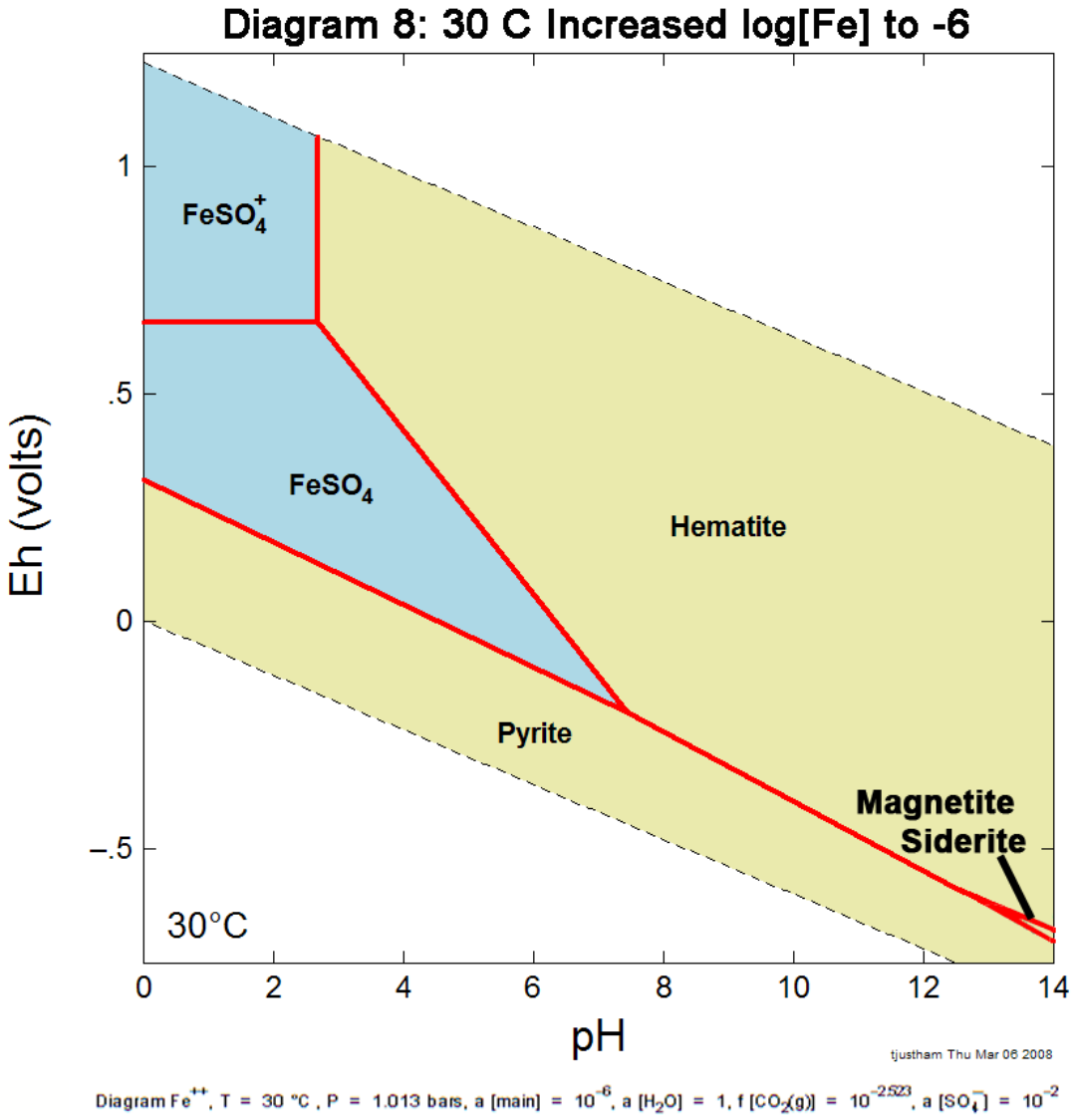
Diagram 8: 30 C Increased log[Fe] to -6
Eh (volts)
1
.5
0
–.5
FeSO4+
FeSO4
Hematite
Pyrite
Magnetite
Siderite
30°C
0
2
4
6
8
10
12
14
pH
tjustham Thu Mar 06 2008
Diagram Fe++, T = 30 °C , P = 1.013 bars, a [main] = 10-6, a [H2O] = 1, f [CO2(g)] = 10-2.523, a [SO4--] = 10-2

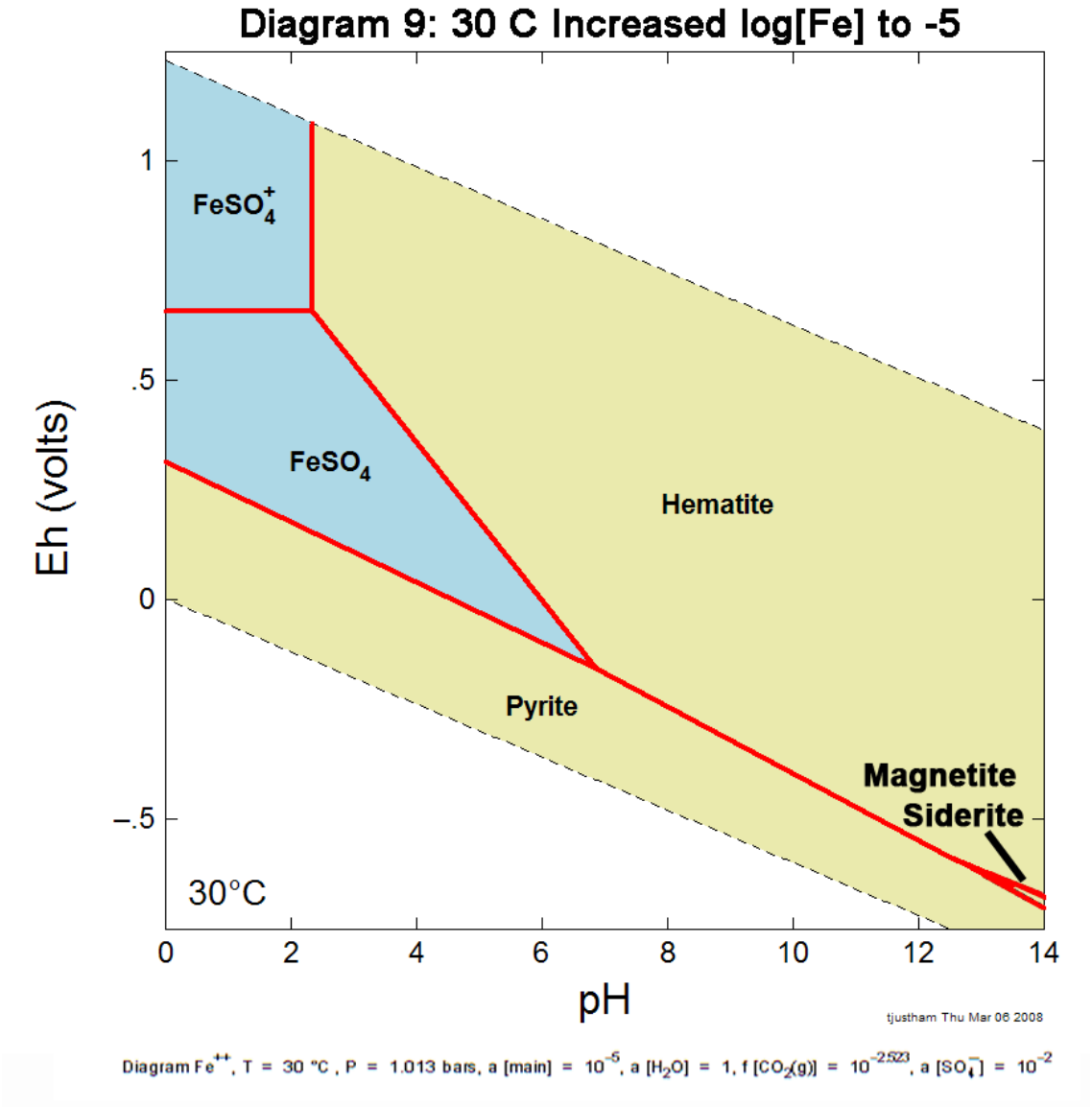
Diagram 9: 30 C Increased log[Fe] to -5
Eh (volts)
1
.5
0
–.5
FeSO4+
FeSO4
Hematite
Pyrite
Magnetite
Siderite
30°C
0
2
4
6
8
10
12
14
pH
tjustham Thu Mar 06 2008
Diagram Fe++, T = 30 °C, P = 1.013 bars, a [main] = 10-5, a [H2O] = 1, f [CO2(g)] = 10-2.523, a [SO4--] = 10-2

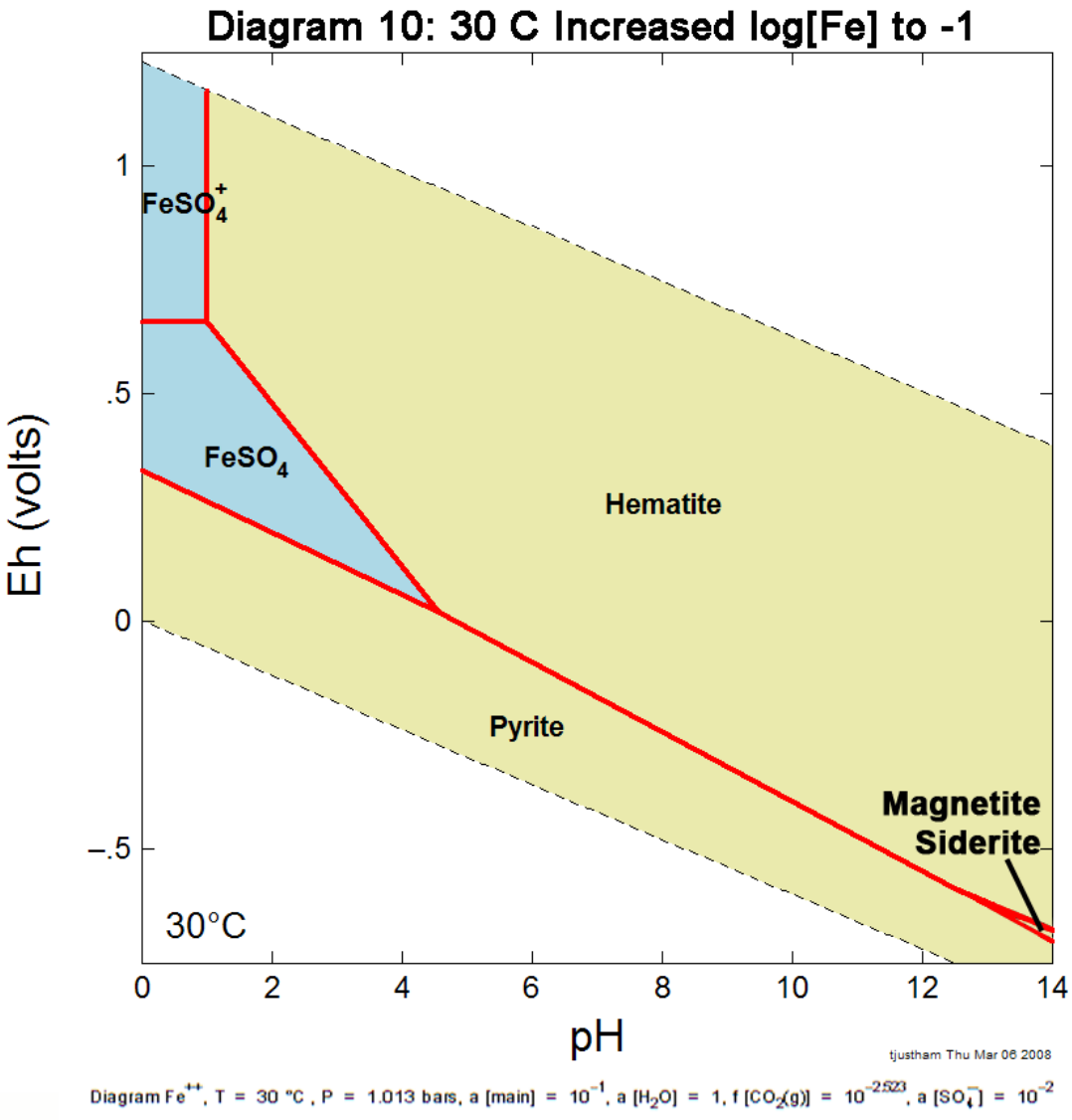
Diagram 10: 30 C Increased log[Fe] to -1
Eh (volts)
1
.5
0
–.5
FeSO4+
FeSO4
Hematite
Pyrite
Magnetite
Siderite
30°C
0
2
4
6
8
10
12
14
pH
tjustham Thu Mar 06 2008
Diagram Fe++, T = 30 °C , P = 1.013 bars, a [main] = 10-1, a [H2O] = 1, f [CO2(g)] = 10-2.523, a [SO4--] = 10-2

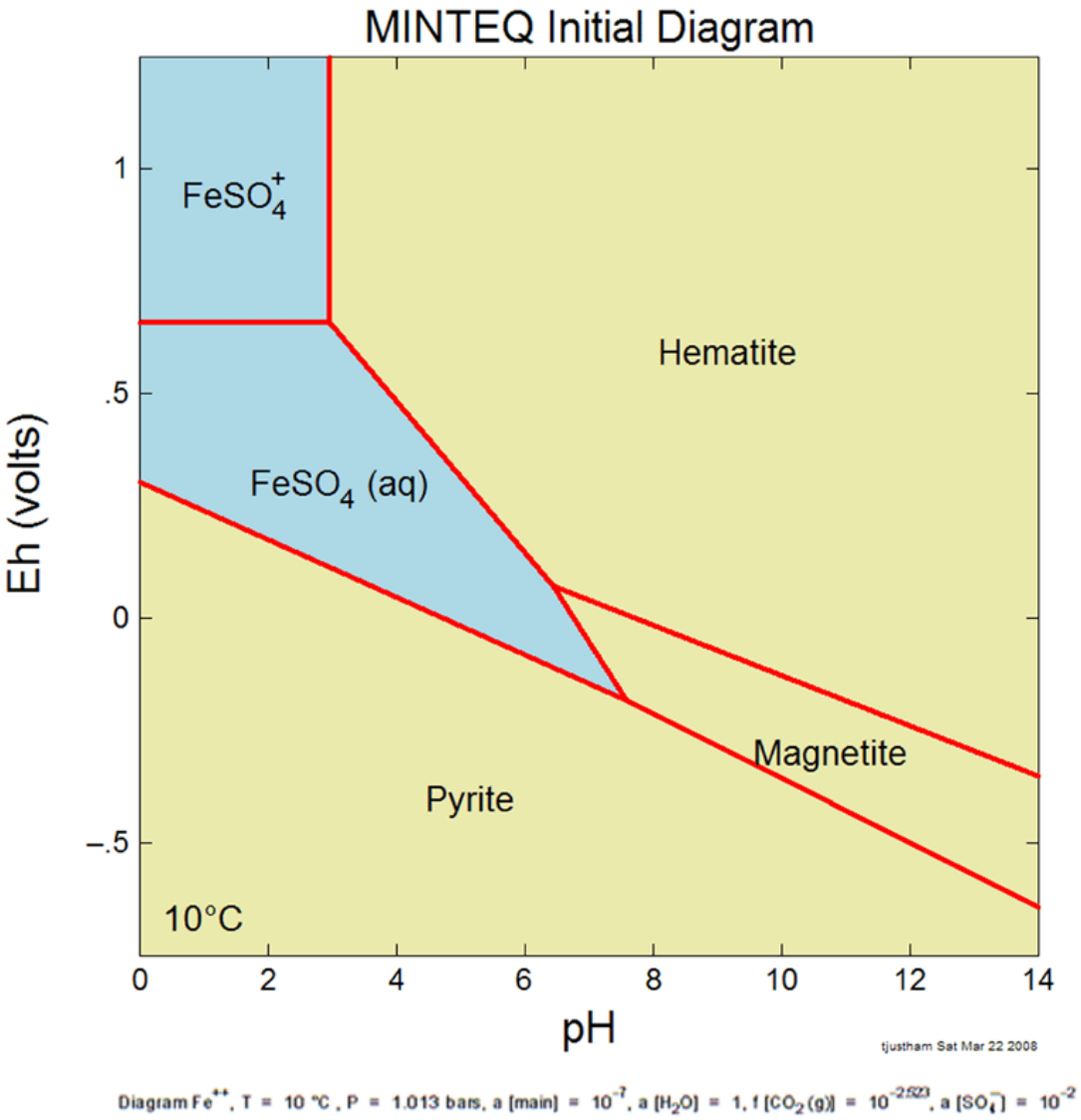
MINTEQ Initial Diagram
FeSO4+
Hematite
FeSO4 (aq)
Magnetite
Pyrite
10°C
Eh (volts)
pH
1
.5
0
–.5
0
2
4
6
8
10
12
14
tjustham Sat Mar 22 2008
Diagram Fe++, T = 10 °C, P = 1.013 bars, a [main] = 10-7, a [H2O] = 1, f [CO2 (g)] = 10-2.523, a [SO4--] = 10-2

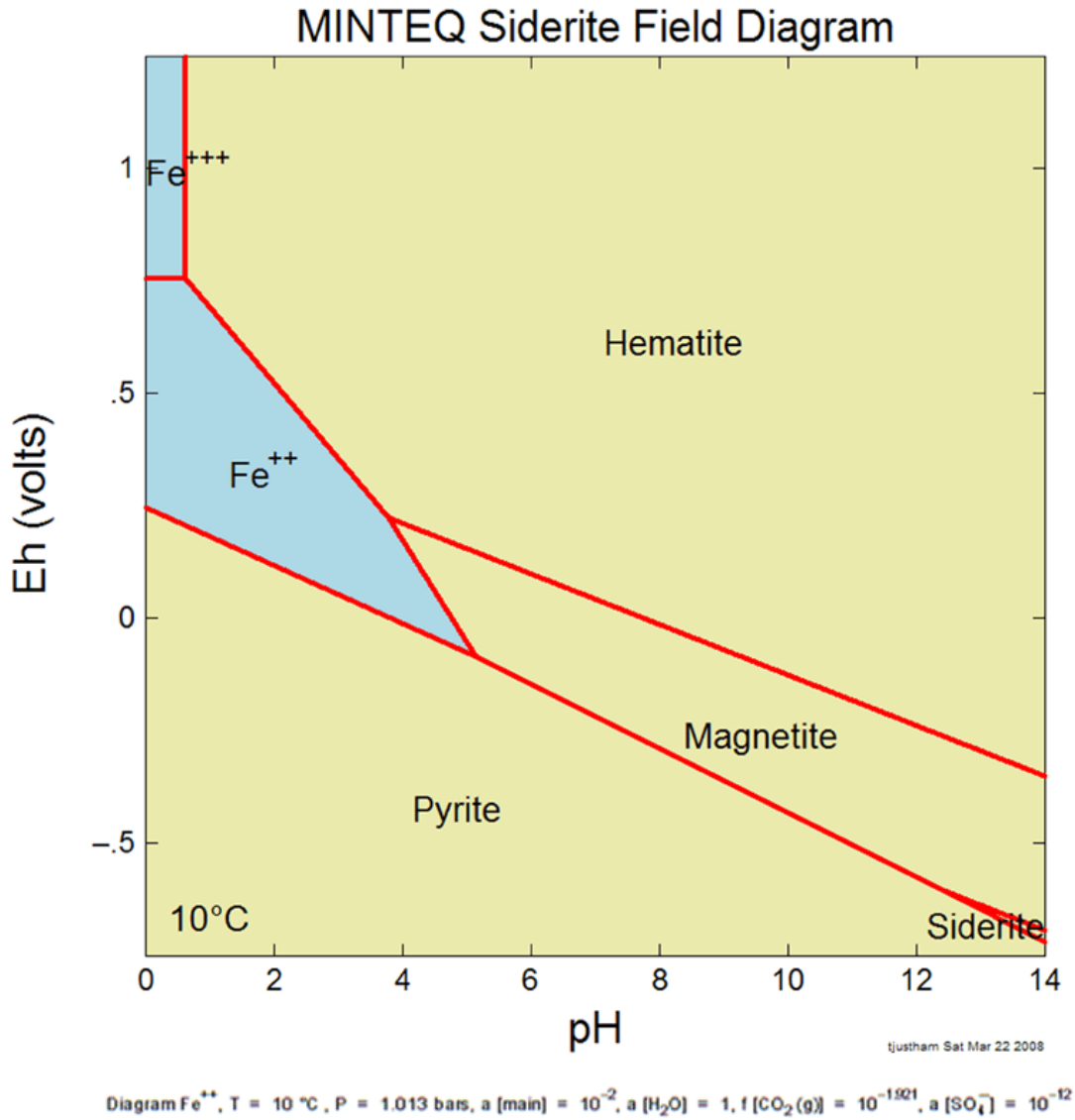

Diagram Fe^{++}, T = 10 °C, P = 1.013 bars, a [main] = 10^{-2}, a [H_2O] = 1, f [CO_2 (g)] = $10^{-1.921}$, a [SO_4^{--}] = 10^{-12}

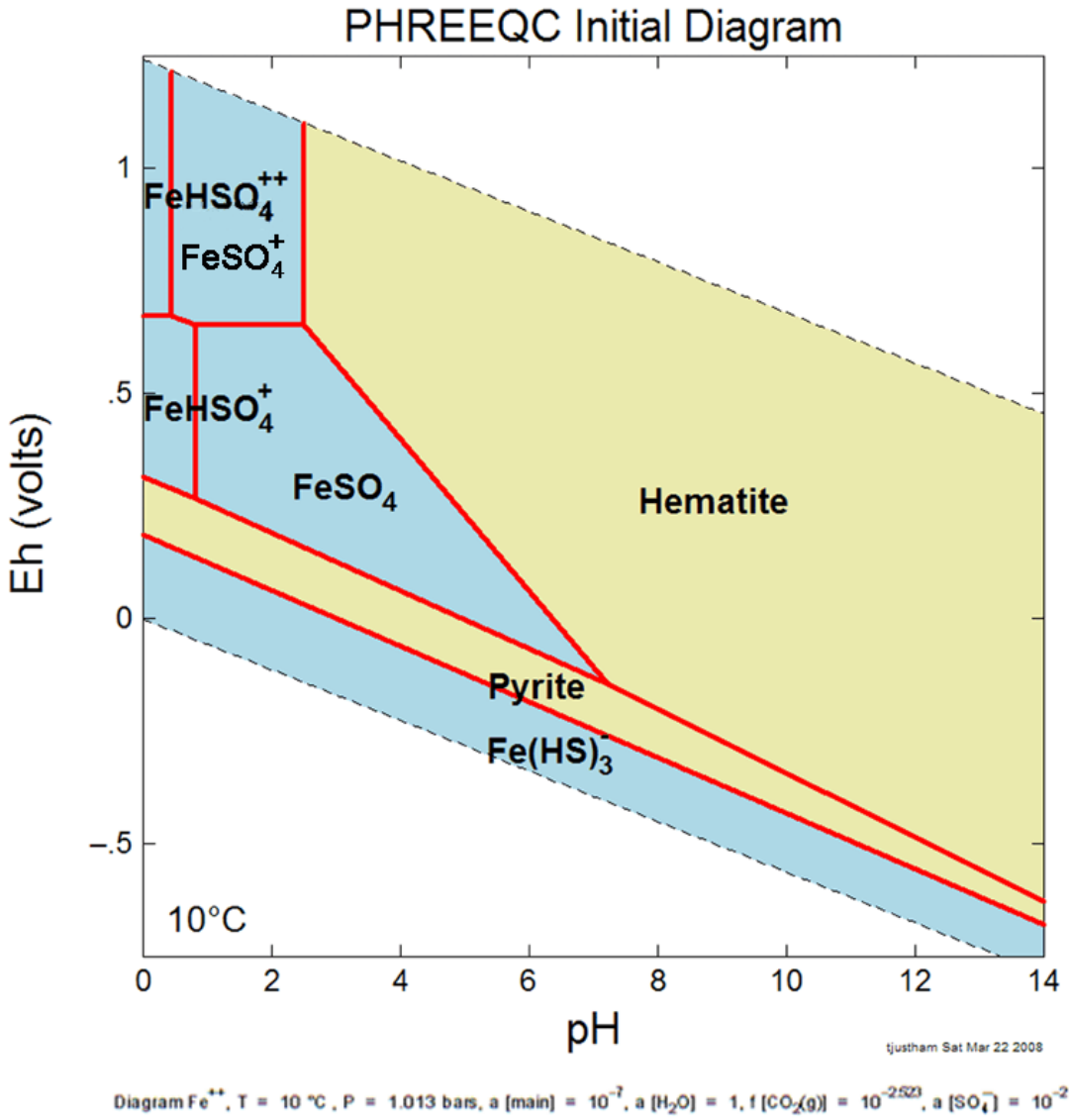
PHREEQC Initial Diagram
Eh (volts)
pH
1
.5
0
–.5
0
2
4
6
8
10
12
14
FeHSO4++
FeSO4+
FeHSO4+
FeSO4
Hematite
Pyrite
Fe(HS)3-
10°C
tjustham Sat Mar 22 2008
Diagram Fe++, T = 10 °C, P = 1.013 bars, a [main] = 10-7, a [H2O] = 1, f [CO2(g)] = 10-2.523, a [SO4--] = 10-2

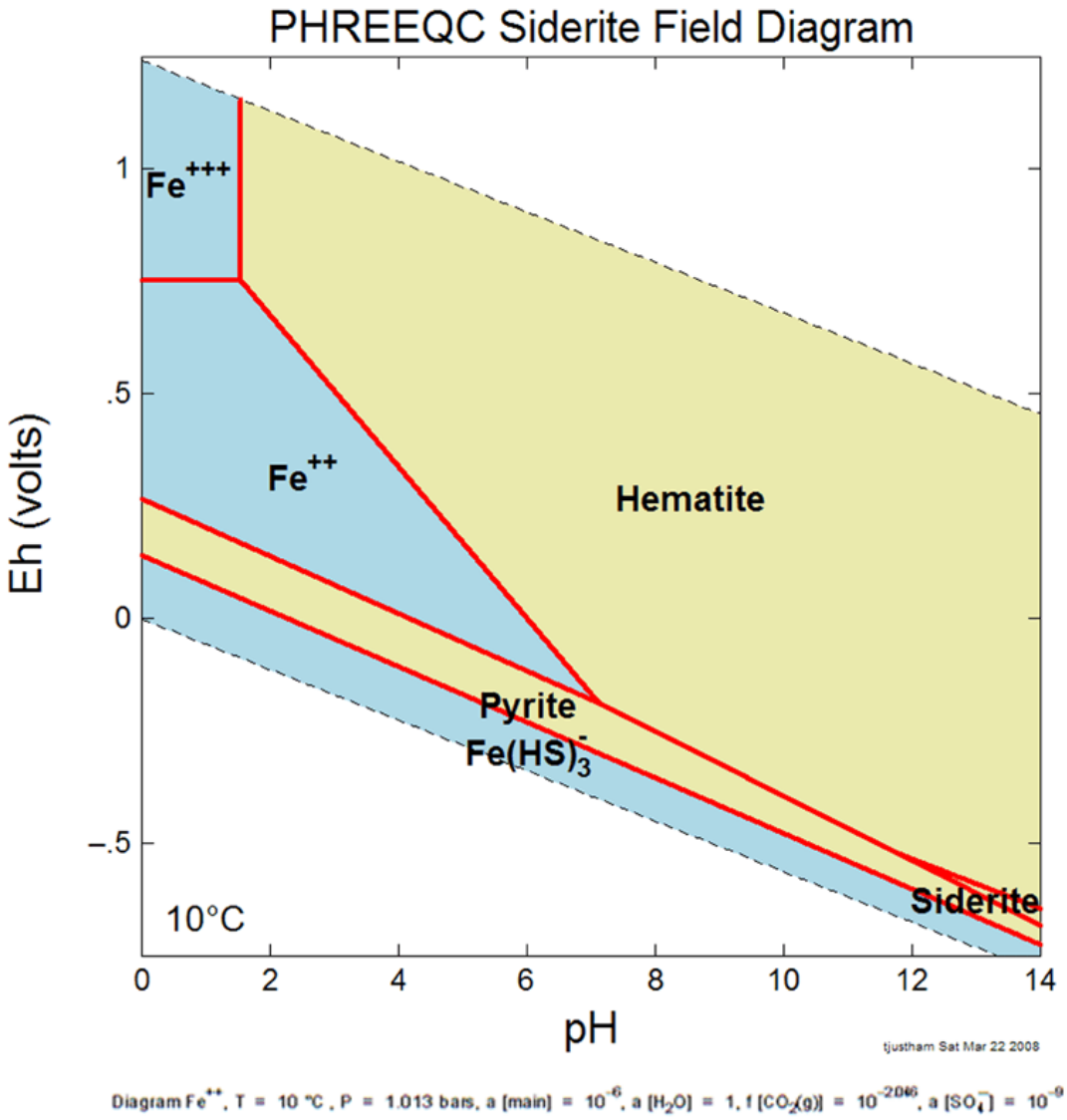
PHREEQC Siderite Field Diagram
Eh (volts)
pH
Fe+++
Fe++
Hematite
Pyrite
Fe(HS)3-
Siderite
10°C
1
.5
0
-.5
0
2
4
6
8
10
12
14
tjustham Sat Mar 22 2008
Diagram Fe++, T = 10 °C, P = 1.013 bars, a [main] = 10-6, a [H2O] = 1, f [CO2(g)] = 10-2.046, a [SO4--] = 10-9

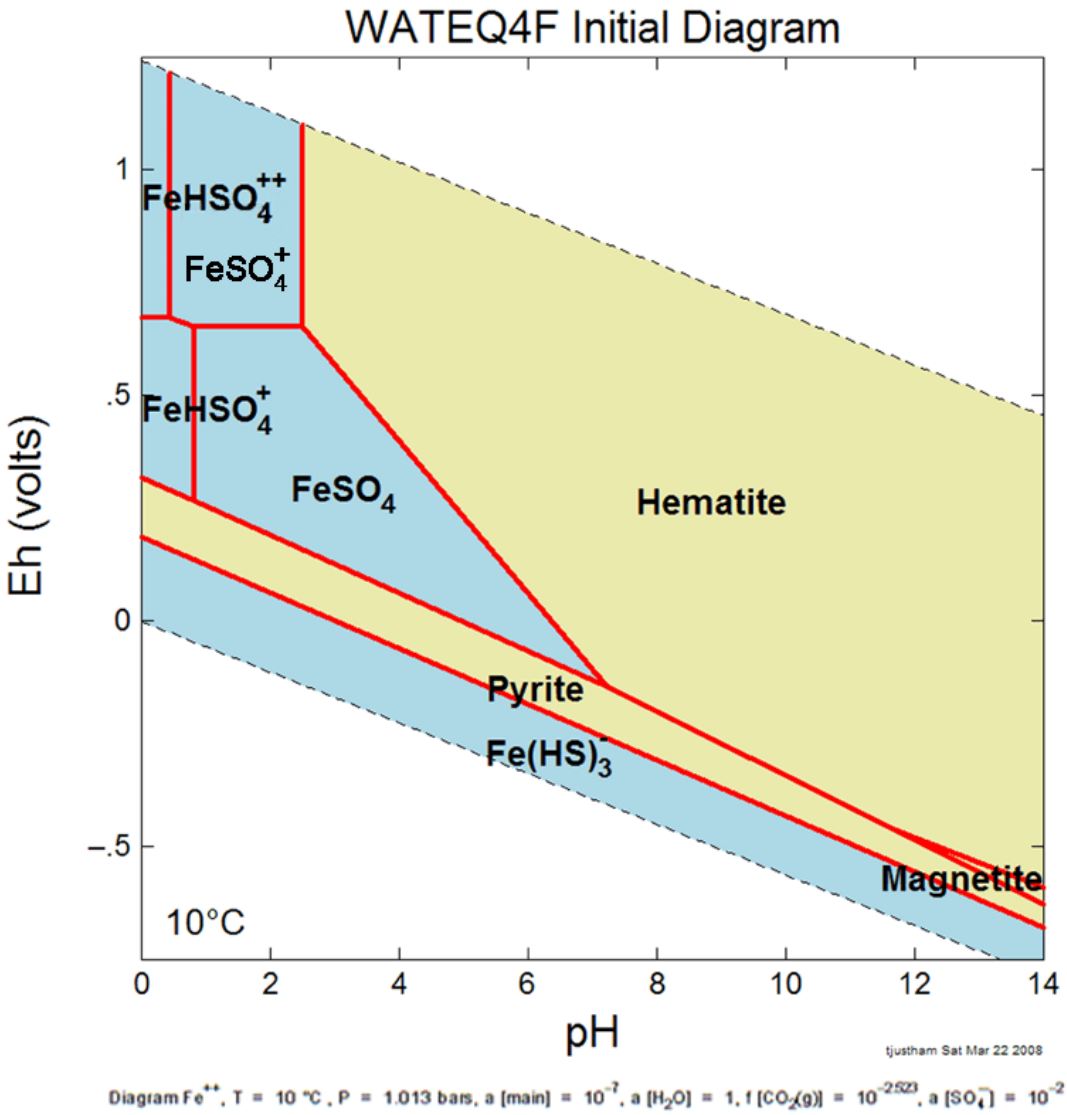
WATEQ4F Initial Diagram
Eh (volts)
1
.5
0
–.5
0
2
4
6
8
10
12
14
pH
FeHSO4++
FeSO4+
FeHSO4+
FeSO4
Hematite
Pyrite
Fe(HS)3-
Magnetite
10°C
tjustham Sat Mar 22 2008
Diagram Fe++, T = 10 °C, P = 1.013 bars, a [main] = 10-7, a [H2O] = 1, f [CO2(g)] = 10-2.523, a [SO4--] = 10-2

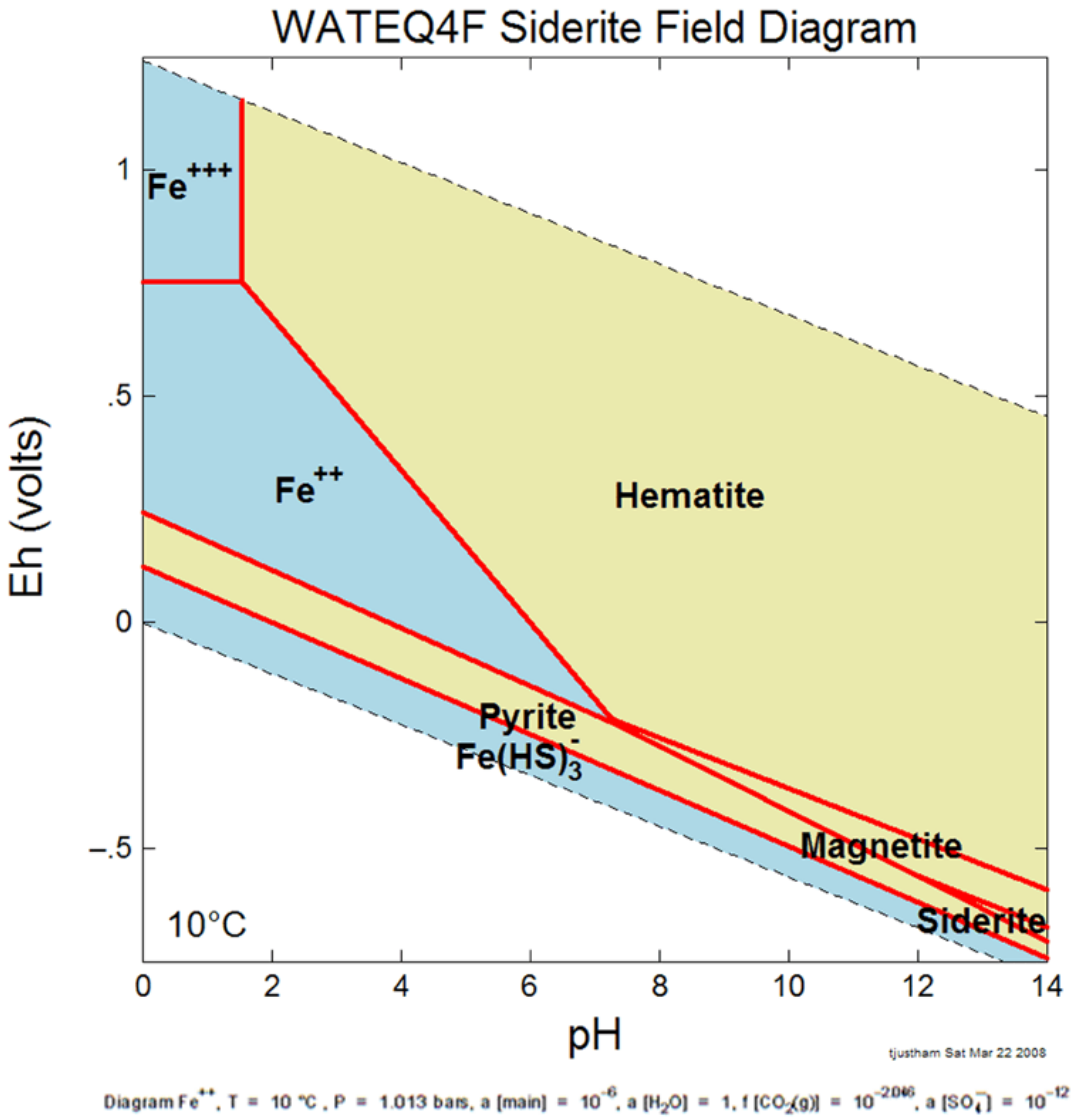
WATEQ4F Siderite Field Diagram
Fe+++
Fe++
Hematite
Pyrite
Fe(HS)3-
Magnetite
Siderite
10°C
Eh (volts)
pH
1
.5
0
–.5
0
2
4
6
8
10
12
14
tjustham Sat Mar 22 2008
Diagram Fe++, T = 10 °C, P = 1.013 bars, a [main] = 10-6, a [H2O] = 1, f [CO2(g)] = 10-2.046, a [SO4--] = 10-12

REFERENCES

Allison, P.A., and Pye, K., 1994, Early diagenetic mineralization and fossil preservation in modern carbonate concretions: Palaios, v. 9, p. 561–575.

Baker, J.C., Kassan, J., and Hamilton, P.J., 1995, Early diagenetic siderite as an indicator of depositional environment in the Triassic Rewan Group, southern Bowen Basin, eastern Australia: Sedimentology, v. 43, p. 77–88.

Burton, E.D., Bush, R.T., and Sullivan, L.A., 2006, Sedimentary iron geochemistry in acidic waterways associated with coastal lowland acid sulfate soils: Geochimica et Cosmochimica Acta, v. 70, p. 5455–5468.

Cochran, J.K., Landman, N.H., Turekian, K.K., Michard, A., and Schrag, D.P., 2003, Paleoceanography of the Late Cretaceous (Maastrichtian) Western Interior Seaway of North America: evidence from Sr and O isotopes: Palaeogeography, Palaeoclimatology, Palaeoecology, v. 191, p. 45–64.

Fastovsky, D.E., 1987, Paleoenvironments of vertebrate-bearing strata during the Cretaceous-Paleogene transition, eastern Montana and western North Dakota: Palaios, v. 2, p. 282–295.

Faure, G., 1998, Principles and applications of geochemistry: Prentice Hall, Upper Saddle River, 600 p.

Frye, C.I., 1967, The Hell Creek Formation in North Dakota [Ph.D. thesis]: Grand Forks, University of North Dakota, 411 p.

Garrels, R.M., 1960, Mineral equilibria: Harper & Brothers, Publishers, New York, 254 p.

Garrels, R.M., and Christ, C.L., 1965, Solutions, minerals, and equilibria: Harper and Row, New York, 450 p.

Gibson, C.L., 1990, Paleoenvironments, phylogeny, and oxygen isotopic ratios of freshwater bivalves at the Cretaceous-Paleogene boundary, Eastern Montana: A preliminary assessment [M.S. thesis]: Kingston, University of Rhode Island, 209 p.

Groenewold, G.H., 1971, Concretions and nodules in the Hell Creek Formation, southwestern North Dakota [M.S. thesis]: Grand Forks, University of North Dakota, 84 p.

Hartman, J.H., 2002, Hell Creek Formation and the early picking of the Cretaceous-Tertiary boundary, *in* Hartman, J.H., Johnson, K.R., and Nichols, D.J., eds., The Hell Creek Formation and the Cretaceous-Tertiary boundary in the Northern Great Plains: An integrated continental record of the end of the Cretaceous: Geological Society of America Special Paper 361, p. 1–7.

Johnson, K.R., 2002, Megaflora of the Hell Creek and lower Fort Union Formations in the western Dakotas: Vegetational response to climate change, the Cretaceous-Tertiary boundary event, and rapid marine transgression, *in* Hartman, J.H., Johnson, K.R., and Nichols, D.J., eds., The Hell Creek Formation and the Cretaceous-Tertiary boundary in the Northern Great Plains: An integrated continental record of the end of the Cretaceous: Geological Society of America Special Paper 361, p. 329–391.

Moore, W.L., 1976, The stratigraphy and environments of deposition of the Cretaceous Hell Creek Formation (reconnaissance) and the Paleocene Ludlow Formation (detailed), southwestern North Dakota: North Dakota Geological Survey Report of Investigation No. 56, 40 p.

Mozley, P.S., 1989, Relation between depositional environment and the elemental composition of early diagenetic siderite: Geology, v. 17, p. 704–706.

Mozley, P.S., and Wersin, P., 1992, Isotopic composition of siderite as an indicator of depositional environment: Geology, v. 20, p. 681–692.

Murphy, E.C., Hoganson, J.W., and Johnson, K.R., 2002, Lithostratigraphy of the Hell Creek Formation in North Dakota, *in* Hartman, J.H., Johnson, K.R., and Nichols, D.J., eds., The Hell Creek Formation and the Cretaceous-Tertiary boundary in the Northern Great Plains: An integrated continental record of the end of the Cretaceous: Geological Society of America Special Paper 361, p. 9–34.

Nichols, D.J., and Johnson, K.R., 2002, Palynology and microstratigraphy of Cretaceous-Tertiary boundary sections in southwestern North Dakota, *in* Hartman, J.H., Johnson, K.R., and Nichols, D.J., eds., The Hell Creek Formation and the Cretaceous-Tertiary boundary in the Northern Great Plains: An integrated continental record of the end of the Cretaceous: Geological Society of America Special Paper 361, p. 95–143.

Postma, D., 1977, The occurrence and chemical composition of recent Fe-rich mixed carbonates in a river bog: Journal of Sedimentary Petrology, v. 47, p. 1089–1098.

Postma, D., 1981, Formation of siderite and vivianite and the pore-water composition of a recent bog sediment in Denmark: Chemical Geology, v. 31, p. 225–244.

Postma, D., 1982, Pyrite and siderite formation in brackish and freshwater swamp sediments: American Journal of Science, v. 282, p. 1151–1183.

Pye, K., Dickson, J.A.D., Schiavon, N., Coleman, M.L., and Cox, M., 1990, Formations of siderite-Mg-calcite-iron sulphide concretions in intertidal marsh and sandflat sediments, North Norfolk, England: Sedimentology, v. 37, p. 325–343.

Weast, R.C., Astle, W.J., and Beyer, W.H., 1986, CRC Handbook of Chemistry and Physics: CRC Press, Boca Raton, FL, 2424 p.

Woods, T.L., and Garrels, R.M., 1987, Thermodynamic values at low temperature for natural inorganic materials: An uncritical summary: Oxford University Press, New York, 242 p.